Mechanotransduction and Flow across the Endothelial Glycocalyx

by

Xiaobing Zhang

A dissertation submitted to the Faculty in Engineering in partial fulfillment of the requirements for the degree of Doctor of Philosophy,

The City University of New York

2005

UMI Number: 3187444

ProQuest Information and Learning Company
300 North Zeeb Road
P.O. Box 1346
Ann Arbor, MI 48106-1346

This manuscript has been read and accepted for the Graduate Faculty in Engineering in satisfaction of the dissertation requirements for the degree of Doctor of Philosophy.

Date	Professor Sheldon Weinbaum Chair of Examining Committee
Date	Professor Mumtaz K. Kassir Executive Officer
	Professor Stephen C. Cowin
	Professor Bingmei Fu
	Professor John M. Tarbell
	Professor Fitz-Roy E. Curry Supervisory Committee

The City University of New York

Abstract

Mechanotransduction and Flow across the Endothelial Glycocalyx

by

Xiaobing Zhang

Mentor: Professor Sheldon Weinbaum, Co-mentor: Professor Fitz-Roy E. Curry

While the endothelial glycocalyx layer (EGL) was first identified by special electron microscopic staining techniques nearly forty years ago (Luft, 1967), it is only relatively recently that this surface layer has been observed *in vivo* (Vink and Duling, 1996), and the importance of its multifaceted physiological functions recognized. In this dissertation we quantitatively investigate the physiological functions of the EGL as a mechanotransducer of fluid shearing stress, and as a transport barrier, using models for the quasi-periodic structure of the EGL proposed in Squire et al. (2001) and Weinbaum et al. (2003). We also develop a simplified 1-D model to describe the revised Starling principle using the structural parameters for the interendothelial cleft measured in rat mesenteric capillaries (Adamson et al., 2004).

We first present a mathematical model for estimating the mechanical properties of the endothelial glycocalyx fibers based on existing experimental data (Vink and Duling, 1999). The predicted value of EI, 700 pN·nm^2, indicates that the glycocalyx is stiff to resist large deformations due to both fluid shear stresses in the physiological range and shear stresses due to the passage of red blood cells, yet its fibers can easily buckle due to the normal forces when red cell motion is arrested in tightly fitting capillaries. Second, we use the detailed morphological data for rat mesenteric capillaries obtained by our collaborator at UC Davis, Dr. Adamson, to construct a 3-D model for water and protein transport in rat mesenteric microvessels, and use this to

confirm the Michel and Weinbaum hypothesis for a revised Starling principle in mammalian tissue. We also use this 3-D model to show that when the EGL covers the entrance to the cleft one cannot treat the hydraulic resistance of the EGL and cleft as two linear resistances in series. We then develop a much simpler, multilayer, 1-D theoretical model that can be solved analytically to provide most of the important results predicted by its complex numerical 3-D counterpart. Finally, we shall present an approximate model to describe the mechanism of oncotic flow across the EGL based upon the fiber matrix structure proposed in Squire et al. (2001) and Weinbaum et al. (2003). This model extends the theory in Anderson and Malone (1974) for cylindrical pores to a sieving fiber layer.

Acknowledgements

I would like to express my deepest gratitude to my mentor, Professor Weinbaum. He has influenced me greatly by his wonderful scientific advice, careful guidance and encouragement. I did not have any background in Biomedical Engineering before I came to City College. I am so excited when I look at the things I have learned and the research projects I have done. Without him, this would have never happened. He taught me how to become a researcher. His enthusiasm for research will influence me forever.

Special thanks to Professors Roger H. Adamson, Stephen C. Cowin, Fitz-Roy E. Curry, Susannah P. Fritton, Bingmei Fu, Peter Ganatos, Latif M. Jiji, John M. Tarbell Maribel Vazquez, and Yiannis Andreopoulos for their invaluable advice and guidance on my study and research.

I am grateful to Carol Bamberger, Patricia Cupid**,** Linda Emedoh and Dahlia Libert for their support. I am also grateful to Mingdong Bi, Yi Duan, Kelly Emerton, Peng Guo, Yuefeng Han, Xiaping Hu, Bo Jin, Qingjun Kong, Xiang Long, Liyuan Mi, Mia M. Thi, Lidan You, Yuliya Vengrenyuk, Huapei Wan, Liyun Wang, Yilin Wang, Qianhong Wu, Savvas Xanthos, Yi Xiong, Shiyun Xu and other fellow graduate students.

Greatest thanks to my husband, Wei Yuan, my parents, my brother, and my parents-in-law for their unconditional love and support. Special thanks to my son, Kelvin Yuan, for all the happiness he has brought to our family.

This research is supported by NIH grant HL 44485.

Contents

List of Tables

List of Figures

Chapter 1 Introduction

While the endothelial glycocalyx was first identified by special electron microscopic staining techniques nearly forty years ago (Luft, 1967), it is only relatively recently that this surface layer has been observed *in vivo* (Vink and Duling, 1996), and the importance of its multifaceted physiological functions recognized. Key among these functions are its role as a molecular sieve in determining the oncotic forces that are established across microvessel endothelium (Michel, 1997; Weinbaum, 1998; Hu and Weinbaum, 1999; Hu *et al*., 2000; Adamson et al, 2004), its role as a transducer of mechanical forces to the intracellular cytoskeleton in the initiation of intracellular signaling (Weinbaum et al., 2003; Thi et al., 2004), a hydrodynamic exclusion layer preventing the interaction of proteins in the red cell and endothelial cell membranes (Feng and Weinbaum, 2000; Secomb *et al*., 2001; Damiano, 1998), and its function in modulating leukocyte attachment and rolling (Zhao *et al*., 2001).

1.1 Quasi-periodic structure of the endothelial glycocalyx

The possible existence of an ordered structure was first proposed in Michel (1983) to explain why there is a sharp break in the solute permeability curve for molecules the size of albumin. Little was known about the specific proteins or generalized structure of the glycocalyx until recently (Squire *et al*., 2001; Henry and Duling, 1999 and 2000; Florian et al., 2003). The state of knowledge prior to 2000 is summarized in (Pries *et al*., 2000). *In vivo* experiments demonstrated that hyaluronan and chondroitin

sulfate play an important role in the assembly of the layer and its sieving properties (Henry and Duling, 2000). Florian et al. (2003) recently verified the presence of heparin sulfate proteoglycan in the glycocalyx of cultured bovine aortic endothelial cells (ECs). Using computed autocorrelation functions and Fourier transforms of EM images obtained from both new (Squire *et al*., 2001) and previous studies (Clough *et al*., 1988) of frog mesenteric capillaries, Squire *et al*. (2001) were able to identify for the first time the quasi-periodic substructure of the glycocalyx and the anchoring foci that appear to emanate from the underlying cortical cytoskeleton. The computer enhanced images showed that the glycocalyx is a three-dimensional fibrous meshwork with a characteristic spacing of 20 nm in all directions and that the effective diameter of the periodic scattering centers was 10-12 nm. Using a freeze fracture replica from a rare section where the fracture plane passed parallel and close to the endothelial surface, they also showed that anchoring foci formed an hexagonal array with an intercluster spacing of typically 100 nm in frog lung capillary. This latter observation was consistent with the spacing of bush like structures seen on the plasmalemma of the fenestrated renal capillaries of the rat using a new fluorocarbon oxygen fixation technique which preserved the portion of the glycocalyx close to the endothelial cell surface (Rostgaard and Qvortrup, 1997).

Based on the foregoing observations Squire *et al*. (2001) proposed a model for the structural organization of the endothelial glycocalyx layer (EGL) and its relationship to the EC cortical cytoskeleton. The model provides a new view of the organization of the matrix that forms the molecular sieve for the filtering of plasma proteins.

1.2 Ultrastucture of the interendothelial cleft in rat

Adamson et al. (2004) has recently obtained detailed measurements for the structural parameters for the tight junction (TJ) in rat mesenteric capillaries. These measurements include the cleft depth, L = 411 nm, the tight junction (TJ) strand depth, L_1=67 nm, the cleft height, 2h=18 nm, the orifice size, 2d =315 nm, and the spacing between adjacent orifices, 2D =3,590 nm. They also measured L_p for rat mesenteric capillaries and obtained values that fell in the range 0.8-1.3×10^{-7} cm/s/cm H_2O.

1.3 Mechanotransduction through the EGL

It is widely recognized that fluid shearing forces acting on ECs have a profound effect on their morphology, structure and function (Davies, 1995; Drenckhahn and Ness, 1997; Weinbaum et al., 2003; Thi et al., 2004). Thi *et al.* (2004) performed a series of experiments to see if the EGL was directly involved in the reorganization of the actin cytoskeleton and the redistribution of various linker proteins in response to fluid shear. Rat fat-pad endothelial cells were exposed to fluid shear stress with an intact or compromised EGL. They observed that a fluid shear stress of 10 dyn/cm^2 with a duration of 5 h disrupts the dense peripheral actin bands (DPABs) and promotes migration of vinculin to cell borders in the case of ECs with an intact glycocalyx. In sharp contrast, such reorganization was completely abolished when the EGL was compromised. The glycocalyx core protein fibers were also shown to amplify the effect of fluid shear stress and produce a sufficient disjoining force on the adherens junction to unzipper the VE-caderins bonds and initiate a disruption of the

DPABs. This behavior is explained in the terms of a ‘bumper car’ model proposed in Thi *et al*. (2004). It is now also clear from theoretical considerations (Feng and Weinbaum, 2000; Damiano, 1998; Secomb *et al*., 1998 and 2001) that the shear stress at the edge of the EGL is greatly attenuated by the extracellular matrix of proteoglycans and glycoproteins in the glycocalyx with the result that fluid velocities, except near the edge of the layer, are vanishingly small. Thus, the shear stress due to the fluid flow acting on the apical membrane of the endothelial cell itself is negligible.

This paradoxical prediction has raised a fundamental question as to how hydrodynamic and mechanical forces, more generally, are transmitted across the structural components of the glycocalyx. How do these components deform under the action of these forces and how are these forces and deformations communicated to the underlying cortical cytoskeleton?

We first address a basic question: what is the bending rigidity *EI* of the core proteins comprising the glycocalyx that enables them to resist the randomizing forces of Brownian motion and deformation by fluid shear stresses? To answer this question we shall examine the time dependent recovery of the surface layer after it has been crushed by the passage of a white blood cell (Vink *et al*., 1999). Theoretical models are then developed to explore the deformability of the matrix in response to fluid shearing forces. The forces and torques exerted on the structural elements of the glycocalyx by these mechanical loads are then used to predict the stresses transmitted to the cortical cytoskeleton.

Using this theoretically estimated *EI*, we will show that the glycocalyx layer

deforms only slightly when subject to shear flow at physiological rates. Therefore, for physiological shear flows this layer provides nearly constant resistance to transcellular fluid and solute transport.

1.4 Oncotic pressures opposing filtration across non-fenestrated rat microvessels

The classic Starling Equation describing the balance of hydrostatic and colloid osmotic (oncotic) forces which determine filtration and reabsorption across the capillary wall includes four forces:

$$J_V / A = L_p \left[P_L - P_T - \sigma_f \left(\pi_L - \pi_T \right) \right], \qquad (1.1)$$

where J_V / A is the fluid filtration flux across the capillary wall per unit area, L_p is the hydraulic permeability, σ_f is the reflection coefficient, and P_L, P_T, π_L and π_T are the global values for the hydrostatic and osmotic pressures in the capillary and interstitial compartments, respectively.

This relation has been tested by changing P_L and π_L (only rarely by changing P_T or π_T) and confirmed many times in both whole organ and isolated microvessels, but usually under conditions where the tissue protein concentration was low, due to wash-down of the tissue proteins after rapid filtration, or washout of tissue protein in exposed superfused tissue (Pappenheimer & Soto-Rivera, 1948; Michel *et al.*, 1974; Granger & Taylor, 1980). Thus the precise contribution of the interstitial Starling forces warrants further study.

In recent years evidence has accumulated that the tissue oncotic pressure may not contribute to the balance of osmotic and hydrostatic forces to the same extent as the

other three forces. Specifically, Levick pointed out that, if the most accurate values for tissue oncotic pressure are substituted into the Starling equation, then most tissues are not in fluid balance, and would filter far more fluid than can be accounted for by measured lymph flows (Levick, 1991). Further, in direct measurements Levick demonstrated in the synovium that tissue albumin had much less effect on fluid exchange than the same concentration administered intravascularly (McDonald & Levick, 1993).

Michel (1997) and Weinbaum (1998) proposed independently that the effective protein osmotic barrier is not the whole capillary wall, but the luminal glycocalyx which acts as the primary molecular filter. If this is the case, the plasma protein concentration in the protected region behind the glycocalyx on the lumen side of the tight junction (TJ) strand between adjacent endothelial cells may be much less than it is in the tissue because the diffusive flux of the plasma protein from the tissue into the cleft is reduced by the convective flow through orifice like breaks in the TJ strand. Our collaborators at UC Davis have conducted elegant experiments to test this hypothesis in detail in mammalian capillaries. They found the effective oncotic pressure difference to be close to 70% of luminal oncotic pressure. Our theoretical model to explain these results provides new evidence that the effective oncotic pressure opposing net filtration in mammalian continuous capillaries is developed across the endothelial glycocalyx and that the oncotic pressure of interstitial fluid does not directly determine fluid balance across microvascular endothelium.

1.5 Simplified model for revised Starling principle

As noted above Michel (1997) and Weinbaum (1998) have proposed that Starling's hypothesis should be applied locally, just across the thin EGL, rather than globally, across the entire endothelial layer, between plasma and interstitium, since the EGL is hypothesized to be the primary molecular sieve for plasma proteins.

Hu and Weinbaum (1999) have developed a sophisticated 3-D model which predicts that the convective flow through the orifice-like breaks in the TJ strand could greatly reduce back diffusion from the tissue into the lumen side of the TJ strand with the result that the oncotic force behind the EGL could be much smaller than the tissue at the cleft exit. This prediction is clearly borne out by the experiments in Hu et al. (2000) for frog microvessls and Adamson et al. (2004) for rat microvessels in which the tissue is back loaded with albumin at the same concentration as the lumen. The experiments demonstrate that at high filtration rates the proteins on the lumen side of the TJ strand are washed out and nearly the full oncotic pressure $\sigma_f \pi_L$ is felt across the EGL in the case of frog microvessels, and ~70 percent of $\sigma_f \pi_L$ in the case of rat microvessels, although the tissue oncotic pressure is isotonic with respect to the luminal oncotic pressure.

The 3-D model in Hu and Weinbaum (1999) is far too complicated for most investigators to conveniently use and requires considerable computer time for the numerical solutions to converge. To overcome these shortcomings we have formulated a much simpler model in which the entire endothelial layer is divided into five regions. Each region is described by a one-dimensional, convection-diffusion

equation which can be solved analytically subject to simplified interface matching conditions. This enables one to reduce the entire boundary value problem to a simple system of algebraic equations for the unknown constants that is easily solved on the computer. The new model has the additional advantage that one can easily assess the relative importance of the EGL and cleft and at the same time examine the effect of different boundary conditions in the tissue.

1.6 Oncotic flow through the EGL

The thermodynamic theory for the osmotic flow through porous membranes is largely based on the movement of water and solute through long circular cylindrical pores (Anderson and Malone, 1974). This theory is applicable to cell membrane proteins with hydrophilic interiors which either allow only the passage of water, such as aquaporins, or have larger channels that permit the passage of water and the restricted convection and diffusion of small solutes. In contrast to this classical theory, Michel (1997) and Weinbaum (1998) have independently proposed that the oncotic forces that are exerted across the capillary wall are due to the sieving of plasma proteins by a fiber like layer of proteoglycans and glycoproteins that comprise the EGL.

Staverman (1951) proposed that the solutes exert their full osmotic pressures across a semipermeable barrier if water can pass freely but solutes are completely restricted. He proposed that only a fraction of this full osmotic force will be exerted by a barrier that is also leaky to solutes, and introduced the concept of a reflection

coefficient, σ_0, to describe this reduced osmotic pressures.

A rigorous theory based on classical transport and thermodynamic relations has been developed by Anderson and Malone (1974) to determine the reflection coefficient for long circular cylindrical pores. For the steric exclusion of spherical solutes they showed that

$$\sigma_0 = (1-\phi)^2, \tag{1.2}$$

where ϕ is the partition coefficient defined as the ratio between the area available to solute and that available to water. However, no equivalent analysis has been developed for a sieving fiber matrix layer. Curry and Michel (1980) suggested an expression identical to Equation (1.2) to describe the reflection coefficient for a fiber matrix

$$\sigma_0 = (1-\phi_f)^2. \tag{1.3}$$

The partition coefficient ϕ_f is defined by the ratio between the area available to the solute and that of a periodic unit of the fiber matrix. Equation (1.3) is an intuitive expression without detailed derivation.

The recent ultrastructural study of Squire et al. (2001) and its model representation in Weinbaum et al. (2003) have led to a major modification of existing views of the 3-D organization of the molecular structures that form the EGL. This new ultrastructural view of the EGL has been the motivation for the development of a theoretical model to describe the reflection coefficient, σ_0, in a fiber matrix layer with this proposed new structure. The pore theory in Anderson and Malone (1974) describes the osmotic flow inside the pores whose driving force is produced by a

radial discontinuity in hydrostatic pressure and concentration due to the steric exclusion of the solutes from the pore walls. Our fiber matrix model describes the oncotic flow around the fibers whose driving force is produced by the discontinuity in hydrostatic pressure and concentration due to the steric exclusion of the solutes at the surface of the fibers. We shall show that the classical expression for circular pores, Equation (1.2), or its intuitive extension to the fiber matrix model, Equation (1.3), is a good approximation only for large solutes and fiber radii, and that a more general expression is required for small and medium sized solutes.

Chapter 2 Mechanical Properties of Surface Glycocalyx Fibers

2.1 Introduction

In this chapter, I develop a mathematical model for estimating the mechanical properties of the endothelial glycocalyx fibers based on existing experimental data. The endothelial surface glycocalyx was first identified by Luft (1966) nearly forty years ago using a ruthenium red electron microscopic staining technique. Due to its sensitivity to chemical staining, the glycocalyx had not been observed *in vivo* until Vink and Duking (1996). More recently Squire et al. (2001) showed that the matrix has an underlying quasi-periodic substructure. This raises a basic question as to how the matrix maintains its periodicity under Brownian motion and when subject to fluid flow at physiological shear rates, as well as how it responds to red and white cell motion.

Figure 2.1A is a modified sketch of the structural model proposed in (Squire et al., 2001) for the organization of the core proteins in the proteoglycan clusters that comprise the glycocalyx and their linkage to the underlying cortical cytoskeleton. This composite structure is deduced from the appearance of bush-like structures that appear to emanate from foci in the cell membrane (Rostgaard and Qvortrup, 1997) and current models of the cortical cytoskeleton (Sako and Kusumi, 1995). Also shown are transcellular actin stress fibers linked by α-actinin tethering the cortical shell to focal adhesion sites of integrins on the basal aspect of the cell and other tethering filaments associated with actin filament bundles in close proximity to the junctional complexes (Davies, 1995; Drenckhahn and Ness, 1997). There is a bidirectional grid with 20 nm periodicity of scattering centers aligned along the axes of the core proteins. There is also a 100 nm periodicity associated

with the separation of each cluster and the observed hexagonal organization of the membrane bound foci. Figure 2.1B is an *en face* view of our idealized model which assumes both an hexagonal arrangement of the core proteins in each cluster and an hexagonal arrangement of the actin filaments in the underlying cortical cytoskeleton. We assume that each membrane foci is connected by short linker molecules at the intersections of the hexagonal actin lattice that forms the cortical network. Based on the length of the cytoplasmic tails and the typical forces exerted by optical tweezers in dragging membrane proteins across domain boundaries, these linkages are both short and relatively rigid (Sako and Kusumi, 1995). The key parameter in determining how the core proteins transmit hydrodynamic and mechanical forces across the surface glycocalyx is their bending rigidity *EI*. In Secomb *et al*. (2001) the bending rigidity of the fibers is neglected and the structural rigidity of the layer is attributed to a weak colloidal osmotic pressure that resists the normal component of the tension that is imposed by the fluid shearing stress. Detailed solutions in Hu et al. (2000) for the protein concentration distribution across the surface glycocalyx show that there is a sharp drop in concentration across the surface glycocalyx even in the presence of back loading of the tissue. Thus, the oncotic pressure in the plasma should be significantly greater and not less than in the surface glycocalyx. This would appear to negate the possibility that an oncotic pressure provides for the structural rigidity of the surface layer.

In this study we propose an alternate hypothesis, namely that that the core proteins have a finite bending rigidity which is sufficient to withstand the bending moments that are created by the drag forces on their tips in the fiber interaction layer. Three observations strongly support this hypothesis. First, it is hard to explain how the

glycocalyx could maintain its periodic structure in the presence of thermal fluctuations due to Brownian motion were it not for a significant bending rigidity of the core proteins. Second, the molecular sieving properties of the glycocalyx described in the section on transport cannot be explained by slender highly flexible glycan sidechains, but are consistent with a more rigid molecular structure associated with the core proteins. Third, the *in vivo* measurements (Vink and Duling, 1996) for L_f and the fluid gap between the edge of the surface layer and the red cell membrane indicate little or no deformation of the surface glycocalyx occurs for red cell velocities > 20 μm/s.

2.2 Estimation of *EI*

Vink *et al*. (1999) observed that the surface glycocalyx layer could be substantially compressed by either the passage of a white blood cell or the arrest of motion of a red blood cell. They measured the time dependent gap between the endothelial cell membrane and that of red blood cells which pass in the wake of the white blood cell. Since neither the fluid space between the outer edge of the compressed glycocalyx layer nor the red cell noticeably change, most of the time dependent change in displacement of the red cell membrane from the endothelial cell surface could be accounted for by the change in thickness of the glycocalyx surface layer. The recovery curve for the glycocalyx layer can be approximately described by a single exponential with a characteristic time of 0.38 sec, as shown in Figure 2.2. We shall determine *EI* by constructing an approximate visco-elastic model for the recovery.

We assume that the roots of each bush-like cluster are firmly anchored by short linker molecules into the underlying cortical cytoskeleton. Therefore, each vertical fiber can be

modeled as a cantilever beam, whose initial loading due to the passage of the white blood cell is approximated as a horizontal force P applied at the tip of the deforming fiber. The energy stored in elastic deformation of the core proteins will be consumed in the viscous dissipation of the recoiling fibers. The local drag on them is proportional to the local instantaneous velocity of the fiber relative to the fluid motion. However, Guo et al. (2000) showed that the fluid trapped in the matrix is almost stagnant except for a thin tip interaction layer, which we shall neglect. The local drag force on the fiber per unit length is therefore linearly related to the local fiber velocity

$$F = \frac{\pi}{c}\frac{\mu r_f^{\,2}}{K_P}U\,, \tag{2.1}$$

where μ is the plasma viscosity, r_f, the fiber radius, U, the local instantaneous velocity of the fiber relative to the fluid motion, K_P, the Darcy permeability, and c the fiber volume fraction, $c = 2\pi r_f^{\,2}/\sqrt{3}\left(2r_f + \Delta\right)^2$. Following the approach in Guo *et al*. (2000), we determine K_P using the solution in Sangani and Acrivos (1982) for the flow past a periodic hexagonal array of cylindrical fibers. For c<0.4,

$$\frac{K_P}{r_f^{\,2}} = \frac{\ln\left(c^{-1/2}\right) - 0.745 + c - c^2/4}{4c}. \tag{2.2}$$

Equation (2.2) describes the hydrodynamic interaction between the fibers. If $y(x,t)$ is the local deflection of the fiber, then $U = \partial y/\partial t$.

For small deflections, the visco-elastic recoil of a fiber in a viscous fluid can be described by modified beam equation in the form of

$$EI\frac{\partial^4 y}{\partial x^4} = -\frac{\pi}{c}\frac{\mu r_f^{\,2}}{K_P}\frac{\partial y}{\partial t}, \tag{2.3}$$

where the coordinate system and local instantaneous velocity are shown in Figure 2.3. In solving Equation (2.3), we neglect the change in K_P with time as the glycocalyx expands and non-linear effects of large deformation. Since the final phase of the recoil is described by the long time mode for the fiber recovery and not the rapid initial phase of large deformation, Equation (2.3) should provide a reasonable lowest order approximation for the recovery time.

Equation (2.3) can be cast in dimensionless form

$$Y_{XXXX} = -Y_T \,, \tag{2.4}$$

by introducing the dimensionless coordinates $X = x/L$ and $Y = y/y(L,0)$, and dimensionless time $T = t/\tau$, where $\tau = kL^4/EI$. $k = (\pi/c)(\mu r_f{}^2/K_P)$.

Equation (2.4) satisfies the dimensionless boundary and initial conditions:

$$Y(0,T) = \frac{\partial Y(0,T)}{\partial X} = \frac{\partial^2 Y(1,T)}{\partial X^2} = \frac{\partial^3 Y(1,T)}{\partial X^3} = 0 \,, \tag{2.5a, b, c, d}$$

$$Y(X,0) = \frac{3}{2}X^2 - \frac{1}{2}X^3 \,, \tag{2.5e}$$

where Equation (2.5e) is the initial deflection due to a point load applied at X=1. The viscous loading term on the right hand side of Equation (2.4) is expressed in an infinite series of the form

$$-\frac{\partial Y}{\partial T} = a_2(T)\cdot X^2 + a_3(T)\cdot X^3 + a_4(T)\cdot X^4 + a_5(T)\cdot X^5 + a_6(T)\cdot X^6 + a_7(T)\cdot X^7 + \ldots \,, \tag{2.6}$$

where the $a_i(T)$, i = 2, 3, 4 … are unknown time dependent functions. Substituting Equation (2.6) into Equation (2.4), integrating term by term and applying the first two boundary conditions (2.5a, b), one finds that

$$Y(X,T) = f_2(T)\cdot\frac{X^2}{2} + f_3(T)\cdot\frac{X^3}{6} + a_2(T)\cdot\frac{X^6}{360} + a_3(T)\cdot\frac{X^7}{840} + a_4(T)\cdot\frac{X^8}{1680} + a_5(T)\cdot\frac{X^9}{3024}$$

$$+a_6(T)\cdot\frac{X^{10}}{5040} + a_7(T)\cdot\frac{X^{11}}{7920} + \ldots, \qquad (2.7)$$

where $f_2(T)$ and $f_3(T)$ are also unknown functions of time. Differentiating Equation (2.7) with respect to T, provides another way to express Y_T, which is equivalent to Equation (2.6). Comparing the coefficients of X^n in these two expressions for Y_T, one obtains the following relationships between the $a_i(T)$ and $f_2(T)$ and $f_3(T)$

$$a_2(T) = -\frac{f_2'(T)}{2}, \qquad (2.8a)$$

$$a_3(T) = -\frac{f_3'(T)}{6}, \qquad (2.8b)$$

$$a_4(T) = a_5(T) = 0, \qquad (2.8c, d)$$

$$a_6(T) = -\frac{a_2'(T)}{360} = \frac{f_2''(T)}{720}, \qquad (2.8f)$$

Therefore, Equation (2.7) can be rewritten as

$$Y(X,T) = f_2\cdot\frac{X^2}{2} + f_3\cdot\frac{X^3}{6} - f_2'\cdot\frac{X^6}{720} - f_3'\cdot\frac{X^7}{5040} + f_2''\cdot\frac{X^{10}}{5040\times720} + f_3''\cdot\frac{X^{11}}{5040\times7920} + \ldots \qquad (2.9)$$

Conditions (2.5c), d require that $f_2(T)$ and $f_3(T)$ satisfy,

$$f_2 + f_3 - \frac{f_2'}{24} - \frac{f_3'}{120} + \frac{f_2''}{5040\times8} + \frac{f_3''}{5040\times72} + \ldots = 0, \qquad (2.10a)$$

$$f_3 - \frac{f_2'}{6} - \frac{f_3'}{24} + \frac{f_2''}{5040} + \frac{f_3''}{5040\times8} + \ldots = 0, \qquad (2.10b)$$

where higher order terms are neglected since Equation (2.9) converges rapidly. Terms involving f_2" and f_3" are also neglected because they introduce inertia which is very small in a viscous dominated flow. The coupled equations for f_2 and f_3 thus simplify to

$$\frac{1}{2880}\cdot\frac{d^2 f_3}{dT^2}+\frac{1}{12}\frac{df_3}{dT}+f_3=0. \tag{2.11}$$

Assuming a solution for f_3 of the form

$$f_3(T)=A\cdot e^{-\frac{T}{\xi}}, \tag{2.12}$$

and substituting it into Equation (2.11), one finds

$$1-\frac{\xi}{12}+\frac{\xi^2}{2880}=0, \tag{2.13}$$

whose roots are $\xi_1=0.0044$ and $\xi_2=0.0789$.

The solution for f_3 is

$$f_3(T)=A_1 e^{-\frac{T}{\xi_1}}+A_2 e^{-\frac{T}{\xi_2}}. \tag{2.14}$$

Then, the simplified version of Equations (2.10a) and (2.10b) gives

$$f_2(T)=-\frac{3}{4}f_3-\frac{1}{480}f_3'=\frac{1}{4}A_1 e^{-\frac{T}{\xi_1}}\left(\frac{1}{120\xi_1}-3\right)+\frac{1}{4}A_2 e^{-\frac{T}{\xi_2}}\left(\frac{1}{120\xi_2}-3\right). \tag{2.15}$$

A_1 and A_2 are the integration constants which can be determined by applying the initial condition 2.5e.

$$A_1=-\frac{3\xi_1(-1+120\xi_2)}{-\xi_2+\xi_1}, \tag{2.16a}$$

$$A_2=\frac{3\xi_2(-1+120\xi_1)}{-\xi_2+\xi_1}. \tag{2.16b}$$

It should be pointed out that only first two terms in Equation (2.9) are required to satisfy initial condition (2.5e).

$\xi_1 \cdot \tau$ is the short dimensional time constant which accounts for the initial transient change in fiber shape after the point force *P* is released. $\xi_2 \cdot \tau$ is the long dimensional time constant which describes the long time recoil. We require the long time constant be equal to the single exponential, β=0.38 sec, obtained by curvefitting the experimental data in Vink *et al.* (1999). Hence,

$$EI = \frac{\xi_2}{\beta} \frac{\pi}{c} \frac{\mu r_f^{\,2}}{K_P} L^4, \tag{2.17}$$

where *L* is the fiber length, 400 nm. This leads to our theoretical prediction that *EI*=700 pN·nm^2. In comparison, the measured values of *EI* for an actin filament vary between 15 $\times 10^3$ pN·nm^2 (Dupuis *et al*., 1997) and 73×10^3 pN·nm^2 (Gittes *et al*., 1993). One observes that *EI* for an actin filament is at least 21 fold greater than the core proteins. Thus, if the core proteins are anchored into the cortical cytoskeleton through a transmembrane protein complex, as sketched in Figure 2.1, this supporting structure will be much stiffer than the core proteins in the surface glycocalyx. This justifies our use of a cantilever beam model in solving Equation (2.3).

2.3 Deflections of core proteins due to fluid shear

The hydrodynamic loading on the core proteins given by Equation (2.1) can be used to predict their deformation when subject to fluid shear. Following the analysis described in Guo *et al*. (2000), one can split the total loading into two contributions, a concentrated load *P* applied at *x*=*L*, due to the fluid drag associated with the tip interaction layer and a

uniformly distributed load q associated with the much slower pressure driven flow in the interior of the glycocalyx layer. One obtains the following simple expression for the shape of the fiber, using classical beam theory,

$$y(x) = \frac{1}{EI}\left[\frac{P}{6}\left(-x^3 + 3Lx^2\right) + \frac{q}{24}\left(x^4 - 4Lx^3 + 6L^2x^2\right)\right]. \tag{2.18}$$

Equation (2.18) has been plotted in Figure 2.4 for fibers ranging in length from 150 nm, the glycocalyx layer thickness observed in Squire *et al*. (2001) for frog mesentery capillary, to 400 nm, the thickness of the excluded fluorescent dextran layers observed in Vink and Duling (1996) for hamster cremaster. Results are shown for a fluid shear stress of 10 dyn/cm^2 at the edge of the glycocalyx layer and a bending rigidity EI = 700 pN·nm^2. The tip deflection of the longest fiber is only 17.9 nm. Thus, all deflections are well within the limits of small deflection theory. The important conclusion is that the fibers have sufficient flexural rigidity to resist bending at fluid shear stresses in the physiological range and, as observed in Vink and Duling (1996) and Henry and Duling (1999), there is no observable deformation of the glycocalyx layer due to fluid shear.

A simple model for the deformation of the surface glycocalyx is developed in Weinbaum *et al*. (2003) when the red cell is gliding above its outer edge at velocities > 20 μm/s. The novel feature of their solution is that the increase in the fluid gap δ as a function of the red cell velocity U_{RBC} has been estimated using the measured data in Fig.3 of (Vink and Duling, 1996). This allows them to circumvent the much more difficult problem of developing a model for finding the change in red cell shape as a function of its velocity and capillary diameter when their primary interest is the forces and bending moments on the vertical fibers and their deformation. They found that the magnitude of the tip deflection at 210 μm/s for a 400-nm fiber is about 8 nm, one half that shown in

Figure 2.4 for a shear stress of 10 dyn/cm^2, but decreases rapidly as the red cell velocity and fluid gap δ decrease.

2.4 Buckling of core proteins due to arrest of red blood cell motion

Vink and Duling (1996) observed that when the red blood cell motion is arrested, the cell expands to fill nearly the entire capillary lumen. During the red blood cell expansion, the glycocalyx fibers buckle, and the water within the matrix slowly drains. One may ask how much resistance comes from the buckling of the fibers, and how much from the water drainage through the compressed matrix.

The governing equation for the bending of a curved beam whose initial shape is given by a curve $y_o(x)$ subject to a compressive force P acting at its end, as shown in Figure 2.5, is

$$EI\frac{d^2(y-y_0)}{dx^2} = P(\delta - y), \tag{2.19}$$

where δ is the unknown tip deflection after the load P is applied. A simple approximate description of the initial shape of the fibers in Figure 2.1A is $y_0(x) = \delta_0 \sin(\alpha x)$ where $\alpha = \pi / 2L_f$, and δ_0 is the initial tip deflection. The solution of Equation (2.19) which satisfies the boundary conditions $y(0) = 0$ and $y'(0) = \delta_0\alpha$ is

$$y(x) = \delta - \delta\cos(\lambda x) + \frac{\delta_0\alpha\lambda}{\lambda^2 - \alpha^2}\sin(\lambda x) - \frac{\delta_0\alpha^2}{\lambda^2 - \alpha^2}\sin(\alpha x), \tag{2.20}$$

where $\lambda = \sqrt{P/EI}$. If we now require that $y(L) = \delta$ in Equation (2.20), then the unknown tip deflection is given by

$$\delta = \frac{\delta_0 \alpha}{\lambda^2 - \alpha^2} \frac{\lambda \sin(\lambda L) - \alpha \sin(\alpha L)}{\cos(\lambda L)}. \tag{2.21}$$

We draw a distinction between L and the surface glycocalyx thickness, L_f, because later in the proposal we will consider large changes in L_f in which L is unchanged.

The tip deflection given by Equation (2.21) is plotted in Figure 2.6A for the case where L = 0.4 μm and EI = 700 pN·nm^2. The critical load for the buckling of a straight fiber using small deflection theory is $P_{cr} = \alpha^2 EI$. For the foregoing values of L and EI, P_{cr} = 0.0108 pN. Elastica theory (Timoshenko, 1988) for large deformations must be used to determine the displacement for this critical load since small incremental loads above P_{cr} will cause large deflections. This result using elastica theory is given by the uppermost curve in Figure 2.6A. One observes that fibers that are initially not straight will support compressive loads that are far smaller than P_{cr}. Returning to Figure 2.1B one observes that on average 27 core proteins terminate in each cluster foci taking into account shared proteins at hexagonal cluster boundaries. Surrounding each central core protein there are 6 core proteins in the first hexagon, 12 in the second hexagon and 18 in the outer border hexagon, 12 of which are shared by two clusters and 6 of which are shared by 3 clusters. The maximum compressive force that could be supported by each bush like structure is ≈ 0.3 pN if each fiber could support the critical load. However, most of the fibers are either initially bent or loaded off axis with the result that they carry a load that is far less than the critical load. For fibers that are initially bent there is no critical load.

Using the results in Figure 2.6A one can construct a simple model to estimate the increase in normal force that would be exerted by each 27-fiber cluster if the glycocalyx layer was subject to a uniform compression by a planar surface. One assumes that each

fiber extends to the edge of the surface glycocalyx during the compression and the vertical displacement of each fiber is the same. The tip deflection δ in Equation (2.21) is adjusted to satisfy this constraint and the deformed shape of the fiber is given by Equation (2.20). The downward (vertical) displacement of the fiber is determined by requiring that the initial fiber length L be conserved, which is given by

$$\int_0^{L_{f0}} \sqrt{1+\left(\frac{dy_0}{dx}\right)^2}\,dx = L\,, \tag{2.22}$$

where L_{f0} is the initial glycocalyx layer thickness. Therefore,

$$\int_0^{L_f} \sqrt{1+\left(\frac{dy}{dx}\right)^2}\,dx = L\,, \tag{2.23}$$

where L_f is the glycocalyx layer thickness when the compressive force P is applied at the tip. Then, $\left(L_{f0} - L_f\right)$ is the fiber deflection in the normal direction due to P.

To simplify the model for a fiber cluster we assume that the fibers are arranged in three concentric circles rather than hexagons about the central core protein. The initial tip deflections are 20, 40 and 60 nm in each circle. The increase in normal force as a function of the downward displacement of a fiber in each of the three concentric circles is plotted in Figure 2.6B. These results are shown for vertical deflections up to 100 nm since Equations (2.20) and (2.21) are limited by the assumptions of small deflection theory. However, the curve for the central core protein is given by elastica theory for large deflections and this result provides a useful upper bound. The right hand ordinate in Figure 2.6B provides the summation of the normal forces exerted by all 27 fibers in a cluster foci. For a downward displacement of 100 nm the compressive force on a cluster would be 0.15 pN or about 1/2 of the maximum compressive force of 0.3 pN cited

previously. Since the *en face* area of each cluster is 9.4×10^3 nm^2, the resisting pressure of the fibers for this deflection is 160 dyn/cm^2. At the same time, the cell pressure necessary to squeeze the water out of the matrix is at least 2,420 dyn/cm^2 (Weinbaum *et al*., 2003), a pressure which is much larger than the pressure provided by the fibers.

2.5 Discussion

An important prediction of this study is the bending stiffness of the core proteins in the bush-like clusters that decorate the endothelial surface. The value of *EI*, 700 pN·nm^2, predicted by our model for the restoration of the glycocalyx layer after the passage of a white blood cell is at least 20 times less than the measured *EI*, 15×10^3 (Dupuis *et al*., 1997) ~73×10^3 (Gittes *et al*., 1993), for actin filaments, but sufficiently stiff to resist large deformations of the glycocalyx due to both fluid shear stresses in the physiological range and shear stresses due to the passage of red blood cells. The tip deflections predicted for a shear stress of 20 dyn/cm^2 in small arterioles would be twice those shown in Figure 2.4 or about 35 nm for a fiber of 400 nm long. The much larger value of *EI* for the actin filaments in the underlying cortical cytoskeleton indicates that it provides a firm support for the short linker molecules that attach the transmembrane proteins at the base of each bush-like cluster to the submembrane scaffold. We propose that it is these root-like connections which firmly anchor the fiber clusters.

When blood is flowing within the capillary at a physiological rate, the glycocalyx layer, as already shown, is almost intact. The fluid velocities within the surface glycocalyx, except near the edge of the layer, are vanishingly small. Thus, the shear stress due to the fluid flow acting on the apical membrane of the endothelial cell itself is negligible. We

also note that the drag on a single core protein, 7.0×10^{-4} pN at a shear stress of 10 dyn/cm^2, is far too small to produce a significant deformation of the actin boundaries, but the entire bush-like core protein structure in Figure 2.1 experiences a drag force of 1.9×10^{-2} pN, a force that would result in a 6 nm lateral displacement of an actin boundary since its spring constant is 3×10^{-3} pN/nm (Sako and Kusumi, 1995). However, more revealing is the bending moment on the entire bush, 6.2 pN·nm (Weinbuam *et al*., 2003). The long lever arm provided by the core proteins leads to a mechanical advantage that substantially amplifies the drag forces on the core protein tips when they are transmitted to the cortical cytoskeleton. A simple moment calculation applied to the actin network in Figure 2.7 reveals that a vertical shear force of 0.045 pN would be experienced by the actin fibers, for a shear stress of 10 dyn/cm^2. This would correspond to an elastic recoil of 15 nm for a spring constant of 3×10^{-3} pN/nm. It is clear from this calculation that the mechanical advantage obtained by applying a small force at the tips of the core proteins provides sufficient leverage to deform the underlying cortical cytoskeleton. Our model predicts that, collectively, but not individually, the core proteins in the bush-like structures in Figure 2.1A are ideally suited to act as mechanotranducers that convert fluid shearing stresses at the edge of the surface glycocalyx to deformations of the cortical cytoskeleton. We suggest that this is the initial activating step in intracellular signaling.

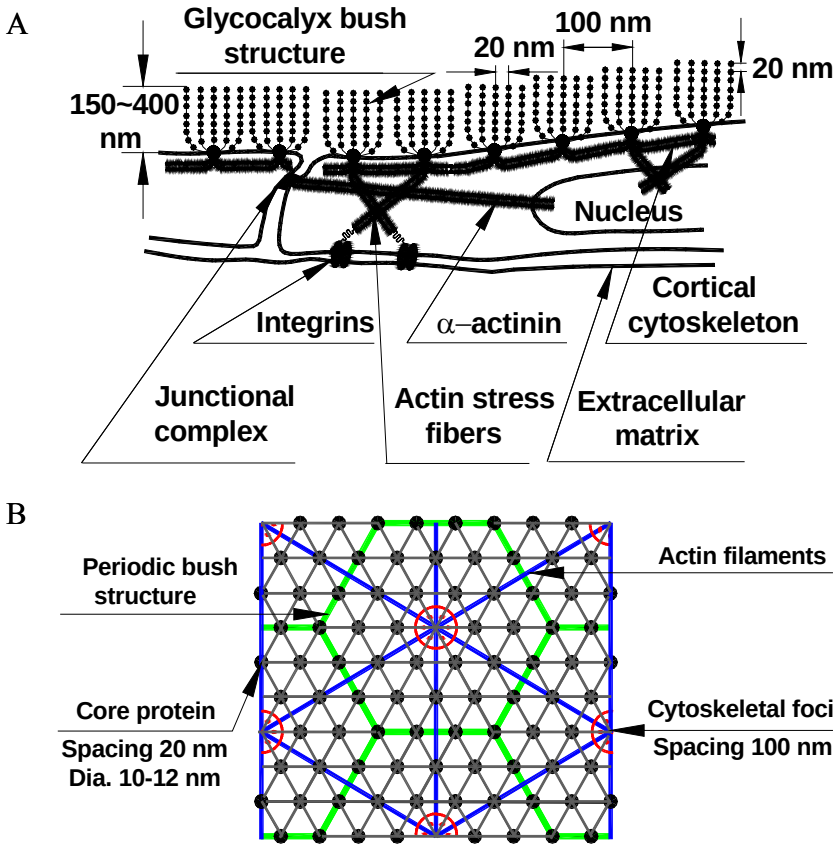

Figure 2.1 A. Sketch of surface glycocalyx (not to scale) showing core protein arrangement and spacing of scattering centers along core proteins and their relationship to actin cortical cytoskeleton as proposed in (Squire et al., 2001). B. *En face* view of idealized model for core protein clusters and cluster foci and their relationship to hexagonal actin lattice in cortical cytoskeleton.

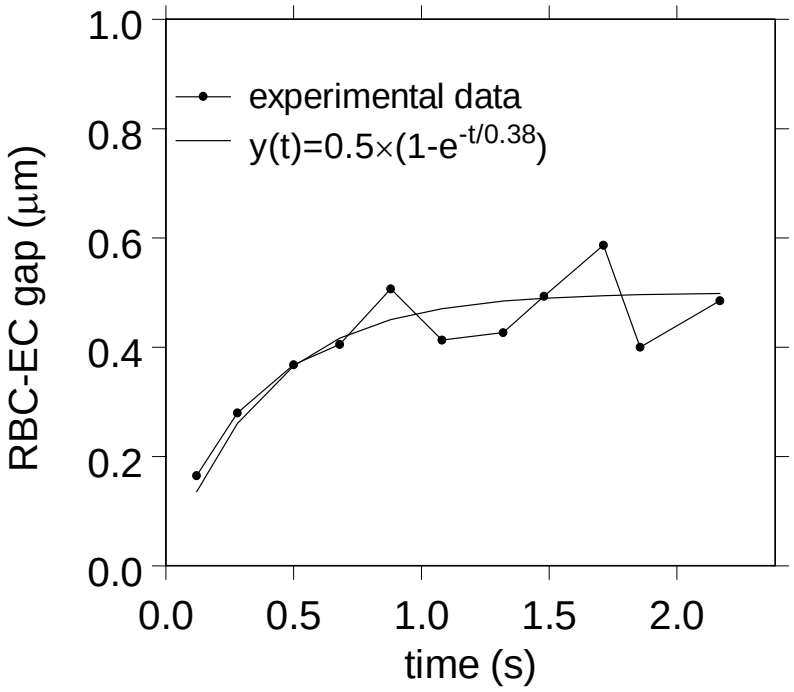

Figure 2.2 Curve fitting of the experimental data for glycocalyx recovery after white blood cell passage. The characteristic time constant obtained is used to determine the *EI* for core proteins of surface glycocalyx using our theoretical model.

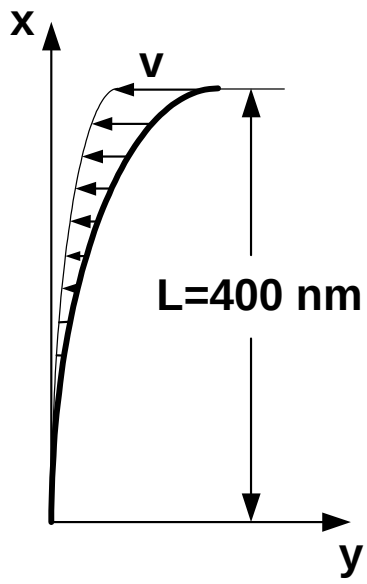

Figure 2.3 Coordinate system used to describe the visco-elastic recoil of a fiber. v is the instantaneous fiber velocity.

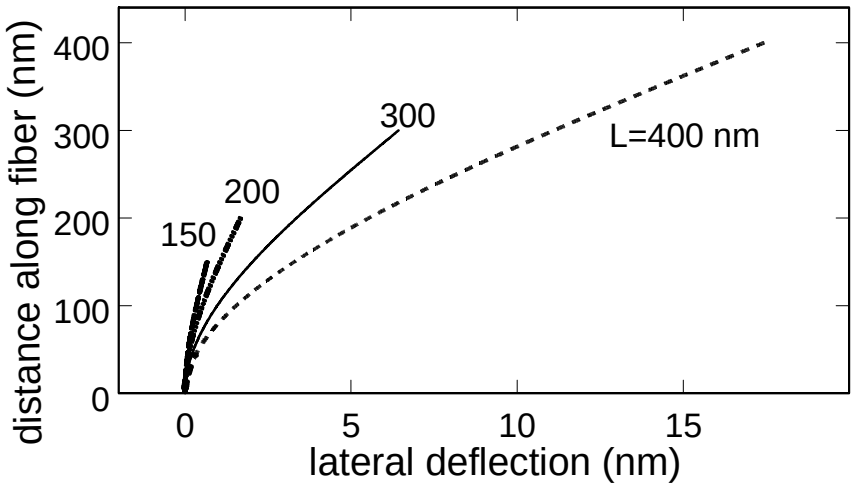

Figure 2.4 Model predictions for lateral deflection of core proteins of different lengths L for a fluid shear stress of 10 dyn/cm2 at glycocalyx edge. *EI* = 700 pN•nm2.

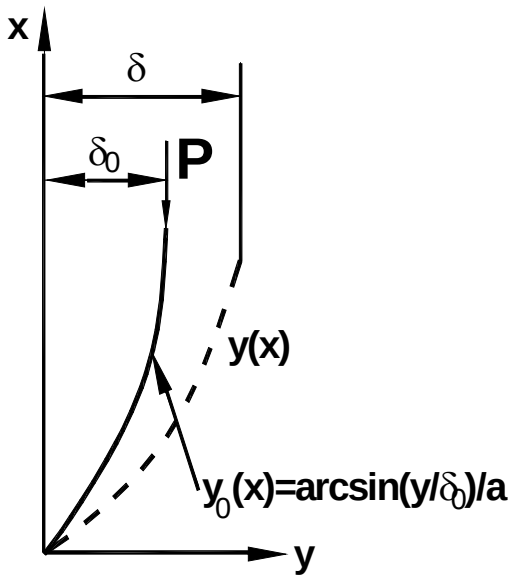

Figure 2.5 Coordinate system used to describe the deformation of an initially curved fiber after a compressive load *P* is applied at the tip. The initial shape of the fiber is described by a simple expression for convenience, where $\alpha=\pi/2Lf$, and $\delta 0$ is the initial unloaded tip deflection from vertical.

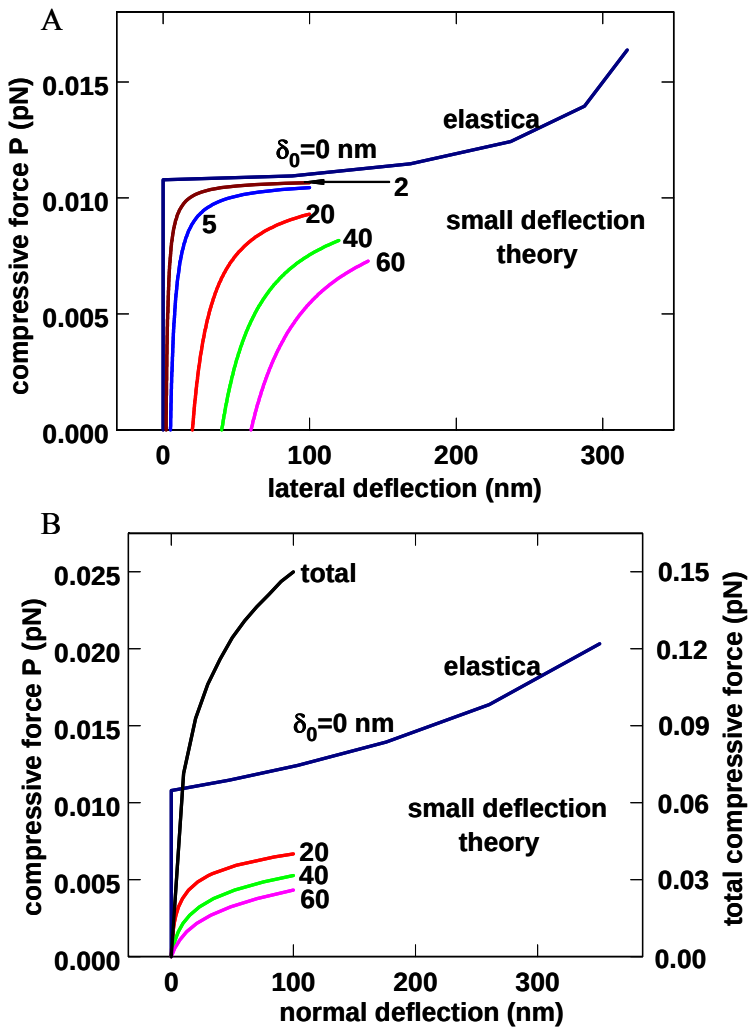

Figure 2.6 A. Predictions of Equation 2.20 for lateral tip deflection due to buckling of core proteins subject to a normal load *P* applied at their ends. *d*o is the initial unloaded tip displacement from vertical shown in Figure 2.5. Curve for *d*o = 0 is "elastica" theory prediction for large deflections (Timoshenko, 1988). B. Results in panel A converted to normal displacement of glycocalyx fibers. Right ordinate is the compressive force for 27 fiber model for core protein cluster in Figure 2.1B.

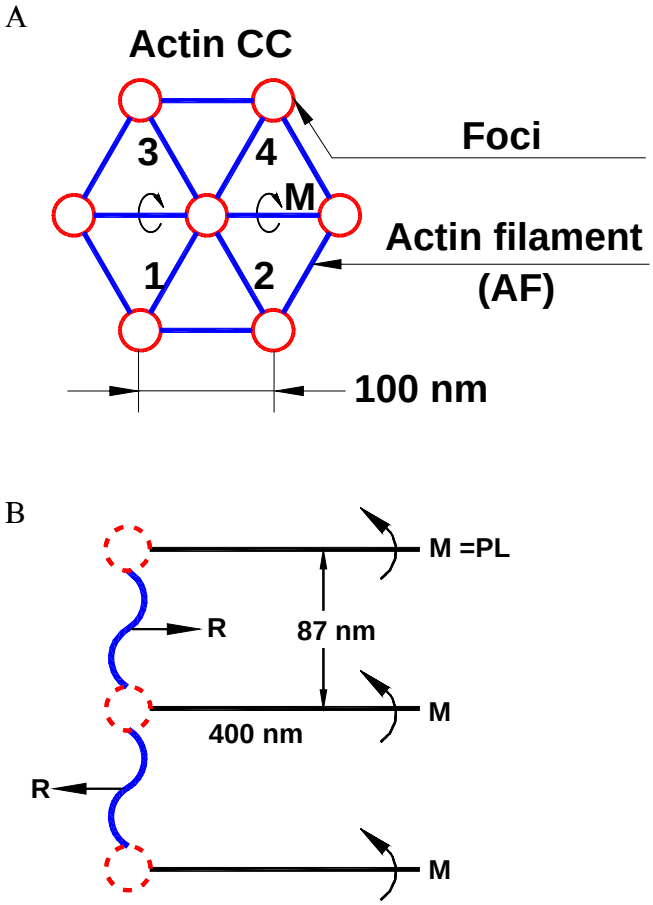

Figure 2.7 Sketch of the underlying cortical cytoskeleton (not to scale) showing how the drag forces on core protein tips are amplified when they are transmitted to the cortical cytoskeleton.

Chapter 3 Oncotic Pressures Opposing Filtration across Non-fenestrated Rat Microvessels

3.1 INTRODUCTION

The classic Starling Equation describing the balance of hydrostatic and colloid osmotic (oncotic) forces which determine filtration and reabsorption across the capillary wall includes four forces:

$$J_V / A = L_p \left[P_L - P_T - \sigma_f \left(\pi_L - \pi_T \right) \right], \tag{3.1}$$

where J_V / A is the fluid filtration flux across the capillary wall per unit area, L_p is the hydraulic permeability, σ_f is the reflection coefficient, and P_L, P_T, π_L and π_T are the global values for the hydrostatic and osmotic pressures in the capillary and interstitial compartments, respectively.

This relation has been tested by changing P_L and π_L (only rarely by changing P_T or π_T) and confirmed many times in both whole organ and isolated microvessels, but usually under conditions where the tissue protein concentration was low, due to wash-down of the tissue proteins after rapid filtration, or washout of tissue protein in exposed superfused tissue (Pappenheimer & Soto-Rivera, 1948; Michel *et al.*, 1974; Granger & Taylor, 1980). Thus the precise contribution of the interstitial Starling forces warrants further study. With respect to interstitial oncotic pressure, filtration of normally low protein concentration fluid into interstitium tends to diminish π_T by dilution of the interstitial fluid. This change opposes further increase in fluid filtration, providing a buffering or moderating influence on fluid filtration. The latter idea,

incorporated into the concepts of safety factors against oedema, resulted from direct measurements of interstitial pressure and interstitial fluid composition (Guyton, 1963; Aukland & Reed, 1993).

Over recent years evidence has accumulated that the tissue oncotic pressure may not contribute to the balance of osmotic and hydrostatic forces to the same extent as the other three forces. Specifically, Levick pointed out that, if the most accurate values for tissue oncotic pressure are substituted into the Starling Equation, then most tissues are not in fluid balance, and would filter far more fluid than can be accounted for by measured lymph flows (Levick, 1991). Further, in direct measurements Levick demonstrated in the synovium that tissue albumin had much less effect on fluid exchange than the same concentration administered intravascularly (McDonald & Levick, 1993).

Michel (1997) and Weinbaum (1998) proposed independently that the effective protein osmotic barrier is not the whole capillary wall, but the luminal glycocalyx which acts as the primary molecular filter. If this is the case, the plasma protein concentration on the tissue side of the glycocalyx in the junction between adjacent endothelial cells may be much less than it is in the tissue because the diffusive flux of the plasma protein from the tissue into the cleft is reduced. In particular, the degree of reduction depends on the velocity of the ultrafiltrate in the cleft distal to the glycocalyx. Thus the concentration difference of the plasma protein across the glycocalyx may be much larger than that estimated from the plasma to tissue concentration difference. The effectiveness of this mechanism depends on the

geometry of the filtration path in the cleft, and on the gradients of tissue plasma proteins near the tissue side of the vascular wall.

A detailed model of the albumin concentration gradients across the glycocalyx and in the cleft between adjacent endothelial cells was developed by Hu and Weinbaum, based on the carefully measured geometry of the size and frequency of junction strand breaks in frog mesenteric microvessels (Adamson and Michel, 1993; Hu and Weinbaum, 1999). In this previous paper the authors directly compared the prediction of a 3-dimensional model of filtration through a fiber-matrix-junctional break model after loading the tissue with serum albumin at a concentration of 50 mg/ml, and perfusing a vessel with albumin at the same concentration. They found that there was no significant difference between the oncotic pressure exerted by the perfusate when there was no albumin in the tissue and when albumin was in the tissue at the same concentration as in the lumen (Hu et al., 2000). The key observation is that albumin is filtered at the glycocalyx, and the ultrafiltrate with its low concentration of albumin is funneled into infrequent breaks in the junction strand so that the water velocity at these breaks reduces the flux of albumin from tissue toward the glycocalyx, even when filtration rates are quite low.

Our collaborators at UC Davis, R. H. Adamson and F. E. Curry, have conducted elegant experiments to test this hypothesis in detail in mammalian capillaries. Little information about the size and frequency of breaks in the junctional strand was available for mammalian capillaries when they began this investigation. In fact, the series of serial sections reported by Bundgaard, on rat heart microvessels, focused on

very small breaks in the junction strand that might act as molecular filters and provided no detailed data on the few larger breaks that were noted in rat heart (Bundgaard, 1984).

There are several key steps in the evaluation of this new hypothesis experimentally. The first step was to measure oncotic pressure across rat mesenteric microvessels perfused with albumin at a concentration of 50 mg/ml, with and without albumin at the same concentration in the superfusate. The second step was to carry out detailed reconstructions of the organization of the junction strands in the microvessels from serial sections. All reconstructions have been carried out on microvessels in which the hydraulic conductivity was also measured. The final important step was to directly measure the gradients of albumin in the tissue around the microvessels during both high and low filtration rates. The microvessels R. H. Adamson and F. E. Curry have studied have hydraulic conductivities similar to those of rat heart, and overlap the range of L_p values reported for mammalian skeletal muscle and skin (Renkin, 1977). Their results provide new evidence that the effective oncotic pressure opposing net filtration in mammalian continuous capillaries is developed across the endothelial glycocalyx and that the oncotic pressure of interstitial fluid does not directly determine fluid balance across microvascular endothelium.

3.2 METHODS

Our theoretical model for the prediction of L_p and the steady state concentration profiles in the cleft and tissue for rat mesentery venules is shown in Figure 3.1. This model is based on the morphometric measurements summarized in Table 3.1 taken from Adamson et al. (2004) and the mean values of L_p and σ to albumin found in the present *in vivo* measurements. In the current mathematical model, σ of the glycocalyx is assumed to equal the value found in our *in vivo* measurements. Key dimensions for the cleft geometry are shown in the figure. This basic model differs from that used previously for frog mesentery capillary in two important respects (Hu & Weinbaum, 1999; Hu *et al.*, 2000). First, the present morphological observations and the previous studies by Schulze & Firth (1992) on mammalian heart capillaries indicate localized regions of cleft spanning structures that might fill the entire cleft. These could be cadherins or an equivalent molecule that is responsible for the remarkably uniform gap height of the cleft outside of the junctional region. Based on the extensive measurements in Schulze and Firth (1992) we have assumed in this chapter that the cleft spanning molecules are spaced in an hexagonal array at 15 nm intervals and their diameter is taken as 2.5 nm, the diameter of cadherins (Shapiro *et al.*, 1995; Boggon *et al.*, 2002). Second, the tight junction strand has been located asymmetrically in the cleft, only 15 percent of the cleft depth or 67 nm from the apical margin of the cell. In previous studies on frog mesentery (Hu and Weinbaum, 1999; Hu et al., 2000) the authors had for convenience placed the strand midway between apical and basal aspects of the cleft. Based on an earlier mathematical model in the appendix to Adamson and Michel (1993), where the endothelial glycocalyx was omitted, it was

shown that the effect of the location of the junction strand had little effect on L_p. However, we have found that the location of the junction strand relative to the glycocalyx does have a significant effect on L_p since it can create a narrow water channel on the apical side of the junction strand through which fluid streamlines must pass if the strand is located close to the apical margin (Weinbaum *et al.*, 2003).

The only unknown in the 3-D model, if the EGL thickness, L_F, is prescribed, is K_P, the Darcy permeability for the EGL. K_P is then determined by satisfying the measured value of L_p=1.3x10^{-7} cm/s/cm H_2O for rat mesenteric capillaries (Adamson et al., 2004). Using the structural parameters for the cleft in Table 3.1 and L_F=150 nm, one finds that K_P =30 nm^2. The flow in the wide part of the cleft, where we assume an hexagonal array of cleft spanning structures, is described using a Brinkman equation (Tsay & Weinbaum, 1991). Since the spacing of the structures, 15 nm, is of the same order as the measured gap height of the cleft, 18 nm, the fiber interaction layers near the plasma boundaries must be considered in determining the effective Darcy permeability K_p of the cleft. Once this effective K_p is determined, the governing equation for the flow in the cleft can be treated as a two-dimensional Darcy flow satisfying a potential flow equation for the pressure field. The junction strand itself is treated as an impermeable boundary for both water and solute. The treatment of the flow in region B, the region surrounding the cleft exit and the tissue space in the far field is the same as summarized previously (Hu & Weinbaum, 1999).

3.3 RESULTS

3.3.1 Ultrastructural data for rat mesenteric capillaries

Our collaborator at UC Davis, Dr. Adamson, has carefully performed the serial section electron microscopy and segment reconstruction for rat mesenteric capillaries. He obtained, for the first time, the detailed morphometric data for the interendothelial clefts in mammalian capillaries. This data summarized in Table 3.1 provides the geometrical ultrastructural information for our model.

3.3.2 Effective oncotic pressure with and without high extravascular albumin

Figure 3.2 taken from Adamson et al. (2004) shows the results of a single experiment in which J_v/A was measured in a rat mesenteric venular microvessel perfused with solution containing BSA (50 mg/ml) having π_i equal to 27 cmH_2O. Measurements were made first when the superfusate was protein-free Ringer solution. Under these conditions with no albumin in the superfusate and π_p equal to 0 cmH_2O, the intercept on the pressure axis measured the effective oncotic pressure (24 cmH_2O) due to albumin in the perfusate and the L_p was 1.2×10^{-7} $cm/s/cmH_2O$ (solid line). Then we changed the superfusate to one containing BSA (50 mg/ml) so that there was no albumin concentration difference between lumen and interstitium and again measured J_v/A. Under these latter conditions ($\pi_t = \pi_p$), we predicted, according to the classic Starling Equation, that the pressure intercept should go through the origin and the slope (L_p) would be unchanged (dotted line). While the L_p (1.3×10^{-7} $cm/s/cmH_2O$) was not different from expectation, we found the effective oncotic pressure was 17 cmH_2O (dashed line).

Adamson et al. (2004) also showed using confocal microscopy that there was no significant change in the albumin concentration near the microvessel after increasing the filtration rate, indicating that increased filtration did not significantly dilute the concentration of extravascular albumin near the microvessel wall.

3.3.3 Steady state filtration at multiple pressures

Figure 3.3 taken from Adamson et al. (2004) shows that for all the lumen pressures which they examined, the measured J_v/A at steady state was substantially less than the value expected indicating that albumin oncotic pressure on the downstream side (tissue side) of the sieving structure in the vessel wall was substantially lower than the luminal value.

3.3.4 Model prediction for the steady state albumin concentration gradient

Figure 3.4 shows the model predictions for the albumin concentration through the cleft and tissue along the center line of a periodic junction strand break ($y = 0$), near the edge of the strand break ($y = d$ =158 nm) and at the edge of the periodic unit ($y = D$ = 1795 nm). Figure 3.4A is for a low filtration state P_L of 30 cmH_2O in which a steady state has been achieved after the tissue has been equilibrated with albumin in the superfusate by damaging the mesothelium 100 μm from the microvessel and allowing albumin to diffuse into the tissue around the microvessel. One observes that the concentration in the tissue just outside the cleft exit is reduced by only 10% from the superfusate concentration, yet the concentration on the lumen side of the junction strand beneath the glycocalyx is reduced by near 45% from the lumen value. Figure 3.4B is for a high filtration state where the lumen pressure is 60 cmH_2O. Note that the

predicted albumin concentration on the lumen side of the junction strand is only about 25% that in the superfusate or lumen. The convective flow through the break in the junction strand is sufficiently strong to greatly hinder diffusive flux of albumin from the tissue space into the protected space on the tissue side of the glycocalyx. The effective oncotic pressure driving the flow is approximately 75% the total oncotic pressure in the lumen of the vessel. In both cases the effective oncotic difference, the difference across the glycocalyx, is much greater than the difference between lumen and tissue.

3.4 Discussion

Both the experiments to measure the effective osmotic pressure of albumin across the wall of rat mesenteric microvessels, and the calculation of the albumin concentration gradients across the glycocalyx, at the breaks in the cleft and in the tissue, conform to the hypothesis that the hydrostatic and osmotic forces which determine fluid filtration across the microvessel wall are across the endothelial glycocalyx. Furthermore, the measurements of the albumin concentration on both sides of the microvessel wall during high and low filtration states demonstrate that the local albumin concentration behind the glycocalyx must differ greatly from that in the tissue. Figure 3.2 shows that the effective oncotic pressure difference is close to 70% of luminal oncotic pressure. These results support the growing evidence that tissue proteins contribute far less to the balance of osmotic forces across the microvessel wall than expected from the usual form of the Starling equation. The unique feature of

the experiment in Adamson et al. (2004) is to test the relation under conditions where the tissue concentration is high and directly measured. As pointed out in the introduction to this chapter, the diminished contribution of the tissue proteins was likely missed in earlier evaluations of the Starling balance for fluid exchange because the tissue concentrations were usually low due to experimental conditions.

Our experimental and theoretical results confirm and extend, for rat mesenteric microvessels, the observations described previously for frog mesenteric microvessels using a similar approach, that large protein osmotic pressures were developed across the microvessel wall even when albumin concentrations in the lumen and the tissue were equal (Hu et al., 2000). However, there are several important refinements in our experimental methods and the model used to explain the observations that we evaluate below. The most important is the measurement of the concentration of albumin in tissue close to the vessel wall under conditions where there is a high filtration rate of water across the vessel wall. There was no measurable difference in the concentration of albumin in the tissue within a few μm of the wall under conditions of high filtration rate compared with low filtration. This clearly demonstrates that a dilution of tissue albumin concentration does not contribute strongly to the formation of a protein osmotic pressure difference while albumin is in the tissue. These observations re-emphasize that the primary mechanism to maintain a low albumin concentration on the tissue side of the glycocalyx is the presence of small but infrequent gaps in the junctional strands that funnel the trans-capillary water flows, such that the velocity of water at the gaps is a significant fraction (estimated values 30-100%) of the albumin

diffusion velocity at the gaps. The result is that the diffusion of albumin from the tissue into the cleft beyond the strand gaps is reduced by convection, creating a steep gradient of albumin concentration in the distal region of the cleft in Figure 3.4. This helps to maintain the low albumin concentration in a "protected region" just underneath the glycocalyx. One notes that in regions removed from the breaks (y = 1795 nm), where convection is low, the concentration in the distal part of the cleft nearly equals that at the cleft exit due to diffusion of albumin in the tissue.

Another important improvement in the present experiments is that the ultrastructure of the endothelial cleft and continuity of junctional strands was determined by extensive serial sectioning on the same microvessels as used for the measurement of L_p. The gaps in the junctional strands were longer in rat than those in frog microvessels (315 nm versus 150 nm) described by Adamson & Michel (1993). The frequency of strand gaps observed in serial reconstructions was comparable (on average one every 3.6 μm in rat versus near 4.4 μm in frog) so it appears that the effective area for exchange of water between adjacent endothelial cells in the rat mesenteric microvessels at the level of the breaks in the junctional strand was larger than in the frog as the width of the openings (near 18 nm) was not a significantly different proportion of open strand (9% in rat compared with close to 4% in the frog). When this result is combined with the observation that the overall L_p of rat vessels is about one half that in frog, we conclude that, at any value of microvessel pressure, the water velocity at the level of the break is likely to be lower in the rat than in the frog. Thus the local Peclet number at the cleft (ratio of water velocity to albumin diffusion

velocity) is expected to be smaller in the rat microvessels. Thus, we expect more back diffusion of albumin from the tissue even at high microvessel pressures and a smaller albumin concentration difference across the glycocalyx at these pressures. These trends are consistent with the measured results. Although the measured albumin osmotic pressure approaches that of the luminal osmotic pressure even when albumin is in the tissue, the values in rat microvessels are close to 70 % of luminal pressure while the measured values in the frog approached 90% of the luminal concentration.

Table 3.1. *Cleft, junction strand gap, and glycocalyx parameters*

gap length[1]	$2d$	315 nm
gap spacing[1]	$2D$	3590 nm
depth of strand[1]	L_1	67 nm
total cleft depth[1]	L	411 nm
width of cleft[1]	$2h$	18 nm
cleft length per area vessel wall[1]	L_c	0.10 μm^{-1}
cleft linker spacing[2]	δ_c	15 nm
cleft linker diameter[3]	$2r_c$	2.5 nm
glycocalyx fiber spacing[4]	δ_f	8 nm
glycocalyx fiber diameter[4]	$2r_f$	12 nm

[1] Present results; [2] Schulze & Firth, 1992; [3] Shapiro et al., 1995; [4] Squire et al., 2001.

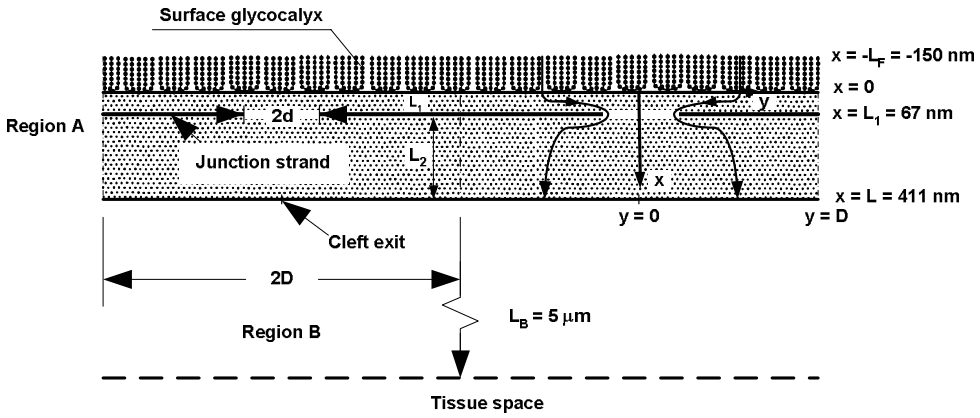

Figure 3.1 Idealized diagram representing the mathematical model for the endothelial glycocalyx. Values for the cleft and glycocalyx incorporating results of the present study and literature values are summarized in Table 3.1 taken from Adamson et al. (2004).

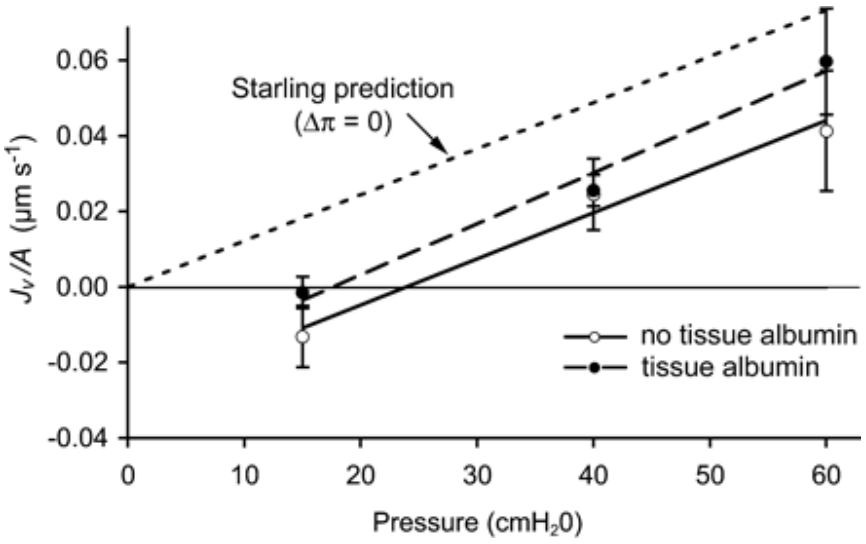

Figure 3.2. Effective oncotic pressure with and without high extravascular albumin. Filtration flux, J_v/A, during perfusion with BSA (50 mg/ml) was measured in this vessel first with protein-free Ringer superfusate (filled circles) and then with superfusate also containing BSA at the same concentration (open circles). Intercept on the pressure axis indicates the effective oncotic pressure and shows that when interstitial albumin is present at the same concentration as in the perfusate the effective oncotic pressure is greatly different from the expected value of zero (line of Starling prediction) (Adamson et al., 2004).

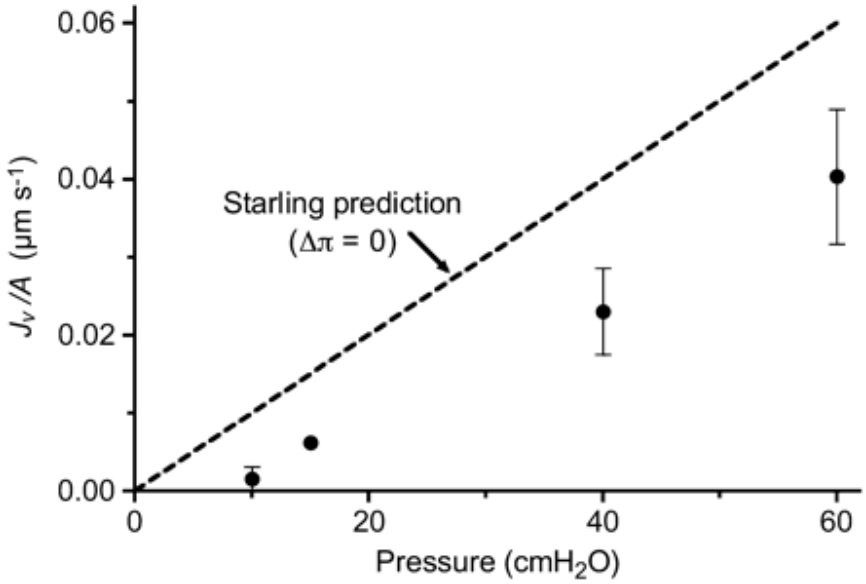

Figure 3.3. Steady state filtration at multiple pressures. Filtration flux, J_v/A, was measured after having established steady state conditions at each indicated intraluminal pressure. The superfusate contained BSA at the same concentration as the perfusate (50 mg/ml). Values shown are means ± SEM for 4 vessels. The relationship expected based on the lack of a protein osmotic difference between perfusate and interstitial fluid is also shown (Starling prediction) (Adamson et al., 2004).

Figure 3.4 Model prediction for the steady state albumin concentration gradient during low and high filtration. Dimensionless concentration profiles from the lumen into the tissue are shown for a path through the center of a strand gap (y = 0, solid line), the edge of a strand gap (y = *d* =158 nm, dashed line) and across the tight junction equidistant between two strand gaps (y = *D* = 1795 nm, dash-dot line). *LF* =150 nm. A. With *PL* =30 cmH2O protein concentration at the abluminal side of the glycocalyx is reduced by 45% from its value in the lumen and the superfusate. Concentration on the tissue side of the cleft is low near the strand gap and rises toward the tissue. *Inset*, concentration just outside the cleft is only 10% reduced from the steady state value in the lumen and the superfusate. B. At high pressure, with *PL* = 60 cmH2O, the protein concentration on the abluminal side of the glycocalyx is reduced by 75% from the luminal value. *Inset*, even at high *PL* the protein concentration just outside the cleft is reduced by only 15% from the value in the superfusate.

A

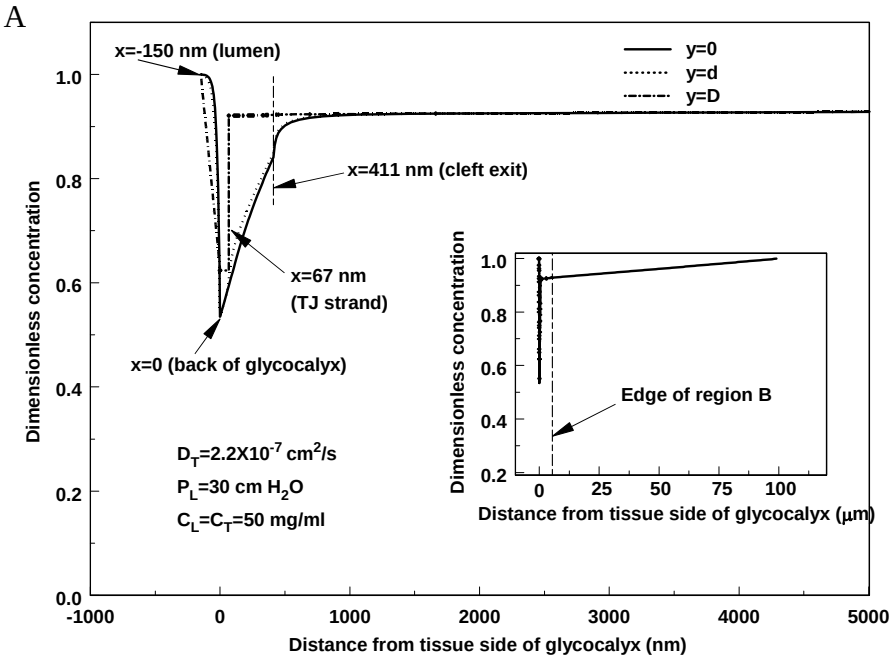
x=-150 nm (lumen)
y=0
y=d
y=D
x=411 nm (cleft exit)
x=67 nm
(TJ strand)
x=0 (back of glycocalyx)
D_T=2.2X10^{-7} cm^2/s
P_L=30 cm H_2O
C_L=C_T=50 mg/ml
Dimensionless concentration
Distance from tissue side of glycocalyx (nm)
Edge of region B
Distance from tissue side of glycocalyx (μm)

B

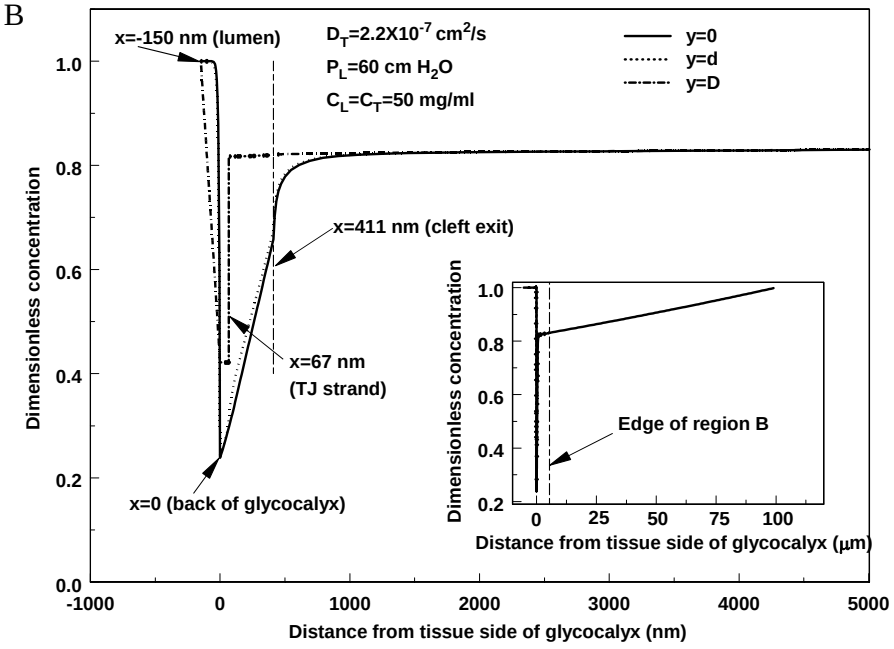
x=-150 nm (lumen)
D_T=2.2X10^{-7} cm^2/s
P_L=60 cm H_2O
C_L=C_T=50 mg/ml
y=0
y=d
y=D
x=411 nm (cleft exit)
x=67 nm
(TJ strand)
x=0 (back of glycocalyx)
Dimensionless concentration
Distance from tissue side of glycocalyx (nm)
Edge of region B
Distance from tissue side of glycocalyx (μm)

Chapter 4 A Simplified Model to Describe the Revised Starling Principle

4.1 INTRODUCTION

Starling's classical principle for the transcapillary water flow can be described by an equation of the form,

$$J_V / A = L_p \left[P_L - P_T - \sigma_f \left(\pi_L - \pi_T \right) \right], \tag{4.1}$$

where J_V / A is the fluid filtration flux across the capillary wall per unit area, L_p is the hydraulic permeability, σ_f is the reflection coefficient, and P_L, P_T, π_L and π_T are the global values for the hydrostatic and osmotic pressures in the capillary and interstitial compartments, respectively.

Michel (1997) and Weinbaum (1998) independently proposed that Starling's hypothesis should be applied locally, just across the thin endothelial glycocalyx layer (EGL), rather than globally, across the entire endothelial layer, between plasma and interstitium, since the EGL is proposed to be the primary molecular sieve for plasma proteins. The primary difficulty in applying the revised the Michel-Weinbaum model is that the local Starling forces behind the EGL, $P(0)$ and $\pi(0)$, are spatially varying and unknown because of the large gradients in velocity and protein concentration that are produced by the presence of the tight junction (TJ) strand in the cleft, see Figure 4.1A. Typically less than ten percent of the TJ strand is open with the result that the streamline pattern in the cleft departs greatly from one-dimensional flow. This creates a highly non-uniform pressure and concentration field throughout the cleft and an important non-

linearity in the hydraulic resistance since the presence of the glycocalyx has a substantial effect on the shape of the streamlines that pass though the discontinuities (orifices) in the TJ strand. This is clearly seen if one were to remove the EGL. The filtration coefficient L_p would rise sharply, not because the integrated average resistance of the glycocalyx is large, but because the EGL diverts the streamlines that would pass directly through the orifice and the resistance of these streamlines is greatly reduced when the EGL is removed. Thus, the EGL and the cleft can not be viewed as two simple linear resistances in series.

In view of the complexity of the detailed flow pattern, Hu and Weinbaum (1999) developed a sophisticated 3-D model with five separate regions to describe the flow geometry depicted in Figure 4.1A. This model predicted that the convective flow through the orifice-like breaks in the TJ strand could greatly reduce back diffusion from the tissue into the lumen side of the TJ strand with the result that the oncotic force behind the EGL could be much smaller than in the tissue at the cleft exit. This prediction is clearly borne out by the experiments in Hu et al. (2000) for frog microvessels and Adamson et al. (2004) for rat microvessels in which the tissue is backloaded with albumin at the same concentration as the lumen. The experiments demonstrate that at high filtration rates the proteins on the lumen side of the TJ strand are washed out and nearly the full oncotic pressure $\sigma_f \pi_L$ is felt across the EGL in the case of frog microvessels, and approximately 70 percent of $\sigma_f \pi_L$ in the case of rat microvessels, although the tissue oncotic pressure is isotonic with respect to the lumen oncotic pressure.

The 3-D model in Figure 4.1A is far too complicated for most investigators to conveniently use and requires considerable computer time for the numerical solutions to

converge. It is also hard to interpret the results and obtain numerical convergence when there are small concentration gradients in the tissue, since there is a 500 fold expansion in area from the cleft exit to the tissue. To overcome these shortcomings, we have formulated a much simpler model in which each of the five regions in Figure 4.1B is described by a 1-D, convection-diffusion equation which can be solved analytically subject to simplified interface matching conditions. Though the velocity and concentration fields are non-linearly coupled, the unknown constants that appear in the solutions for each region are linearly coupled in all but the Starling equation for the pressure and oncotic force across the EGL. This enables one to reduce the entire boundary value problem to a simple system of algebraic equations for the unknown constants that is easily solved on the computer. The key simplification is the conversion of the TJ strand with its periodic orifices to a single continuous slit which provides the same transport area for solutes as the orifice like breaks and whose hydraulic resistance is adjusted to provide the same L_p. This simplified model allows one to obtain solutions which closely mimic the full 3-D solutions for J_V / A and the net Starling forces across the EGL.

The new model has the additional advantage that one can easily assess the relative importance of the EGL and cleft and at the same time change the boundary conditions in the tissue. For example, Michel and Phillips (1987) treated the entire endothelium as a uniform matrix layer whose concentration on the tissue side was determined by the criterion that the entire solute flux passed though the paracellular pathway and the concentration in the tissue was given by the ratio of the total solute to water flux. The presence of the cleft with the TJ strand was neglected. The new model allows us to put

back the cleft with its TJ strand and still use a one-dimensional analysis. In addition, one can with little extra difficulty examine the effect of adding a transcellular vesicle flux in parallel with the paracellular pathway. The latter model is able to explain Levick's (1991) observation that the tissue oncotic pressure in the capillary beds of many tissues is approximately 40 percent of the lumen oncotic pressure. Finally, the model is able to easily explore the case where the tissue is back loaded by damaging the mesothelium and adding a superfusate of known concentration as in Hu et al. (2000) and Adamson et al. (2004). In this case one is able to examine the effect of small diffusion gradients in the tissue and their ability to penetrate upstream into the cleft.

4.2 MODEL DESCRIPTION

The 3-D theoretical model for rat mesentery capillaries shown in Figure 4.1A is the same as Adamson et al. (2004) except that the cross-bridging proteins in the cleft have been omitted for simplicity. These linker proteins could be cadherin molecules in the adherens junction (AJ) which Shulze and Firth (1992) observed just distal to the tight junction (TJ) strand. There could also be linker proteins in other parts of the cleft which do not have an ordered quasi-periodic appearance. One expects that neither the widely spaced cadherins (15 nm spacing) in the AJ nor the non-ordered linker proteins provide significant extra resistance to water or protein transport in the cleft.

Figure 4.1B is the simplified 1-D model constructed from Figure 4.1A. The model contains five regions. The first region, region F, is an EGL whose thickness is L_F and the structure is the same as in the 3-D model in Figure 4.1A. The EGL covers the entire endothelial surface including the entrance to the intercellular cleft. The second region,

region A, is a cleft entrance region on the lumen side of the TJ strand whose depth is L_1. The third region, region TJ, is a continuous narrow slit of height $2b$ which replaces the TJ strand with discontinuities of width $2d$ in Figure 4.1A. $2b$ is chosen to be $2h \cdot d/D$. This allows the pore area for albumin diffusion to be conserved and the average velocity of the water in the narrow continuous slits to be the same as in the orifice breaks in the 3-D model when L_p is the same in both models. In contrast to the TJ strand in the 3-D model, which is treated as a zero-thickness layer, the TJ in Figure 4.1B has a finite depth, L_{TJ}, so that it will provide a finite hydraulic resistance in the 1-D model. L_{TJ} is determined by requiring that the total hydraulic resistance of the cleft be the same as predicted by the 3-D model. The fourth region, region B, is the cleft on the tissue side of the TJ strand whose depth is (L-L_1-L_{TJ}). The fifth region, region T, is the tissue space of depth L_T and width $2H$. In the 3-D model, the tissue space is divided into two subregions, a near field and a far field. The near field is a region within 5 μm of the cleft exit where the exit jets from the individual junction orifices and adjacent clefts merge with each other and form a uniform flux along the length of the cleft exit. The description of the far field depends on the tissue loading conditions described in the next paragraph. In the 1-D model, we have a continuous narrow slit for the TJ strand and, thus, one does not have to deal with the complication introduced by the mixing of discrete exit jets. There is an expansion of the flow from a height $2h$ to the cleft spacing $2H$, but since $L_T >> 2H$, this mixing can be neglected.

To simplify the model the short mixing regions at the interfaces between each region are neglected in the 1-D model. Thus, each region can be approximated by a 1-D convection-diffusion equation. At each interface, we assume that the albumin

concentration and albumin flux per unit cleft length are continuous. Three different tissue loading conditions are analyzed. The first is a modified Michel and Phillips (1987) model in which the tissue concentration is uniform and given by the ratio of the total solute flux to the total water flux. The second is the backloading model in Adamson et al. (2004) in which the mesothelium is damaged around 100 μm from the vessel wall and the tissue concentration set equal to the superfusate concentration at this location. In both cases, the total water and solute fluxes pass through the paracellular pathway. The third loading condition is the model proposed in Renkin (1992) and Michel (1997) in which a transcellular vesicle flux is added in parallel with the paracellular pathway to explain the observation that the tissue oncotic pressure in the capillary beds of many tissues is approximately 40 percent of the lumen oncotic pressure (Levick, 1991).

4.3 METHODS

4.3.1 3-D model

To convert from a 3-D to a 1-D model, we first have to examine in more detail the effective hydraulic resistance that results from placing a uniform resistance barrier, the EGL, in front of a highly non-uniform cleft with discrete orifice like breaks in its TJ strand. The key insights can be obtained by analyzing the pressure field for the filtration flow in the 3-D model shown in Figure 4.1A. The structural parameters for the cleft are taken from Adamson et al. (2004) and are summarized in Table 1. The only unknown in the 3-D model, if the EGL thickness, L_F, is prescribed, is K_P, the Darcy permeability for the EGL. K_P is then determined by satisfying the measured value of L_p=1.3x10^{-7} cm/s/cm

H_2O for rat mesenteric capillaries (Adamson et al., 2004). Using the structural parameters for the cleft in Table 1 and L_F=150 nm, one finds that K_P =9.24 nm^2.

The detailed pressure profiles for the 3-D model are shown in Figure 4.2A. These profiles scale linearly with P_L. One observes that for L_F=150 nm, approximately half of the pressure drop occurs across the EGL in the region above the orifice, see Figure 4.2A. However, the average pressure drop across the entire EGL is only 10 percent of the total pressure drop across the entire endothelial layer, see Figure 4.2B. If one naively applies the average pressure behind the EGL as the entrance condition for the cleft as shown in Figure 4.2B, one obtains a much larger water flux than in Figure 4.2A because the fluid streamline patterns in the cleft for the pressure entrance condictions in Figs. 2A and 2B are dramatically different. Figure 4.3 shows that the removal of the 150-nm EGL will lead to a near doubling in L_p. This doubling indicates that approximately half of the total pressure drop should occur across the EGL in the region above the orifice. The pressure profiles in Figure 4.2A show that this is indeed the case and that the presence of the EGL has doubled the hydraulic resistance on these central streamlines which provide most of the flow.

The contribution of the EGL to the total resistance has two components. The first component is the intrinsic resistance of the water flowing through the matrix. This is equivalent to the resistance of the matrix in a 1-D flow. The second component is due to the ability of the EGL to change the streamline pattern in the cleft and, thus, the resistance of the flow after it has passed through the matrix layer. The effect of the streamline pattern change at the cleft entrance on the flow in the EGL itself is minor. The streamlines passing through the EGL are nearly straight because the length of the

periodic unit, $2D$=3590 nm, is >> than the thickness of the layer, L_F=150 nm. Thus, the pressure gradient in the *y* direction is << than in the *x* direction in the EGL. However, once the flow has passed through the EGL the pressure distribution at the cleft entrance markedly changes the shape of the streamlines as they converge on the orifice. Therefore, when converting the 3-D model to a 1-D model, one has to add a resistance, R, at the back of the EGL to take account of the change in streamline pattern that results from adding an EGL of specified thickness or resistance in front of the cleft entrance. This is achieved by defining a corrected pressure, $P(0)_{corrected}$, to account for the streamline pattern change in the cleft due to the presence of the EGL. The flow across the EGL is given by

$$u_F = \frac{K_P}{\mu L_F}\left(P_L - P(0)\right) = R\left(P(0) - P(0)_{corrected}\right), \tag{4.2}$$

where u_F is the average velocity in the EGL, $P(0)$ is the average pressure behind the EGL, shown in Figure 4.2B, and R is the extra resistance that is required to describe the change in the streamline pattern due to the presence of the EGL. The results in Figs. 2 and 3 show that for L_F=150 nm

$$P(0)_{corrected} \approx \frac{P_L}{2}. \tag{4.3}$$

For L_p=1.3x10^{-7} cm/s/cm H_2O, one finds that R=1735 nm/s/cm H_2O for a 150-nm thick EGL whose K_P is the same as in the 3-D model. R for other EGL thicknesses can be estimated from Figure 4.3 by using the increase in L_p that occurs when the EGL is removed.

4.3.2 1-D model

4.3.2.1 Water velocity

In the 1-D model, continuity of water flux at the interface between each region requires that

$$h \cdot u_F = h \cdot u_A , \tag{4.4}$$

$$h \cdot u_A = b \cdot u_{TJ} , \tag{4.5}$$

$$b \cdot u_{TJ} = h \cdot u_B , \tag{4.6}$$

$$h \cdot u_B = H \cdot u_T , \tag{4.7}$$

where u_i (i=F, A, TJ, B, and T) are the 1-D average velocities.

Therefore,

$$u_F = u_A = u_B = b/h \cdot u_{TJ} = H/h \cdot u_T . \tag{4.8}$$

4.3.2.2. Depth of tight junction

The ultrastructural measurements in Adamson et al. (2004) show that approximately 9 % of the tight junction strand is open ($2d$=315 nm vs. $2D$=3590 nm). To satisfy the condition $2b = 2h \cdot d/D$, which preserves the TJ transport area, we find that the slit height $2b$ is 1.58 nm, or approximately 9 % of the cleft height, $2h$=18 nm.

The average velocity for a parabolic laminar flow in a channel of depth L_{TJ} and height $2b$ is,

$$u_{TJ} = \frac{(P_{TJ1} - P_{TJ2})b^2}{3\mu L_{TJ}} , \tag{4.9}$$

where P_{TJ1} and P_{TJ2} are the pressures at the entrance and exit of the TJ slit.

Likewise, in regions A and B

$$u_A = \frac{(P(0)_{corrected} - P_{TJ1})h^2}{3\mu L_1} , \tag{4.10}$$

$$u_B = \frac{(P_{TJ2} - P_t)h^2}{3\mu(L - L_1 - L_{TJ})}, \tag{4.11}$$

where P_T is the pressure in the tissue. We assume that P_T=0.

For pure filtration without albumin in the lumen or in the tissue, one has

$$J_V / A = L_p(P_L - P_t). \tag{4.12}$$

$$J_V / A = u_A \cdot L_C \cdot 2h \cdot 10^{-7}, \tag{4.13}$$

where L_C=1000 cm of cleft per cm^2 vessel wall (Adamson et al. 2004).

Solving Equations (4.3), (4.8) - (4.13) when L_p=1.3x10^{-7} cm/s/cm H_2O, one finds that L_{TJ}=1.49 nm.

One notes that a small channel of height 2b=1.58 nm and depth L_{TJ}=1.49 nm which satisfies the measured L_p=1.3x10^{-7} cm/s/cm H_2O in rat mesentery will not allow the passage of albumin, diameter 7 nm. However, in reality the pore in the tight junction strand is 18 nm high and 315 nm wide, and our narrow continuous TJ slit is an artificial construct which preserves the TJ area for albumin diffusion. The full cleft height 2h is used to estimate the reflection coefficient in the TJ strand and cleft regions A and B in the next section.

4.3.2.3. One-dimensional convection-diffusion

The governing equation for 1-D convection and diffusion in the EGL or any cleft region is given by

$$-D_i \frac{d^2 C_i}{dx^2} + (1 - \sigma_{f,i}) u_i \frac{dC_i}{dx} = 0, \tag{4.14}$$

where i=F, A, TJ or B. Solving Equation (4.14) one finds

$$C_i(x) = C_{i1} + C_{i2} \cdot exp\left(\frac{(1 - \sigma_{f,i}) u_i \cdot x}{D_i}\right), \tag{4.15}$$

where C_{i1} and C_{i2} are not the concentrations at particular positions but unknown constants which can be determined by applying the boundary and matching conditions in all the regions.

Therefore, the solute flux across any region *i* per unit cleft length is

$$\begin{aligned}(J_S)_i(x) &= A_i \cdot \left(-D_i \frac{dC_i}{dx} + (1-\sigma_{f,i}) u_i \cdot C_i \right) \\ &= A_i \left(-D_i \frac{(1-\sigma_{f,i}) u_i C_{i2}}{D_i} exp\left(\frac{(1-\sigma_{f,i}) u_i \cdot x}{D_i} \right) + (1-\sigma_{f,i}) u_i \left(C_{i1} + C_{i2} \cdot exp\left(\frac{(1-\sigma_{f,i}) u_i x}{D_i} \right) \right) \right) \\ &= A_i \cdot (1-\sigma_{f,i}) u_i \cdot C_{i1}, \end{aligned} \tag{4.16}$$

where A_i is the cross-section area of each region and can be replaced by just the height of each region. The reflection coefficient for albumin in the EGL, $\sigma_{f,F}$, is expressed as σ_f. A typical value is 0.94. To estimate the reflection coefficients for albumin in the cleft, σ_C, we use the approximate formula for steric exclusion of a solute of radius a in a channel of half height h

$$\sigma_C = 1 - \left(\frac{J_S}{J_V C_1} \right)_{\Delta C=0} = 1 - \frac{\int_0^{h-a} v(x)dx}{\int_0^{h} v(x)dx}, \tag{4.17}$$

where $v(x)$ is the local velocity in a parabolic profile. The upper limit of integration (*h*-*a*) for the solute flux arises from the steric exclusion due to the finite solute size. After evaluating the integrals in Equation (4.17), one finds that

$$\sigma_C = 1 - \frac{3}{2}\left(1 - \frac{a}{h}\right) + \frac{1}{2}\left(1 - \frac{a}{h}\right)^3 = 1 - \frac{3\phi}{2} + \frac{\phi^3}{2}, \tag{4.18}$$

where ϕ is the partition coefficient indicating the ratio between the area available to solute and that available to water. Using Equation (4.18) one finds that for albumin, a=3.5 nm, and h=9 nm, σ_C is 0.197.

In summary, in the EGL

$$C_F(x) = C_{F1} + C_{F2} \cdot exp\left(\frac{(1-\sigma_f)u_F \cdot x}{D_F} \right), \tag{4.19}$$

$$(J_S)_F(x) = 2h(1-\sigma_f)u_F \cdot C_{F1}, \tag{4.20}$$

in region A

$$C_A(x) = C_{A1} + C_{A2} \cdot exp\left(\frac{(1-\sigma_C)u_A \cdot x}{D_C} \right), \tag{4.21}$$

$$(J_S)_A(x) = 2h(1-\sigma_C)u_A \cdot C_{A1}, \tag{4.22}$$

in region TJ

$$C_{TJ}(x) = C_{TJ1} + C_{TJ2} \cdot exp\left(\frac{(1-\sigma_C)u_{TJ} \cdot x}{D_C} \right), \tag{4.23}$$

$$(J_S)_{TJ}(x) = 2b(1-\sigma_C)u_{TJ} \cdot C_{TJ1}, \tag{4.24}$$

and in region B

$$C_B(x) = C_{B1} + C_{B2} \cdot exp\left(\frac{(1-\sigma_C)u_B \cdot x}{D_C} \right), \tag{4.25}$$

$$(J_S)_B(x) = 2h(1-\sigma_C)u_B \cdot C_{B1}. \tag{4.26}$$

The governing equation in the tissue is

$$-D_T \frac{d^2 C_T}{dx^2} + u_T \frac{dC_T}{dx} = 0. \tag{4.27}$$

Solving Equation (4.27), one finds

$$C_T(x) = C_{T1} + C_{T2} \cdot exp\left(\frac{u_T \cdot x}{D_T}\right), \tag{4.28}$$

where C_{T1} and C_{T2} are unknown constants which can be determined by the boundary and matching conditions. The Solute flux leaving the cleft is

$$(J_S)_T(x) = 2H \cdot u_T \cdot C_{T1}. \tag{4.29}$$

4.3.2. 4. Boundary and matching conditions

4.3.2. 4. 1 Modified Michel and Phillips (1987) model

At the entrance of the EGL the albumin concentration is the same as the lumen concentration. Therefore,

$$C_F(-L_F) = C_L, \tag{4.30}$$

$$\overset{(4.8),(4.19)}{\Rightarrow} \quad C_{F1} + C_{F2} \cdot exp\left(\frac{(1-\sigma_f)u_F \cdot (-L_F)}{D_F}\right) = C_L. \tag{4.31a}$$

At the interfaces between each region, the solute flux per unit cleft length is continuous. Therefore,

$$(1-\sigma_f)C_{F1} = (1-\sigma_C)C_{A1}. \tag{4.31b}$$

$$C_{A1} = C_{TJ1}. \tag{4.31c}$$

$$C_{TJ1} = C_{B1}. \tag{4.31d}$$

At the interfaces between each region, the concentration is continuous. Therefore,

$$C_{F1} + C_{F2} = C_{A1} + C_{A2}. \tag{4.31e}$$

$$C_{A2} \cdot exp\left(\frac{(1-\sigma_C)u_A \cdot L_1}{D_C}\right) = C_{TJ2} \cdot exp\left(\frac{(1-\sigma_C)hu_A \cdot L_1}{bD_C}\right). \tag{4.31f}$$

$$C_{TJ2} \cdot exp\left(\frac{(1-\sigma_C)hu_A(L_1 + L_{TJ})}{bD_C}\right) = C_{B2} \cdot exp\left(\frac{(1-\sigma_C)u_A(L_1 + L_{TJ})}{D_C}\right). \tag{4.31g}$$

At the cleft exit the concentration is the ratio of the albumin to water flux. Therefore,

$$C_B(L) = \frac{J_S}{J_V}, \tag{4.32}$$

$$\overset{(4.22),(4.25)}{\Rightarrow} \quad C_{B1} + C_{B2} \cdot exp\left(\frac{(1-\sigma_C)u_B \cdot L}{D_C}\right) = \frac{2h(1-\sigma_C)u_A \cdot C_{A1}}{2h \cdot u_A} = (1-\sigma_C)C_{A1},$$

$$\overset{(4.31c),(4.31d)}{\Rightarrow} \quad C_{B2} \cdot exp\left(\frac{(1-\sigma_C)u_B \cdot L}{D_C}\right) = \sigma_C \cdot C_{A1}. \tag{4.33}$$

There are eight unknown constants, C_{i1} and C_{i2} (i=F, A, TJ and B), and four unknown water velocities, u_i (i=F, A, TJ and B). The four water velocities can be related to each other by Equation (4.8) and therefore expressed in terms of only one unknown velocity, which we choose to be u_A. Thus, there are nine unknowns. However, there are only eight equations, Equations (4.31a)-(4.31g), and (4.33). For the ninth equation we apply the Starling principle across the EGL

$$u_A = \frac{K_P}{\mu L_F}\left[P_L - P(0) - \sigma_f(\pi_L - \pi(0))\right]. \tag{4.34}$$

The oncotic force behind the glycocalyx, $\pi(0)$ (cm H_2O), is related to the albumin concentration $C_A(0)$ (mg/ml) by the non-linear empirical relation in Equation (4.4) of McDonald and Levick (1993). One notes that Equation (4.4) of McDonald and Levick (1993) is for 35°C (rabbit knee experiments). This can be corrected to 37°C for our rat experiments using the Van't Hoff equation. $C_A(0)$, in turn, can be expressed as a function of C_{A1}, C_{A2}, and u_A.

The water flow in regions A, TJ, and B can be approximated by Poiseuille channel flow, whose velocities are described by Equations (4.10), (4.9) and (4.11), respectively. Solving Equations (4.8) -(4.11), one obtains

$$P(0)_{corrected} = 3\mu \cdot u_A \cdot \left(\frac{L - L_{TJ}}{h^2} + \frac{h \cdot L_{TJ}}{b^3} \right). \tag{4.35}$$

One can relate $P(0)$ and $P(0)_{corrected}$ using Equation (4.2). Therefore, there are two new unknowns, $P(0)$ and $P(0)_{corrected}$, but three more equations, Equations (4.2), (4.34) and (35). In total, there are eleven unknowns, C_{i1} and C_{i2} (i=F, A, TJ and B), one water velocity, u_A, and two pressures, $P(0)$ and $P(0)_{corrected}$; there are eleven equations, Equations (4.2), (4.31a) to (4.31g), and (4.33)-(4.35). Solving all these eleven equations simultaneously, one obtains all the unknowns.

4.3.2. 4. 2. Adamson et al. (2004), tissue backloading

In our model for tissue backloading described in Adamson et al. (2004) model, the boundary and matching conditions in the lumen and in the cleft described by Equations (4.31a) to (4.31g) still apply. However, the tissue is backloaded 100 μm from the vessel wall, where we assume the tissue concentration is the same as in the superfusate. At the cleft exit the albumin flux and concentration are continuous. Thus,

$$(1 - \sigma_C) C_{B1} = C_{T1}. \tag{4.36a}$$

$$C_{B1} + C_{B2} \cdot exp\left(\frac{(1 - \sigma_C) u_A \cdot L}{D_C} \right) = C_{T1} + C_{T2} \cdot exp\left(\frac{h u_A \cdot L}{H D_T} \right). \tag{4.36b}$$

At the damage site the albumin concentration is prescribed and equal to that in the superfusate C_i,

$$C_T (L + L_T) = C_i, \tag{4.37}$$

$$\overset{(4.8),(4.28)}{\Rightarrow} \quad C_{T1} + C_{T2} \cdot exp\left(\frac{hu_A \cdot (L + L_T)}{HD_T} \right) = C_i . \tag{4.36c}$$

The matching conditions for the water flux at the cleft entrance and in the cleft, Equations (4.2), (4.34) and (4.35) still apply. Therefore, there are thirteen unknowns, C_{i1}, C_{i2}, (i=F, A, TJ, B and T), u_A , $P(0)$ and $P(0)_{corrected}$; there are thirteen equations, Equations (4.2), (4.31a)-(4.31g), (4.34), (4.35) and (4.36a)-(4.36c). Solving these thirteen equations simultaneously, one determines all the unknowns.

4.3.2. 4. 3. Combined paracellular and vesicular transport

In the case of combined paracellular and transcellular vesicular transport the boundary and matching conditions in the lumen, at the cleft entrance, at the tight junction entrance and exit, described by Equations (4.2), (4.31a)-(4.31g), (4.34), (4.35) and (4.36b) are still valid. At the cleft exit, the concentration is continuous, but the flux is not, since there is a source for albumin due to the transcellular pathway. Therefore, at the cleft exit

$$(J_S)_B(L) + 2H \cdot K \cdot (C_L - C_T(L)) = (J_S)_T(L), \tag{4.38a}$$

$$\overset{(26),(29)}{\Rightarrow}$$

$$2h(1-\sigma_{f,C})u_B \cdot C_{B1} + 2H \cdot K \cdot \left(C_L - \left(C_{T1} + C_{T2} \cdot exp\left(\frac{u_T \cdot L}{D_T} \right) \right) \right) = 2H \cdot u_T \cdot C_{T1}, \tag{4.39a}$$

where the vesicular flux is described by the second term in Equation (4.38a). In this term K is a coefficient, which depends on the vesicular volume that passes from the plasma to the interstitium per unit time and the partition of solute molecules in the vesicular plasma. If we require that P_L=25 cm H_2O, the average pressure in a capillary bed whose arterial

pressure is about 35 cm H_2O and venous pressure about 15 cm H_2O, one finds that C_T will have an average value in the tissue that is approximately $0.4C_L$ when K= 5.057 nm/s.

In general, the tissue concentration is given by

$$C_T(x) = \frac{J_S}{J_V}, \tag{4.38b}$$

$$\overset{(4.28),(4.39a)}{\Rightarrow} \quad C_{T1} + C_{T2} \cdot exp\left(\frac{u_T \cdot x}{D_T}\right)$$

$$= \frac{2h(1-\sigma_C)u_B \cdot C_{B1} + 2H \cdot K \cdot \left(C_L - \left(C_{T1} + C_{T2} \cdot exp\left(\frac{u_T \cdot L}{D_T}\right)\right)\right)}{2h \cdot u_B}$$

$$= (1-\sigma_C)C_{B1} + \frac{H \cdot K \cdot \left(C_L - \left(C_{T1} + C_{T2} \cdot exp\left(\frac{u_T \cdot L}{D_T}\right)\right)\right)}{h \cdot u_B}. \tag{4.39b}$$

There are thirteen unknowns, C_{i1}, C_{i2}, (i=F, A, TJ, B and T), u_A, $P(0)$ and $P(0)_{corrected}$; there are thirteen equations, Equations (4.2), (4.31a)-(4.31g), (4.34), (4.35), (4.36b), and (4.39a)-(4.39b) to determine all the unknowns.

4.4 RESULTS

4.4.1 3-D model predictions for L_p and pressure in the cleft for pure filtration

Figure 4.2A shows the pressure profiles at the cleft entrance (x=0), before and after the TJ strand ($x = L_1 \mp$) when there is a 150-nm EGL. The structural parameters describing the cleft and TJ strand are summarized in Table 1. L_p=1.3x10^{-7} cm/s/cm H_2O. The pressure behind the EGL is spatially non-uniform. At the centerline, about half of the pressure drop occurs across the EGL and half occurs in the cleft, while at the locations

towards the edges of the periodic unit, the pressure drop across the EGL vanishes and nearly the entire pressure drop occurs across the TJ strand. The pressure drop across the EGL averaged over the entire cleft is only 10 percent of the total pressure drop across the endothelial layer. As shown in Figure 4.2B, if the EGL is removed and the average pressure at the cleft entrance is applied, one finds that the pressure distribution in the cleft is dramatically altered and the water flux is almost doubled (0.019 μm/s vs. 0.034 μm/s for P_L=15 cm H_2O).

Figure 4.3 shows the 3-D model prediction for L_p as a function of EGL thickness based upon the cleft structural parameters in Table 1. Although the average pressure behind the 150-nm EGL is only 10 percent of the total pressure drop across the endothelial layer, the removal of the EGL results in a doubling of L_p, which indicates that about half of the hydraulic resistance resides in the EGL.

4.4.2 Comparison between the predictions of 1-D and 3-D models for net pressures opposing filtration behind the EGL

Rearranging Equation (4.34), one obtains

$$u_A = \frac{K_P}{\mu L_F}\left[\left(P_L - \sigma_f \pi_L\right) - \left(P(0) - \sigma_f \pi(0)\right)\right]. \tag{4.40}$$

For the 3-D model one has a similar relation except that $P(0)$ and $\pi(0)$ are functions of y and the average values should be applied. One notes that $\left(P(0) - \sigma_f \pi(0)\right)$ is the hydrostatic plus oncotic pressure behind the EGL opposing filtration, while $\left(P_L - \sigma_f \pi_L\right)$ is the equivalent pressure in the lumen favoring filtration.

Figure 4.4 compares between the predictions of the 1-D and 3-D models for the net pressure behind the EGL opposing filtration for the tissue backloading experiment in

Adamson et al (2004). One observes that they are in very close agreement with each other in spite of the major simplifications introduced in the 1-D model.

4.4.3 1-D model prediction of water flux

Figure 4.5 compares between the experimental measurements for J_V/A for tissue backloading (Adamson et al. 2004) as a function of lumen pressure, P_L, with our 1-D model predictions of the modified Michel and Phillips (1987) model, our backloading model, and our combined paracellular-vesicular transport model where $C_T = 0.4C_L$ at P_L = 25 cm H_2O (Renkin, 1992; Michel, 1997). The measured L_p=1.3x10^{-7} cm/s/cm H_2O is satisfied for all these models. The modified Michel and Phillips (1987) model, where all water and solutes pass through a paracellular pathway, predicts that the J_V/A curve will bend sharply near $\sigma_f \pi_L$ and that there is no steady state reabsorption even at very low lumen pressure, as observed in their steady state measurements. When a vesicular pathway is present in addition to the paracellular pathway and $C_T = 0.4C_L$, our model predicts that the J_V/A curve also bends, but not as sharply as the modified Michel and Phillips model. The J_V/A curves for both models go through the origin. The theoretical curve for the experimental condition where the tissue is isotonically backloaded (solid line) is in reasonable agreement with the experimental measurements (solid dots). This solid curve will also go through the origin when $P_L = 0$. On the other hand, when the tissue is backloaded at 20 mg/ml 100 μm from the vessel wall, one notes that there is steady state reabsorption when P_L is around 18 cm H_2O or lower. Our detailed concentration profiles presented in the next section show that this behavior will occur if

back diffusion from the damage site overwhelms the washout of solute from region A behind the EGL.

4.4.4 Concentration profiles predicted by the modified Michel and Phillips (1987) model

Figure 4.6 shows the theoretical predictions for the concentration profiles for the modified Michel and Phillips (1987) model. The convective and diffusive fluxes at several key interfaces in the cleft are summarized in Table 3. For all the lumen pressure conditions, there is always a very small concentration gradient in the cleft, approximately 0.5 percent of the concentration gradient across the EGL or less. At high lumen pressures, P_L = 40 or 60 cm H_2O, the concentration at the back of the EGL (or at the cleft entrance) as well as in the cleft has reached the convection limit, $(1-\sigma_f)C_L$, and is no longer sensitive to the lumen pressure. This behavior closely corresponds to the original Michel and Phillips model where the cleft is omitted.

4.4.5 Concentration profiles predicted for the tissue backloading model

Figure 4.7 shows the theoretical predictions for the concentration profiles for our 1-D tissue backloading model in which the tissue is backloaded at 50 mg/ml (A) and at 20 mg/ml (B). The convective and diffusive fluxes at several key interfaces in the cleft are summarized in Tables 4A and 4B. As observed in the backloading experiments of Adamson et al. (2004), where C_L =50 mg/ml and the superfusate is maintained at the same concentration, our 1-D model predicts that the albumin concentration 5 μm from the vessel wall is relatively insensitive to the filtration rate (or the lumen pressure). Our model predicts that at P_L =60 cm H_2O, the albumin concentration at 5 μm is about 0.8C_i. However, the convective flux of solute through the TJ slit exceeds the backward diffusive

flux with the result that the concentration behind the EGL is only approximately 0.45 C_i. When the superfusate concentration at the damage site is reduced to 20 mg/ml, one observes in Figure 4.7B a crossover in behavior at P_L about 18 cm H_2O. For P_L > 18 cm H_2O there is filtration across the EGL, whereas for P_L < 18 cm H_2O there is reabsorption. At the low lumen pressure, the concentration at the back of the EGL does not rise high enough to arrest the reabsorption. One notices that the concentration gradient in the tissue is small and that the relative magnitudes of the diffusive and convective fluxes of albumin in the tissue are comparable at both low and high lumen pressures in Tables 4A and 4B.

4.4.6 Concentration profiles with vesicular transport

Figure 4.8 shows the theoretical predictions of our 1-D model for the concentration profiles when both paracellular and vesicular transport are considered. The convective and diffusive fluxes at several key interfaces in the cleft are summarized in Table 5. The magnitude of the vesicular flux is determined by requiring that at P_L =25 cm H_2O, a typical average capillary pressure, the tissue concentration, C_T, is 20 mg/ml, or 40 percent of the lumen concentration as estimated in Levick (1991) for a number of tissues. Equation (4.38b) requires that the solute in the tissue is well mixed and, therefore, there is no diffusion flux in the tissue in Table 5.

4.5 DISCUSSION

There is a growing body of evidence in support of the Michel-Weinbaum model for a revised Starling principle in which the Starling forces are applied across just the EGL rather than across the entire endothelial layer (Levick, 1991; Levick and McDonald, 1993;

Michel, 1997; Weinbaum, 1998; Adamson et al., 2004). However, one would like to apply this revised Starling principle without having to resort to the complicated 3-D model in Hu and Weinbaum (1999), Hu et al., (2000) and Adamson et al. (2004) which uses detailed cellular-level microstructural data for each TJ and EGL geometry. The primary objective of this chapter is to develop a simplified 1-D model to describe this revised Starling principle that is more accessible to experimentalists and can be readily applied to analyze cleft and junction structure and different tissue loading conditions.

To make the conversion from the complex 3-D to the 1-D model, one has to capture several key features. First, the EGL must serve as the primary molecular sieve across which the effective oncotic pressure is felt. This is satisfied by applying the Starling principle across just the EGL as opposed to the entire endothelial layer. Second, the model must capture the ability of the EGL to change the fluid streamline patterns in the cleft. This is described by adding an extra hydraulic resistance, R, whose value is determined by requiring that fluid flux across the EGL in the 3-D model be the same as in the 1-D model. Third, the average velocity at the continuous TJ slit be the same as in the 3-D model. This is satisfied by requiring the height of the narrow slit in the TJ, $2b$, be $2h \cdot d/D$. This also ensures that the TJ area for albumin diffusion is preserved. Fourth, we require that the fractional resistance of the cleft in the 1-D model be the same as in the 3-D model. One can estimate the fractional resistance of the cleft from Figure 4.3 by comparing the change in L_p with and without the EGL, and then determine the TJ depth, L_{TJ}. These features allow the 1-D model to provide results that are in very close agreement with those predicted by its much more complex numerical 3-D counterpart, as shown in Figure 4.4. We do not compare the 1-D model predictions for $P(0)$ and $\pi(0)$

with the 3-D model predictions individually, because neither of them is measurable. On the other hand, the combined pressure opposing filtration behind the EGL, $\left(P(0)-\sigma_f \pi(0)\right)$, can be evaluated in terms of J_V/A curves because the difference between the solid line, the hydrostatic plus oncotic pressure in the lumen favoring filtration, and the dashed line, the equivalent pressure behind the EGL opposing filtration, is the net force for J_V/A, see Figure 4.4.

One might expect that the EGL and the cleft are two linear resistances in series, and therefore, the resistance of the cleft is fixed and determined only by its own geometry independent of the presence of the EGL. If this assumption were true, one could simply average the pressure behind the EGL and apply this average pressure as the entrance condition to the cleft. However, one finds that the water flux increases by about 80 percent from Figure 4.2A to Figure 4.2B. The streamlines through the EGL itself are nearly straight because the length of the periodic unit is >> than the thickness of the layer (3590 nm vs. 150 nm), and, thus, the pressure gradients in the *y* direction are << than in the *x* direction, see Figure 4.2A. Therefore, one is still able to define a simple average $P(0)$ and $\pi(0)$ behind the EGL, see Figure 4.4, and use these pressures to calculate the total flow across just this layer. At the same time, the solution to the boundary value problem for the pressure distribution within the cleft depends strongly on the pressure entrance condition since this determines the shape of the streamlines on the lumen side of the TJ strand. A streamline near the orifice centerline sees little resistance in the cleft since it is not obstructed. The EGL in front of the orifice will provide a large part of the total resistance. For a 150-nm EGL nearly 50 percent of the total pressure drop occurs across the EGL on the central streamlines for pure filtration in rat mesentery capillaries.

Moreover, adding a significant resistance in front of the orifice causes these central streamlines to be diverted to the sides of the orifice. In contrast, streamlines off to the sides of the orifice see a much greater resistance in the cleft, and, thus, the pressure drop across the EGL is a much smaller fraction of the total pressure drop for these off-center streamlines. When the EGL is removed, nearly all the water goes directly through the orifice without being shunted to the side and passing through the 67-nm narrow channel between the back of the EGL and the TJ strand. It is this streamline shift that is the origin of the non-linearity. One can increase L_p two fold by removing the 150-nm EGL, although the average pressure drop across the EGL is only approximately 10 percent of the total pressure drop across the entire EGL, see Figure 4.3. In the 1-D model, one has to add a resistance R to account for the effect of the change in the streamline patterns at the cleft entrance due to the presence of the EGL. R can be estimated from Figure 4.3 by looking at the change in L_p that occurs when the EGL is removed.

Michel and Phillips (1987) treat the entire endothelium as a uniform matrix layer whose concentration on the tissue side is determined by the criterion that the entire water and solute fluxes pass though a paracellular pathway and that the solute in the tissue is well mixed. For these conditions the tissue concentration is given by the ratio of the total solute to water flux. The presence of the cleft with the TJ strand is neglected. The new model allows us to put back the cleft with its TJ strand and still use a 1-D analysis. One finds that the theoretical predictions of the new 1-D model for the J_V / A vs. lumen pressure curve have the same behavior as the measurements in Michel and Phillips (1987). Moreover, as predicted in their paper, the concentration gradient in the cleft is

very small, see Figure 4.6. in the diffusive resistance of the cleft is small compared to the EGL.

Tissue protein concentrations vary between 0.3 and 0.6 of the lumen concentration with 0.4 being the most representative value (Levick, 1991). One can with little extra difficulty examine the effect of adding a transcellular vesicle flux in parallel with the paracellular pathway as proposed in Renkin (1992) and Michel (1997). The coefficient *K*, which describes the vesicular transport, depends on the vesicular volume that passes from the plasma to the interstitium per unit time and the partition of solute molecules in the vesicular plasma. One finds that when *K* is 5.057 nm/s C_T =20 mg/ml, or C_T/C_L =0.4, at P_L =25 cm H_2O. One notices in Table 5 that the diffusive flux for albumin in the tissue is zero since C_T is uniform and given by J_S/J_V . One assumes that at the cleft exit the solute poor flux from the paracellular pathway mixes instantaneously with the solute rich flux from the transcellular pathway, and, thus, the concentration in the tissue is constant.

When the tissue is isotonically backloaded as in Adamson et al. (2004), the J_V/A curve goes through the origin. This is easy to understand. If the hydrostatic and oncotic pressures in the lumen and in the tissue are exactly the same, the net force for filtration has to be zero at steady state. The concentration close to the cleft exit in the tissue (5 μm from the vessel wall) is insensitive to the filtration rate (or lumen pressure), see Figure 4.7A, because the EGL is the major barrier for albumin transport. This effect becomes more obvious when the tissue is backloaded at 20 mg/ml. One observes steady state reabsorption at low lumen pressure, see Figure 4.7B, because the albumin concentration behind the EGL cannot rise high enough to arrest the reabsorption. The tissue

concentration at low lumen pressure is controlled by the superfusate concentration at the leakage site and does not rise as in the Michel and Phillips experiment.

The small concentration gradient in the tissue is important since the area in the tissue space is 500 times larger than that in the cleft, and the small gradient flux in the tissue can result in a large solute flux into the cleft. The numerical relaxation scheme in the 3-D model converges slowly when there are small tissue gradients whereas the 1-D model has an analytical solution.

The definition of a Peclet number in the tissue is subtle and may not indicate the relative importance of diffusive and convective fluxes in the tissue. Pe is defined as $u_T L_T / D_T$ where L_T is the characteristic tissue length. Our 1-D model predicts that Pe in the tissue is of the order 0.1 or less when L_T=100 μm, whereas the results in Tables 3, 4 and 5 indicate that diffusive and convective fluxes in the tissue do not differ greatly. This discrepancy can be explained by the fact that the convective flux is based on the solute concentration in the tissue, whereas the diffusive flux is based on the concentration difference across the tissue, which is much smaller.

The reflection coefficient in the cleft, σ_C=0.197, is small but not negligible. This reflection coefficient produces a small but finite oncotic pressure in the cleft due to the steric exclusion of solute at the plasmalemma boundaries of the cleft. If σ_C=0, Equations (4.22), (4.24) and (4.26) show that the diffusive flux in the cleft vanishes if the tissue concentration is uniform. In this limit the tissue and cleft concentration are the same and one obtains the Michel and Phillips solution throughout both the cleft and the tissue.

Table 4.1 Cleft and junction strand gap parameters for rat mesenteric capillaries

3D model	Gap length[1]	*2d*	315 nm
	Gap spacing[1]	*2D*	3590 nm
	Depth of strand[1]	L_1	67 nm
	Total cleft depth[1]	*L*	411 nm
	Cleft height[1]	*2h*	18 nm
	Depth of tissue space	L_T	100 μm
1D model	Depth of strand[1]	L_1	67 nm
	TJ length	L_{TJ}	1.5 nm
	Total cleft depth[1]	*L*	411 nm
	Cleft height[1]	*2h*	18 nm
	Height of TJ opening	*2b*	1.58 nm
	Depth of tissue space	L_T	100 μm
	Width of tissue space	*2H*	10 μm

[1] Adamson et al., 2003

Table 4.2 Parameter values for transport for rat capillaries

EGL	Diffusion coefficient for albumin[1]	D_f	D_C/1000
	Reflection coefficient for albumin[1]	σ_f	0.94
	Retardation coefficient for albumin[1]	χ_f	0.06
Cleft	Diffusion coefficient for albumin[1]	D_C	2.0×10^{-7} cm^2/s
	Reflection coefficient for albumin	$\sigma_{f,C}$	0.197
	Retardation coefficient for albumin	χ_C	0.893
Tissue	Diffusion coefficient for albumin	D_C	2.2×10^{-7} cm^2/s
	Retardation coefficient[1]	χ_t	1

[1] Hu and Weinbaum, 1999

Table 4.3 Albumin and water fluxes per cleft when there is only paracellular pathway for albumin, $C_i=J_S/J_V$ (modified Michel and Phillips, 1991)

P_L (cm H_2O)		1	10	25	40	60
Albumin flux at $x=-L_F$ (mg/ml*nm/s)	Diffusive flux	0.657	7.20	15.15	0.660	0.002
	Convective flux	0.043	0.68	15.13	124.3	280.6
	Total flux	0.700	7.88	30.27	124.9	280.6
Albumin flux at $x=0^-$ (mg/ml*nm/s)	Diffusive flux	0.658	7.40	28.45	117.1	262.3
	Convective flux	0.042	0.473	1.83	7.82	18.32
	Total flux	0.700	7.88	30.27	124.9	280.6
Albumin flux at $x=0^+$ (mg/ml*nm/s)	Diffusive flux	0.138	1.55	5.82	20.21	35.43
	Convective flux	0.562	6.33	24.45	104.7	245.1
	Total flux	0.700	7.88	30.27	124.9	280.6
Albumin flux at $x=L^-$ (mg/ml*nm/s)	Diffusive flux	0.138	1.55	5.96	24.61	55.27
	Convective flux	0.562	6.32	24.31	100.3	225.3
	Total flux	0.700	7.88	30.27	124.9	280.6
J_V/A (nm/s)		0.007	0.113	2.52	20.71	46.76

Table 4.4 A. Albumin and water fluxes per cleft when there is only paracellular pathway for albumin and the tissue is backloaded, C_L=C_i=50 mg/ml (Adamson et al., 2004)

P_L (cm H_2O)		1	10	25	40	60
Albumin flux at x=-L_F (mg/ml*nm/s)	Diffusive flux	0.226	0.731	0.137	0.009	0.00009
	Convective flux	4.83	49.85	131.1	219.5	346.9
	Total flux	5.06	50.58	131.2	219.5	346.9
Albumin flux at x=0^- (mg/ml*nm/s)	Diffusive flux	0.276	5.84	32.36	82.04	179.3
	Convective flux	4.78	44.75	98.86	137.5	167.6
	Total flux	5.06	50.58	131.2	219.5	346.9
Albumin flux at x=0^+ (mg/ml*nm/s)	Diffusive flux	-58.90	-548.3	-1192	-1621	-1897
	Convective flux	63.96	598.9	1323	1840	2243
	Total flux	5.06	50.58	131.2	219.5	346.9
Albumin flux at x=L^- (mg/ml*nm/s)	Diffusive flux	-59.36	-593.4	-1467	-2295	-3287
	Convective flux	64.41	644.0	1598	2515	3634
	Total flux	5.06	50.58	131.2	219.5	346.9
Albumin flux at x=L^+ (mg/ml*nm/s)	Diffusive flux	-75.79	-818.9	-2332	-4254	-7607
	Convective flux	80.84	869. 5	2463	4474	7954
	Total flux	5.06	50.58	131.2	219.5	346.9
Albumin flux at x=L_B+L (mg/ml*nm/s)	Diffusive flux	-75.43	-780.3	-2054	-3439	-5435
	Convective flux	80.49	830.9	2185	3659	5782
	Total flux	5.06	50.58	131.2	219.5	346.9
J_V/A (nm/s)		0.805	8.31	21.85	36.59	57.82

Table 4.4 B. Albumin and water fluxes per cleft when there is only paracellular pathway for albumin and the tissue is backloaded, C_L=50 mg/ml, C_i=20 mg/ml (Adamson et al., 2004)

P_L (cm H_2O)		1	10	25	40	60
Albumin flux at x=-L_F (mg/ml*nm/s)	Diffusive flux	54.37	31.56	4.25	0.150	0.0007
	Convective flux	-108.9	-49.88	52.35	158.6	304.4
	Total flux	-54.55	-18.32	56.60	158.8	304.4
Albumin flux at x=0^- (mg/ml*nm/s)	Diffusive flux	0.581	3.95	37.62	111.5	233.7
	Convective flux	-55.13	-22.27	18.98	47.23	70.69
	Total flux	-54.55	-18.32	56.60	158.8	304.4
Albumin flux at x=0^+ (mg/ml*nm/s)	Diffusive flux	683.2	279.7	-197. 5	-473.3	-641.8
	Convective flux	-737.8	-298.0	254. 1	632.1	946.1
	Total flux	-54.55	-18.32	56.60	158.8	304.4
Albumin flux at x=L^- (mg/ml*nm/s)	Diffusive flux	574.9	258.4	-214.5	-608. 7	-1039
	Convective flux	-629.4	-276.8	271.1	767. 5	1344
	Total flux	-54.55	-18.32	56.60	158.8	304.4
Albumin flux at x=L^+ (mg/ml*nm/s)	Diffusive flux	604.3	299.4	-307.7	-1048	-2316
	Convective flux	-658.8	-317.7	364.3	1207	2621
	Total flux	-54.55	-18.32	56.60	158.8	304.4
Albumin flux at x=L_B+L (mg/ml*nm/s)	Diffusive flux	671.5	314.2	-292.4	-898.8	-1724
	Convective flux	-726.1	-332.6	349.0	1057	2029
	Total flux	-54.55	-18.32	56.60	158.8	304.4
J_V/A (nm/s)		-18.15	-8.31	8.73	26.44	50.73

Table 4.5 Albumin and water fluxes per cleft when there are paracellular and vesicular pathways for albumin (K=5.057 nm/s), $C_i=J_S/J_V$ (Renkin, 1992; Michel, 1997)

P_L (cm H_2O)		1	10	25	40	60
Albumin flux at $x=-L_F$ (mg/ml*nm/s)	Diffusive flux	0.581	4.86	3.96	0.301	0.002
	Convective flux	0.818	11.22	54.24	142.7	288.3
	Total flux	1.40	16.07	58.20	143.0	288.3
Albumin flux at $x=0^-$ (mg/ml*nm/s)	Diffusive flux	0.602	7.75	37.93	115.2	253.1
	Convective flux	0.798	8.32	20.27	27.76	35.19
	Total flux	1.40	16.07	58.20	143.0	288.3
Albumin flux at $x=0^+$ (mg/ml*nm/s)	Diffusive flux	-9.27	-95.29	-213.0	-228.5	-182.7
	Convective flux	10.67	111.4	271.2	371.5	471.0
	Total flux	1.40	16.07	58.20	143.0	288.3
Albumin flux at $x=L^-$ (mg/ml*nm/s)	Diffusive flux	-9.29	-97.00	-232. 2	-286.6	-288.6
	Convective flux	10.69	113.1	290.4	429.6	576.9
	Total flux	1.40	16.07	58.20	143.0	288.3
Albumin flux at $x=L^+$ (mg/ml*nm/s)	Diffusive flux	0	0	0	0	0
	Convective flux	13.31	140.8	361.6	535.0	718.4
	Total flux	13.31	140.8	361.6	535.0	718.4
Albumin flux from vesicular pathway (mg/ml*nm/s)		11.91	124.7	303.4	392.0	430.1
J_V/A (nm/s)		0.136	1.87	9.04	23.78	48.05

Figure 4.1 Geometric model of the endothelial cleft. A. 3-D model. Cleft and glycocalyx geometry based on results summarized in Table 1. P_L, π_L, hydrostatic and oncotic pressures in the vessel lumen; P_T, π_T, hydrostatic and oncotic pressures in the interstitium; L_F, thickness of the glycocalyx; L_1, depth of the TJ strand from luminal cleft entrance; L_2, distance from TJ strand to the abluminal cleft exit; L, mean value of total cleft depth; $2d$, mean gap length; $2D$, mean gap spacing. B. 1-D model. Region F is the EGL of thickness L_F. Region A is the cleft of depth L_1 before the TJ strand. Region TJ is the tight junction of depth L_{TJ}. Region B is the cleft of depth (L-L_1 - L_{TJ}). Region T is the tissue space of depth L_F and width $2H$.

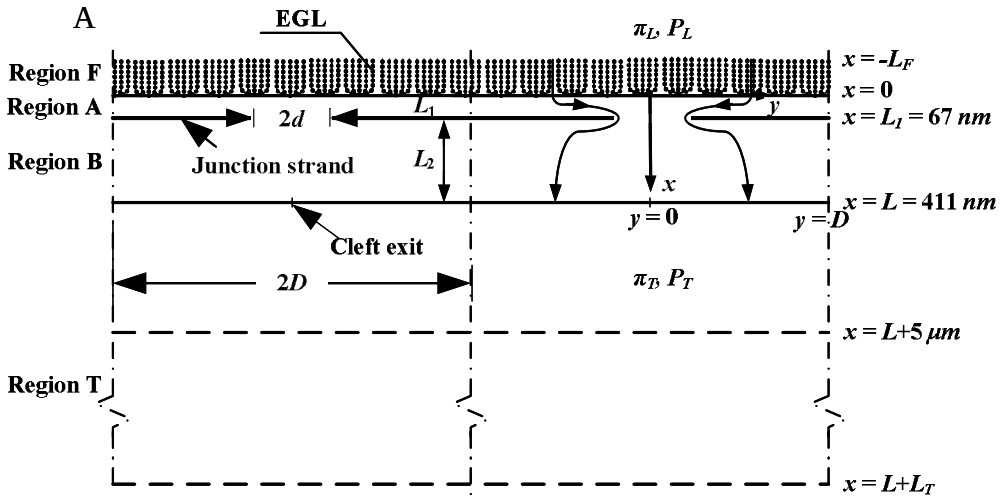
A
EGL
π_L, P_L
Region F
Region A
Region B
Region T
$x = -L_F$
$x = 0$
$x = L_1 = 67\ nm$
$x = L = 411\ nm$
$x = L+5\ \mu m$
$x = L+L_T$
$2d$
L_1
L_2
y
x
$y = 0$
$y = D$
Junction strand
Cleft exit
$2D$
π_T, P_T

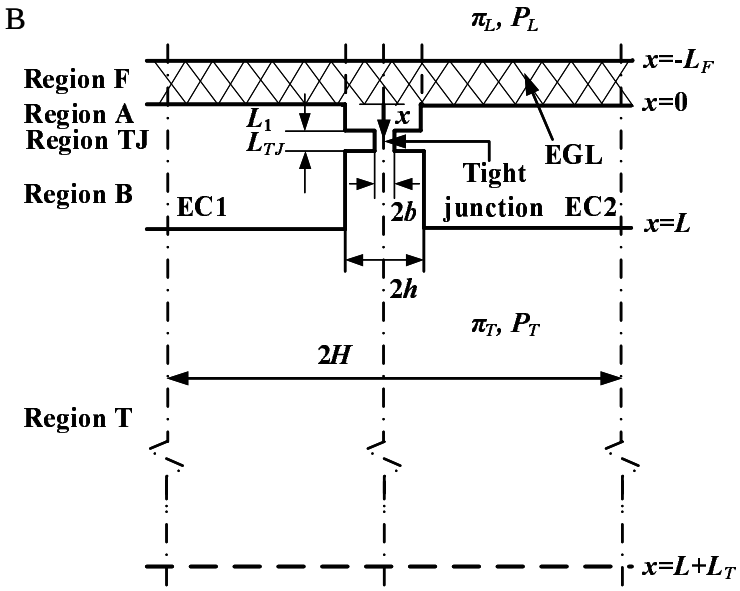
B
π_L, P_L
Region F
Region A
Region TJ
Region B
Region T
$x=-L_F$
$x=0$
$x=L$
$x=L+L_T$
L_1
L_{TJ}
x
EGL
Tight
junction
EC1
EC2
$2b$
$2h$
$2H$
π_T, P_T

Figure 4.2 3-D model predictions for pressure in the cleft for pure filtration. A. Pressure profiles at the cleft entrance (x=0), before and after the TJ strand ($x = L_1 \mp$). The structural parameters describing the cleft and TJ strand are summarized in Table 4.1. A. There is an intact 150-nm EGL. B. There is no EGL. The average $P(0)$ from A is applied as the entrance condition for the cleft. The water flux is almost doubled (0.019 μm/s vs. 0.034 μm/s for P_L =15 cm H_2O). L_p=1.3x10^{-7} cm/s/cm H_2O.

A

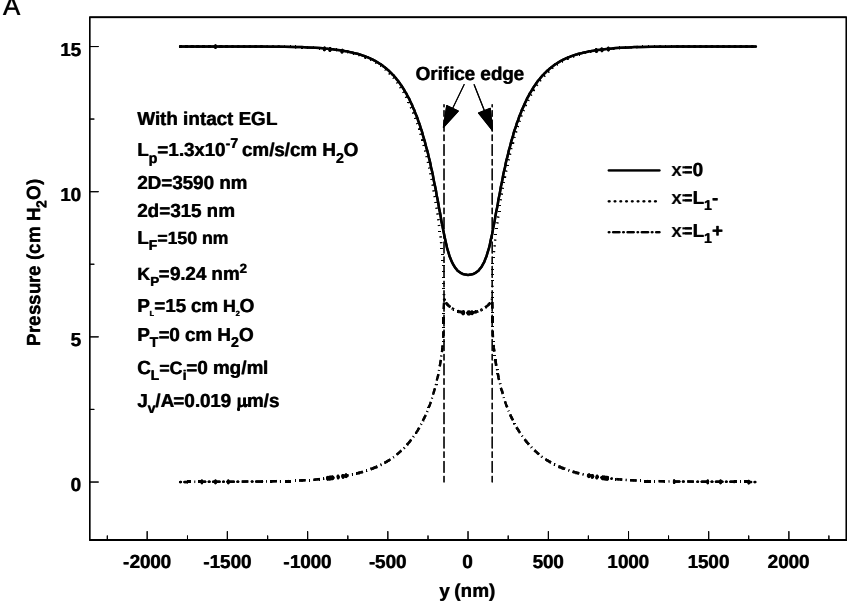
Orifice edge
With intact EGL
L_p=1.3x10^{-7} cm/s/cm H_2O
2D=3590 nm
2d=315 nm
L_F=150 nm
K_P=9.24 nm^2
P_L=15 cm H_2O
P_T=0 cm H_2O
C_L=C_i=0 mg/ml
J_V/A=0.019 μm/s
x=0
x=L_1-
x=L_1+
Pressure (cm H_2O)
y (nm)

B

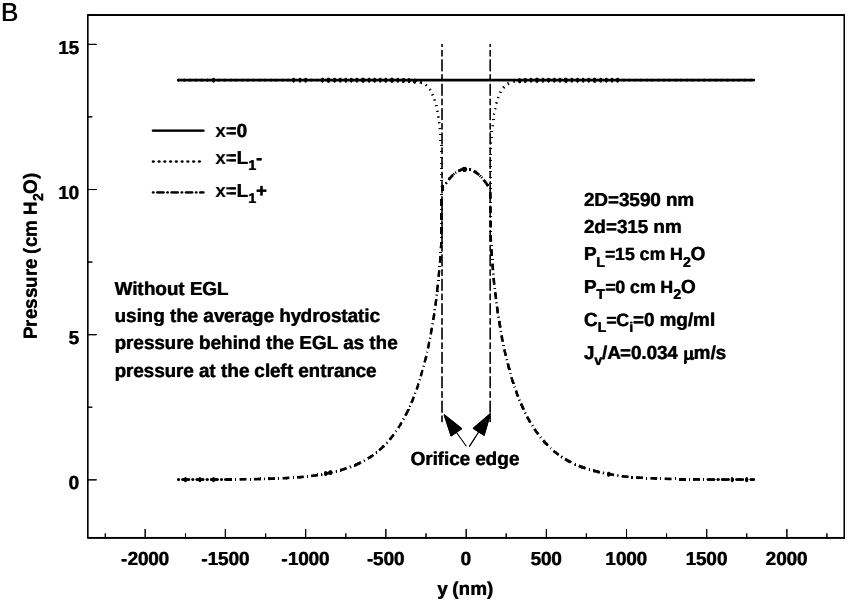
x=0
x=L_1-
x=L_1+
Without EGL
using the average hydrostatic
pressure behind the EGL as the
pressure at the cleft entrance
2D=3590 nm
2d=315 nm
P_L=15 cm H_2O
P_T=0 cm H_2O
C_L=C_i=0 mg/ml
J_V/A=0.034 μm/s
Orifice edge
Pressure (cm H_2O)
y (nm)

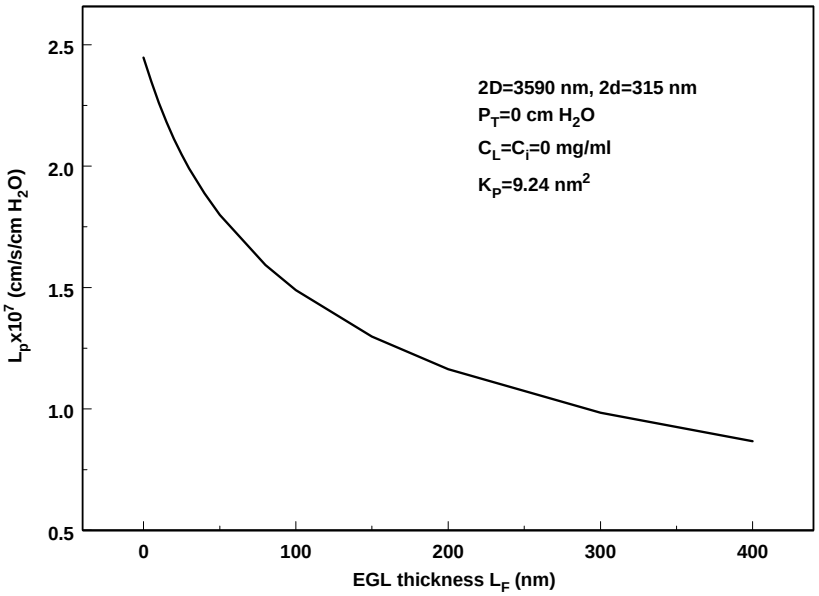

Figure 4.3 3-D model predictions for L_p as a function of L_F. Predicted L_p based on the measured parameters described in the text and listed in Table 4.1 for rat mesentery.

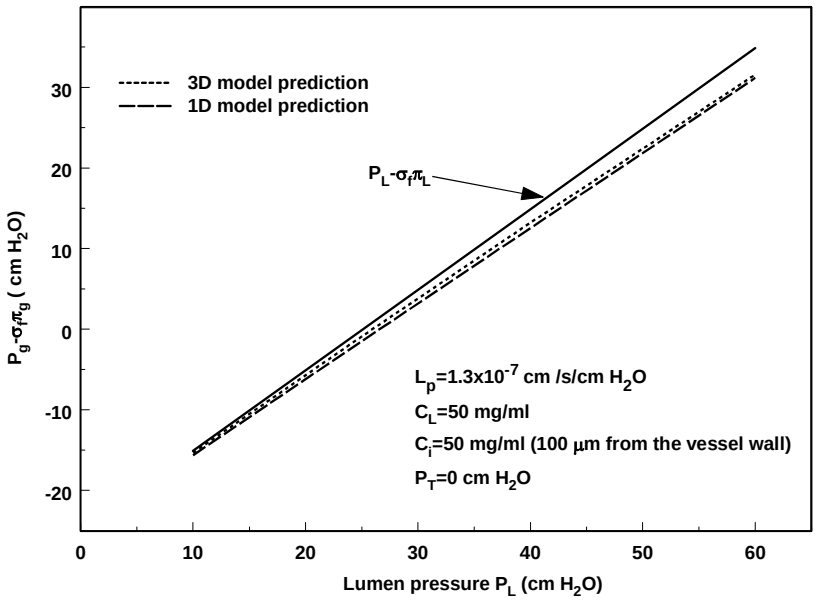

Figure 4.4 Comparison between the predictions of 1-D and 3-D models for net pressures opposing filtration behind the EGL. The results for 3-D model are the average value along *y* direction. The difference between the solid line, the sum of hydrostatic and oncotic pressure favoring filtration in the lumen, and the dotted line (3-D model prediction) or the dashed line (1-D model prediction), the equivalent pressure opposing filtration at the back of the EGL, is the net driving force for water flux. L_p=1.3x10^{-7} cm/s/cm H_2O.

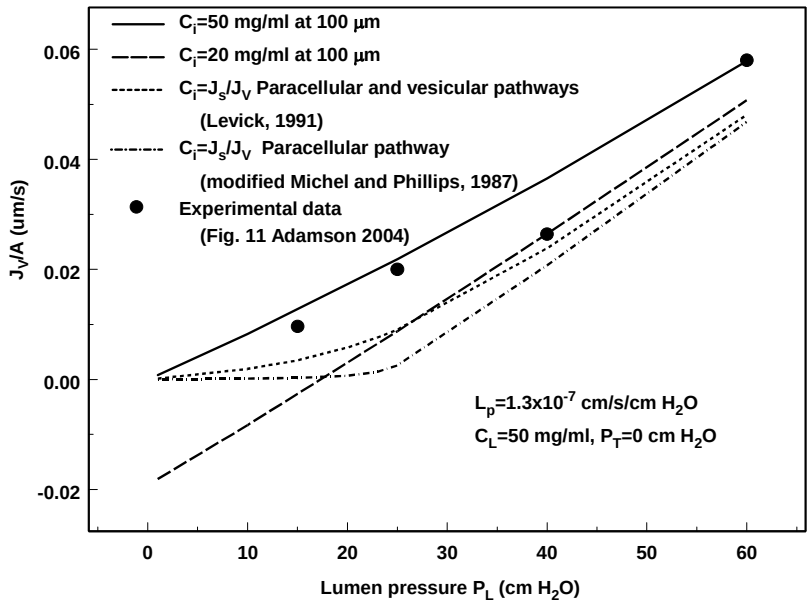

Figure 4.5 1-D model prediction for water flux. The comparison between the experimental measurements with tissue backloading (Adamson et al. 2004) and the 1-D model predictions for water flux, J_V / A, as a function of lumen pressure, P_L, based upon modified Michel and Phillips (1987) model, tissue backloading model, and combined paracellular and vesicular transport model. L_p=1.3x10^{-7} cm/s/cm H_2O. Modified Michel and Phillips model and combined paracellular and vesicular transport model predict that there is no steady state reabsorption even at very low lumen pressure. Tissue backloading model predicts that when the tissue is isotonically loaded, the J_V / A curve goes through the origin, and that when the tissue is backloaded at 20 mg/ml, there is steady state reabsorption.

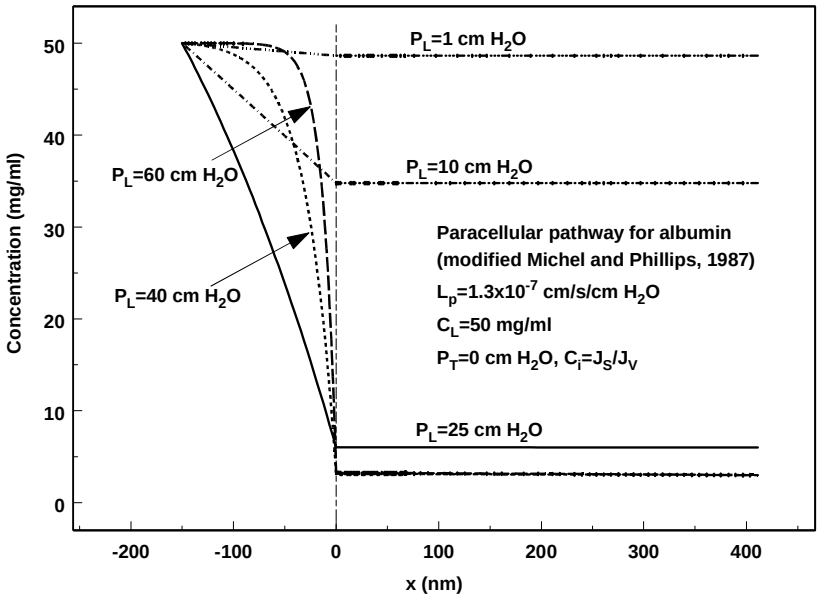

Figure 4.6 Concentration profiles predicted by modified Michel and Phillips (1987) model. L_p=1.3x10^{-7} cm/s/cm H_2O. The entire solute flux passes through the paracellular pathway. There is a very small concentration gradient in the cleft when σ_C =0.197.

Figure 4.7 Concentration profiles predicted by tissue backloading model. L_p= 1.3x10^{-7} cm/s/cm H_2O. The entire solute flux passes through the paracellular pathway. The tissue is backloaded at 50 mg/ml (A) and at 20 mg/ml (B). A. The albumin concentration at the cleft exit is high and relatively insensitive to the filtration rate (or the lumen pressure). The solute concentration behind the EGL is substantially < than the cleft exit concentration. B. When the lumen pressure is low, the concentration at the back of the EGL does not rise high enough to arrest the reabsorption, as in Figure 4.7A.

A

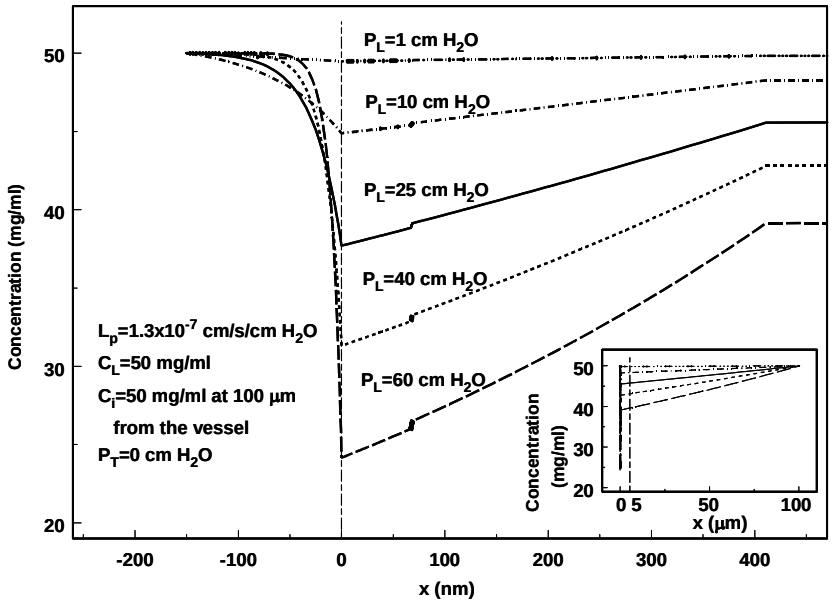
Concentration (mg/ml)
x (nm)
P_L=1 cm H_2O
P_L=10 cm H_2O
P_L=25 cm H_2O
P_L=40 cm H_2O
P_L=60 cm H_2O
L_p=1.3x10^{-7} cm/s/cm H_2O
C_L=50 mg/ml
C_i=50 mg/ml at 100 µm
from the vessel
P_T=0 cm H_2O
Concentration (mg/ml)
x (µm)

B

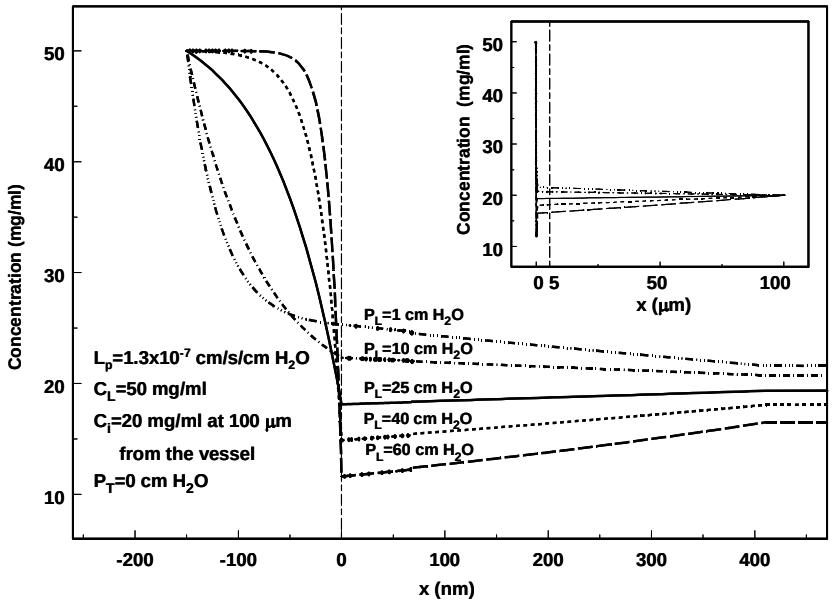
Concentration (mg/ml)
x (nm)
P_L=1 cm H_2O
P_L=10 cm H_2O
P_L=25 cm H_2O
P_L=40 cm H_2O
P_L=60 cm H_2O
L_p=1.3x10^{-7} cm/s/cm H_2O
C_L=50 mg/ml
C_i=20 mg/ml at 100 µm
from the vessel
P_T=0 cm H_2O
Concentration (mg/ml)
x (µm)

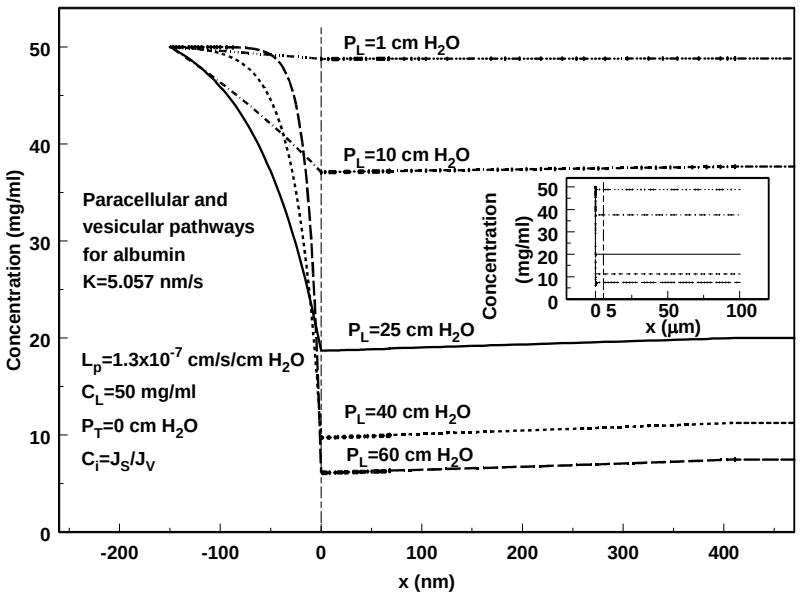

Figure 4.8 Concentration profiles predicted by the combined paracellular and vesicular transport model. L_p=1.3x10^{-7} cm/s/cm H_2O. There also is a transcellular vesicle pathway in addition to a paracellular pathway. At P_L =25 cm H_2O, the average pressure in the capillary bed whose arterial pressure is about 35 cm H_2O and venous pressure is about 15 cm H_2O, C_T, is 20 mg/ml, or 40 percent of the lumen concentration, when K=5.057 nm/s.

Chapter 5 The Mechanism of Oncotic Flow in a Fiber Matrix Layer with Application to the Endothelial Glycocalyx

5.1 INTRODUCTION

The thermodynamic theory for the osmotic flow through porous membranes is largely based on the movement of water and solute through long circular cylindrical pores, Anderson and Malone (1974). This theory is applicable to cell membrane proteins with hydrophilic interiors which either allow only the passage of water, such as aquaporins, or have larger channels that permit the passage of water and the restricted convection and diffusion of small solutes. In contrast to this classical theory, Michel (1997) and Weinbaum (1998) have independently proposed that the oncotic forces that are exerted across the capillary wall are due to the sieving of plasma proteins by a surface fiber matrix layer of proteoglycans and glycoproteins that is called the endothelial glycocalyx layer (EGL). The Michel-Weinbaum model further suggests that the pressure and oncotic forces in the Starling equation for fluid exchange should be applied just across this layer rather than globally between plasma and tissue as previously believed. Due to the presence of a junction strand in the interendothelial cleft behind the EGL, there is a strong asymmetry in the effectiveness of solutes located on the plasma and tissue fronts due to the washout of solutes from the protected region on the lumen side of the tight junction strand. Strong evidence in support of this hypothesis is provided by the recent experiments in frog (Hu et al. 2000) and rat mesentery capillaries (Adamson et al. 2004) where the tissue is back loaded with albumin at the same concentration as the lumen and nearly the full plasma oncotic force is observed.

Whereas a rigorous theory based on classical transport and thermodynamic relations has been developed by Anderson and Malone (1974) to determine the reflection coefficient for long circular cylindrical pores, no equivalent analysis has been developed for a sieving fiber matrix layer. The central tenet in the Anderson and Malone model is that there is an exclusion region near the walls of the pores producing a radial discontinuity in hydrostatic pressure and concentration that provides the driving force for the osmotic flow. In the theory derived herein we shall examine the equivalent effect that develops along the walls of the fibers. As in the case of the circular cylindrical pores, one must assume a simplified geometry for the fibers in the matrix layer. Measurements of the Starling forces led Michel (1983) to propose two decades ago that the EGL was an ordered structure with a sieving dimension that was close to the diameter of albumin, 7 nm. However, there was little information on the organization of this layer until the recent experiments of Squire et al. (2001) showed that it contained a 3-D quasi-periodic array of 10-12 nm scattering centers that were spaced at approximately 20 nm intervals along the axes of the core protein fibers. A larger hexagonal periodicity with a 100-nm spacing was also observed near the plane of the membrane, which Squire et al. proposed were focal membrane complexes associated with the underlying actin cortical cytoskeleton (ACC), see Figure 5.1A. This conceptual picture was then converted into a mathematical model with hexagonal symmetry in Weinbaum et al. (2003), see Figure 5.1B, where the core proteins were arranged in bush like structures that formed an hexagonal lattice. In this paper we shall use this idealized fiber geometry to develop a theory for determining the reflection coefficient in an ordered fiber matrix layer.

Osmotic or oncotic flow is generated between solutions of different concentrations

separated by a discriminating barrier. If the solutes are larger than the pores the barrier is semipermeable, solvent can pass through it freely, while solutes will be impermeable. For semipermeable membranes Mauro (1960) and Ray (1960) advanced independently a model to describe the equivalence between the pressure and osmotic driving forces at the membrane-solution interface (fluid boundary between bulk and pore fluid). Whereas the solutes exert their full osmotic pressures across a semipermeable barrier, Staverman (1951) proposed that for a barrier that was partially permeable to solutes, one must introduce a reflection coefficient, σ_0, to account for the fraction of the full osmotic pressure that would be exerted across a porous (leaky) membrane. For a leaky membrane, the osmotic flow is determined by the difference in osmotic pressures on each side of the barrier, as well as the difference in hydrostatic pressures.

$$J_V / A = L_p \left[\Delta P_\infty - \sigma_0 \Delta \pi_\infty \right], \tag{5.1}$$

where J_V / A is the fluid filtration flux across the barrier, L_p is the hydraulic permeability, ∞ denotes the bulk solution conditions, and ΔP and $\Delta \pi$ are the differences in the hydrostatic and osmotic pressures across the barrier, respectively.

Due to the striking similarity between the sieving of macromolecules by artificial porous membranes and the ultrafiltration of plasma proteins at the capillary wall, many investigators have used pore or slit theory to describe the oncotic force exerted at the capillary wall (Curry, 1984). The basic mechanism for osmotic flow in pores is shown in Figure 5.2 taken from Anderson and Malone (1974). The steric exclusion of solute from the pore wall establishes an equilibrium pressure drop across the imaginary boundary $r = r_w - a$, which produces the driving force for osmotic flow. The theoretical model in Anderson and Malone (1974) assumes that the pore length is much > than pore radius so

that the end effects are negligible. This theory is extended in Yan and Weinbaum (1986) for short pores where pore entrance and exit behaviors are described. Using a rigorous theory based on classical transport and thermodynamic relations, Anderson and Malone (1974) showed that for a circular pore with spherical solutes that experience only steric exclusion,

$$\sigma_0 = (1-\phi)^2, \tag{5.2}$$

where ϕ is the partition coefficient defined as the ratio between the area available to solute and that available to water, i.e.,

$$\phi = \frac{\pi(R-a)^2}{\pi R^2} = \left(1-\frac{a}{R}\right)^2. \tag{5.3}$$

In the absence of an equivalent theory for a fiber matrix layer Curry and Michel (1980) suggested an expression identical to Equation (5.2) to describe the reflection coefficient for the oncotic forces developed by the surface matrix in capillary endothelium

$$\sigma_0 = (1-\phi_f)^2, \tag{5.4}$$

since the flow between fibers can be approximated as pseudo-Poiseuillean. The partition coefficient ϕ_f is defined by the ratio between the area available to the solute and that of a periodic unit of the fiber matrix. Equation (5.4) is an intuitive expression without detailed derivation. One of the objectives of this study is to examine the validity of this simple intuitive expression for a periodic fiber array.

5.2 MODEL DESCRIPTION

In the past the molecular sieve associated with the surface glycocalyx was assumed

to be a fiber matrix composed of glycoproteins with extended glycan side chains of typically 0.6 nm radius and 7-8 nm gap spacing associated with the disaccharide repeat along the core protein. This repeat distance was assumed in Fu *et al*. (1994) and subsequent studies (Hu and Weinbaum, 1999; Hu *et al*., 2000) to provide the dimensions of the molecular sieve for albumin. It is typical of the two-dimensional appearance of glycan side chains along chondroitan sulfate proteoglycans when observed on carbon filters (Buckwalter and Rosenberg, 1982).

The observations by Squire et al. (2001) provide an alternative picture for the sieving structure of the EGL. Using computed autocorrelation functions and Fourier transforms of electron microscope images obtained from both new (Squire et al., 2001) and previous studies (Clough et al., 1988) of frog mesenteric capillaries, Squire et al. were able to identify for the first time the quasi-periodic substructure of the glycocalyx and the anchoring foci that appear to emanate from the underlying ACC. The computer enhanced images showed that the glycocalyx is a 3-D fibrous meshwork with a characteristic spacing of 20 nm in all directions and that the effective diameter of the periodic scattering centers was 10-12 nm. These periodic scatting centers could be either aggregated glycan side chains that take on a spherical appearance or plasma proteins that are attracted by negative charge repeats. Using a freeze fracture replica from a rare section where the fracture plane passed parallel and close to the endothelial surface, they also showed that anchoring foci formed an hexagonal array with an intercluster spacing of typically 100 nm in frog lung capillary. The schematic organization of the EGL is shown in Figure 5.1 taken from Weinbaum et al. (2003). Figure 5.1B is an *en face* view of the idealized endothelial layer model which assumes both an hexagonal arrangement of the core

proteins in each cluster and an hexagonal arrangement of the actin filaments in the underlying ACC. To simplify the description of the EGL's function as a molecular sieve, the core proteins with their 10-12 nm scattering centers are replaced by circular cylindrical fibers whose diameter is the same as the scattering centers. Figure 5.3A is a periodic unit in this idealized fiber array for the EGL. r_f is the fiber radius, and δ is the open spacing between fibers. Based on the measurements in Squire et al. (2001), Weinbaum et al. (2003) assume r_f=6 nm and δ=8 nm. The partition coefficient ϕ_f for the hexagonally ordered fiber array in Figure 5.3A is described by

$$\phi_f = \frac{\frac{\sqrt{3}}{4}(2r_f+\delta)^2 - \frac{1}{2}\pi(r_f+a)^2}{\frac{\sqrt{3}}{4}(2r_f+\delta)^2} = 1 - \frac{\frac{1}{2}\pi r_f^{\,2}\left(1+\frac{a}{r_f}\right)^2}{\frac{\sqrt{3}}{4}(2r_f+\delta)^2} = 1 - V_f\left(1+\frac{a}{r_f}\right)^2, \tag{5.5}$$

in which V_f is the solid fraction defined as

$$V_f = \frac{\frac{1}{2}\pi r_f^{\,2}}{\frac{\sqrt{3}}{4}(2r_f+\delta)^2}. \tag{5.6}$$

Equation (5.5) takes account of the steric exclusion of a solute of radius a by a fiber of radius r_f.

5.3 METHODS

5.3.1 Effective radius R_{eff}

For the flow parallel to the fiber axis in the periodic unit shown in Figure 5.3A, the dashed lines, ab, cb, and db, are lines of flow symmetry along which $\frac{\partial u}{\partial n} = 0$, where u is

the local velocity along the fiber axis and *n* is normal to ab, cb, or db. The lines abc, abd, and cbd can be replaced by circular arcs with an effective radius R_{eff} as shown in Figure 5.3B. R_{eff} is chosen such that one half of the resulting fluid annulus has the same area as the open flow cross-section in Figure 5.3A, i.e.,

$$\frac{1}{2}\pi\left(R_{eff}^{\ 2}-r_f^{\ 2}\right)=\frac{\sqrt{3}}{4}\left(2r_f+\delta\right)^2-\frac{1}{2}\pi r_f^{\ 2}. \tag{5.7}$$

Solving for R_{eff} one obtains

$$R_{eff}=\frac{3^{1/4}}{\sqrt{2\pi}}\left(2r_f+\delta\right). \tag{5.8}$$

For r_f =6 nm and δ=8 nm, R_{eff} =10.5 nm. Therefore, the periodic unit in Figure 5.3A can be approximated by a fiber surrounded by a fluid annulus whose outer radius is R_{eff} as shown in Figure 5.3B. R_{eff} is much smaller than EGL thickness, L_F, which has been estimated to be vary between 150 nm and 400 nm. This assumption in Figure 5.3B enables us to take advantage of a cylindrical coordinate system with symmetry about the longitudinal axis of the fiber and also neglect end effects.

Applying Equation (5.8) to Equations (5.6) and (5.7), one finds that

$$\phi_f=\frac{\frac{\pi R_{eff}^{\ 2}}{2}-\frac{\pi\left(r_f+a\right)^2}{2}}{\frac{\pi R_{eff}^{\ 2}}{2}}=1-\left(\frac{r_f}{R_{eff}}+\frac{a}{R_{eff}}\right)^2. \tag{5.9}$$

5.3.2 Reflection coefficient σ_0

The Gibbs-Du hem equation is used to relate pressure and potential gradients in the radial direction in the fluid annulus $r_f < r \le R_{eff}$ in Figure 5.3B. Since the chemical potential is constant in the radial direction,

$$\frac{\partial P}{\partial r} + C \cdot \frac{d\psi}{dr} = 0 , \tag{5.10}$$

where C is the solute concentration, and $\psi(r)$ is the solute potential energy field which controls the radial distribution of the solute in the annulus. $\psi(r)$ could include London forces, electric effects as well as steric exclusion. The Boltzmann equation is valid if one assumes a constant activity coefficient of solute and low volume fraction. Therefore, the solute concentration is given by

$$C(r,z) = C_{R_{eff}}(z) exp\left[-\frac{\psi(r) - \psi(R_{eff})}{RT} \right], \tag{5.11}$$

where $C_{R_{eff}}$ is the value of C at $r = R_{eff}$ in Figure 5.3B and z is in the axial direction of the fibers.

Our model differs from Anderson and Malone (1974) in that our model describes the fluid annulus surrounding individual fibers, as shown in Figure 5.3B, rather than circular cylindrical pores. Substituting Equation (5.11) into Equation (5.10) and integrating the resultant equation, one finds

$$P(r,z) = P_{R_{eff}}(z) - \pi_{R_{eff}}(z)\left\{ 1 - exp\left[-\frac{\psi(r) - \psi(R_{eff})}{RT} \right] \right\}, \tag{5.12}$$

where $\pi_{R_{eff}}(z)$ is the axial variation of the oncotic pressure, $RTC_{R_{eff}}(z)$, along the fiber axis. Equation (5.12) indicates the coupling of oncotic and hydrostatic pressures in generating the driving force for the bulk flow through the EGL.

Neglecting the end effects, the momentum balance is

$$\frac{\mu}{r}\frac{\partial}{\partial r}\left(r\frac{\partial U}{\partial r} \right) - \frac{\partial P}{\partial z} = 0 , \tag{5.13}$$

where $U = U(r,z)$ is the axial velocity. The boundary conditions for Equation (5.13) are

$$U(r,z) = 0 \qquad \text{at } r = \alpha R_{eff}, \tag{5.14a}$$

$$\frac{\partial U(r,z)}{\partial r} = 0 \qquad \text{at } r = R_{eff}, \tag{5.14b}$$

where $\alpha = \frac{r_f}{R_{eff}}$. Equation (5.14a) is the no-slip condition at the fiber surface, while Equation (5.14b) is the symmetry condition at the boundary of the fluid annulus. Substituting Equation (5.12) into Equation (5.11), integrating, and applying the boundary conditions (5.14a) and (5.14b), one finds

$$U(r,z) = \frac{1}{4\mu}\frac{\partial P_{R_{eff}}}{\partial z} {R_{eff}}^2 \left[\left(\frac{r}{R_{eff}}\right)^2 - 2\ln\left(\frac{r}{R_{eff}}\right) + 2\ln(\alpha) - \alpha^2 \right]$$

$$+ \frac{1}{\mu}\frac{\partial \pi_{R_{eff}}}{\partial z} \int_{r_f}^{r} \frac{dy}{y} \int_{y}^{R_{eff}} x\left\{1 - \exp\left[-\frac{\psi(x) - \psi\left(R_{eff}\right)}{RT}\right]\right\} dx. \tag{5.15}$$

Therefore, the average velocity over an annular cross section is

$$\bar{U} = -\frac{\partial P_{R_{eff}}}{\partial z} \frac{\frac{{R_{eff}}^4}{2}\ln\left(\frac{R_{eff}}{r_f}\right) + \frac{{r_f}^2 {R_{eff}}^2}{2} - \frac{{r_f}^4}{8} - \frac{3{R_{eff}}^4}{8}}{\mu\left({R_{eff}}^2 - {r_f}^2\right)}$$

$$+ \frac{1}{\mu\left({R_{eff}}^2 - {r_f}^2\right)} \frac{\partial \pi_{R_{eff}}}{\partial z} \int_{r_f}^{R_{eff}} 2r dr \int_{r_f}^{r} \frac{dy}{y} \int_{y}^{R_{eff}} x\left\{1 - \exp\left[-\frac{\psi(x) - \psi\left(R_{eff}\right)}{RT}\right]\right\} dx. \tag{5.16}$$

By continuity $\bar{U}$ is independent of z, Equation (5.16) can be directly integrated along the fiber axis to obtain

$$\bar{U} = \frac{L_{FM}}{\varepsilon}\left\{\left[P_{R_{eff}}(0) - P_{R_{eff}}(L_F)\right] - B \cdot \left[\pi_{R_{eff}}(0) - \pi_{R_{eff}}(L_F)\right]\right\}, \tag{5.17}$$

where

$$\frac{L_{FM}}{\varepsilon} = \frac{R_{eff}^{\ 4} \ln\left(\frac{R_{eff}}{r_f}\right) + r_f^{\ 2} R_{eff}^{\ 2} - \frac{r_f^{\ 4}}{4} - \frac{3R_{eff}^{\ 4}}{4}}{2\mu L_F\left(R_{eff}^{\ 2} - r_f^{\ 2}\right)}$$

$$= \frac{R_{eff}^{\ 2}\left[\frac{\alpha^2}{2} - \frac{\alpha^4}{8} - \frac{3}{8} - \frac{\ln(\alpha)}{2}\right]}{\mu L_F\left(1-\alpha^2\right)}, \tag{5.18}$$

and

$$B = \frac{\int_{r_f}^{R_{eff}} 2r dr \int_{r_f}^{r} \frac{dy}{y} \int_{y}^{R_{eff}} x\left\{1 - exp\left[-\frac{\psi(x) - \psi\left(R_{eff}\right)}{RT}\right]\right\} dx}{\frac{R_{eff}^{\ 4}}{2} ln\left(\frac{R_{eff}}{r_f}\right) + \frac{r_f^{\ 2} R_{eff}^{\ 2}}{2} - \frac{r_f^{\ 4}}{8} - \frac{3R_{eff}^{\ 4}}{8}}, \tag{5.19}$$

where L_{FM} is the hydraulic permeability of the fiber matrix, and ε is the void volume fraction of the fiber matrix.

The Boltzmann and Gibbs-Duhem relations are applied at the cylinder ends.

$$\pi_{R_{eff}}(0) = \pi_{0\infty}\, exp\left[-\frac{\psi\left(R_{eff}\right)}{RT}\right], \tag{5.20a}$$

$$\pi_{R_{eff}}\left(L_F\right) = \pi_{L_F\infty} \exp\left[-\frac{\psi\left(R_{eff}\right)}{RT}\right], \tag{5.20b}$$

$$P_{R_{eff}}(0) = P_{0\infty} - \pi_{0\infty}\left\{1 - exp\left[-\frac{\psi\left(R_{eff}\right)}{RT}\right]\right\}, \tag{5.20c}$$

$$P_{R_{eff}}\left(L_F\right) = P_{L_f\infty} - \pi_{L_F\infty}\left\{1 - \exp\left[-\frac{\psi\left(R_{eff}\right)}{RT}\right]\right\}, \tag{5.20d}$$

where $\pi_{0\infty}$, $\pi_{L_f\infty}$, $P_{0\infty}$, and $P_{L_f\infty}$ denote the oncotic and hydrostatic pressures in the bulk fluid phase at the EGL entrance and exit. Substituting relations (5.20a)-(5.20d) into

Equation (5.17), one obtains

$$J_V / A = L_{FM}\left(\Delta P_\infty - \sigma_0 \Delta \pi_\infty\right), \tag{5.21}$$

in which

$$\Delta P_\infty = P_{0\infty} - P_{L_f\infty}, \tag{5.22a}$$

$$\Delta \pi_\infty = \pi_{0\infty} - \pi_{L_f\infty}, \tag{5.22b}$$

and

$$\begin{aligned}\sigma_0 &= 1 - \exp\left[-\frac{\psi\left(R_{eff}\right)}{RT}\right] + B\exp\left[-\frac{\psi\left(R_{eff}\right)}{RT}\right] \\ &= 1 - \frac{\int_{r_f}^{R_{eff}} 2rdr \int_{r_f}^{r} \frac{dy}{y} \int_{y}^{R_{eff}} x\, exp\left[-\frac{\psi(x)}{RT}\right]dx}{\frac{R_{eff}^{\,4}}{2} ln\left(\frac{R_{eff}}{r_f}\right) + \frac{r_f^{\,2} R_{eff}^{\,2}}{2} - \frac{r_f^{\,4}}{8} - \frac{3R_{eff}^{\,4}}{8}}.\end{aligned} \tag{5.23}$$

Note that the water flux J_V / A through the fiber matrix has been substituted for the void volume flux $\bar{U}$ times the void volume fraction.

5.3.3 Steric exclusion with spherical solute molecules

One cannot calculate σ_f using Equation (5.23) unless $\psi(r)$ is a known function. The simplest model is that for pure steric exclusion of the solute molecules treated as rigid spheres of radius *a*. The solute potential is given by the steric effect alone. Therefore,

$$\psi(r) \to \infty \qquad r_f < r \le r_f + a, \tag{5.24a}$$

$$\psi(r) = 0 \qquad r_f + a < r \le R_{eff}. \tag{5.24b}$$

Accordingly, we define a step function

$$\exp\left[-\frac{\psi(r)}{RT}\right] = H\left[r - \left(r_f + a\right)\right]. \tag{5.25}$$

Substituting Equation (5.25) into Equation (5.23), one finds

$$\sigma_0 = B = 1 - \frac{\int_{r_f}^{R_{eff}} 2rdr \int_{r_f}^{r} \frac{dy}{y} \int_{y}^{R_{eff}} xH\left[x-\left(r_f+a\right)\right]dx}{\frac{R_{eff}^{\ 4}}{2}\ln\left(\frac{R_{eff}}{r_f}\right)+\frac{r_f^{\ 2}R_{eff}^{\ 2}}{2}-\frac{r_f^{\ 4}}{8}-\frac{3R_{eff}^{\ 4}}{8}}. \tag{5.26}$$

Evaluating the interrals in Equation (5.26) one obtains

$$\sigma_0 = \frac{\frac{1}{4}\left(\frac{a}{R_{eff}}\right)^2+\frac{1}{2}\left(\frac{a}{R_{eff}}\right)^3\left(\frac{r_f}{R_{eff}}\right)+\frac{1}{8}\left(\frac{a}{R_{eff}}\right)^4+\frac{1}{2}\left(\frac{a}{R_{eff}}\right)^2\left(\frac{r_f}{R_{eff}}\right)^2+\frac{1}{2}\left(\frac{a}{R_{eff}}\right)\left(\frac{r_f}{R_{eff}}\right)-\frac{1}{2}\left(\frac{a}{R_{eff}}+\frac{r_f}{R_{eff}}\right)^2\ln\left(1+\frac{a}{r_f}\right)}{\frac{3}{8}+\frac{1}{8}\left(\frac{r_f}{R_{eff}}\right)^4+\frac{1}{2}\ln\left(\frac{r_f}{R_{eff}}\right)-\frac{1}{2}\left(\frac{r_f}{R_{eff}}\right)^2}. \tag{5.27}$$

Equation (5.27) can be written in more compact form using the definition (5.14) for α and introducing a second dimensionless length parameter

$$\beta = \frac{a}{R_{eff}}, \tag{5.28}$$

$$\sigma_0 = \frac{\frac{\beta^2}{4}+\frac{\alpha\beta^3}{2}+\frac{\beta^4}{8}+\frac{\alpha^2\beta^2}{2}+\frac{\alpha\beta}{2}-\frac{(\alpha+\beta)^2}{2}\ln\left(1+\frac{\beta}{\alpha}\right)}{\frac{3}{8}+\frac{\alpha^4}{8}+\frac{1}{2}\ln(\alpha)-\frac{\alpha^2}{2}}. \tag{5.29}$$

In terms of α and β the expression for ϕ_f in Equation (5.9) can be simplified to

$$\phi_f = 1-(\alpha+\beta)^2. \tag{5.30}$$

We next wish to examine the pressure distribution and velocity profiles in the excluded zone, $r_f < r \le r_f + a$, and in the fluid annulus, $r_f + a < r \le R_{eff}$. In the excluded zone of thickness a adjacent to the fiber wall, there is no solute. In the fluid annulus the solute equilibrium distribution is only a function of z. This radial partitioning establishes an equilibrium pressure drop across the imaginary boundary $r = r_f + a$:

$$P_e(z) = P_{ann}(z) - \pi_{ann}(z), \tag{5.31}$$

since $P_{ann}(z) = P_{R_{eff}}(z)$ and $\pi_{ann}(z) = \pi_{R_{eff}}(z)$. The subscript *e* denotes the excluded region, *ann* denotes fluid annulus region outside the excluded region, and $\pi_{ann}(z)$ is the thermodynamic oncotic pressure one would measure at the concentration $C(z)$ in the fluid annulus region. The mechanism for oncotic flow across the fiber matrix is clear from Equation (5.31). The steric exclusion of solute near the fiber wall creates an abrupt pressure change proportional to the solute concentration; thus, an axial concentration gradient in the fluid annulus region generates an axial pressure gradient in the excluded region near the fiber boundary which is the driving force for the fluid in the annulus. The equation for the velocity profile is derived from Equation (5.15). In the fluid annulus

$$U_{ann}(r,z) = \frac{\partial P_{ann}}{\partial z}\frac{R_{eff}^{\,2}}{4\mu}\left[\left(\frac{r}{R_{eff}}\right)^2 - 2\ln\left(\frac{r}{R_{eff}}\right) + 2\ln(\alpha) - \alpha^2\right] + U_{ann,on\cot ic}(z). \tag{5.32A}$$

$$U_{ann,on\cot ic}(z) = \frac{\partial \pi_{ann}}{\partial z}\frac{R_{eff}^{\,2}}{4\mu}\left[2(\alpha+\beta)^2\ln\left(1+\frac{\beta}{\alpha}\right) - \beta^2 - 2\alpha\beta\right]. \tag{5.32B}$$

In the excluded zone,

$$U_e(r,z) = \frac{\partial P_{ann}}{\partial z}\frac{R_{eff}^{\,2}}{4\mu}\left[\left(\frac{r}{R_{eff}}\right)^2 - 2\ln\left(\frac{r}{R_{eff}}\right) + 2\ln(\alpha) - \alpha^2\right] + U_{e,on\cot ic}(r,z). \tag{5.33A}$$

$$U_{e,on\cot ic}(r,z) = \frac{\partial \pi_{ann}}{\partial z}\frac{R_{eff}^{\,2}}{4\mu}\left[2(\alpha+\beta)^2\ln\left(\frac{r}{r_f}\right) - \left(\frac{r}{R_{eff}}\right)^2 + \alpha^2\right]. \tag{5.33B}$$

Note that Equation (5.32B), which describes the oncotic contributions to the velocity profiles, is independent of *r* and, thus, non-Poiseuillean in nature. However, the oncotic contribution in the excluded zone is a function of *r* containing both parabolic and

logarithmic terms.

The average velocity derived from Equation (5.16) is

$$\bar{U} = -\frac{\partial P_{ann}}{\partial z}\frac{R_{eff}{}^2}{\mu\left(1-\alpha^2\right)}\left[\frac{\alpha^2}{2}-\frac{\alpha^4}{8}-\frac{3}{8}-\frac{\ln(\alpha)}{2}\right]$$

$$+\frac{\partial \pi_{ann}}{\partial z}\frac{R_{eff}{}^2}{\mu\left(1-\alpha^2\right)}\left[\frac{1}{2}(\alpha+\beta)^2\ln\left(1+\frac{\beta}{\alpha}\right)-\frac{\alpha\beta}{2}-\frac{\beta^2}{4}-\frac{\alpha\beta^3}{2}-\frac{\alpha^2\beta^2}{2}-\frac{\beta^4}{8}\right]. \qquad (5.34)$$

As mentioned in Anderson and Melone (1974) the exact determination of $\frac{\partial P_{ann}}{\partial z}$ and $\frac{\partial \pi_{ann}}{\partial z}$ requires the solution of the mass flux equation for solute, which is coupled to the velocity profile. When the bulk hydrostatic pressures at both sides are the same, $\frac{\partial P_{ann}}{\partial z}$ is close but not equal to zero, and the velocity in the fluid annulus is relatively flat since $U_{ann,on\cot ic}(z)$ is not a function of r. On the other hand, $U_e(r,z)$ is a function of r. A sketch of a typical axial velocity profile is shown in Figure 5.3B.

5.4 RESULTS

Equations (5.4) and (5.27) for σ_0 are quite different in form. We would like to see how they compare with one another for the structural model proposed in Squire et al. (2001) and Weinbaum et al. (2003) for the EGL where r_f=6 nm, and also when r_f=2 nm, a typical radius of the central core protein monomer in proteoglycans. In Figure 5.4, 5.5 and 5.6 we examine typical small (sodium fluorescein a=0.45 nm), medium (α-lactalbumin a=2.0 nm), and large molecules (albumin a=3.5 nm), respectively.

For small and medium size solutes, the discrepancy between the results predicted by

Equations (5.4) and (5.27) when r_f=6 nm is significant, while for the large solute, the discrepancy is much smaller. Equation (5.4) predicts that for all solute sizes there is a substantial difference in the reflection coefficient at the same δ for both values of r_f, while Equation (5.27) predicts a minor difference, especially for values of δ in the vicinity of 8 nm, the open fiber gap estimated in Squire et al. (2001) and Weinbaum et al. (2003) where the scattering centers were spaced at 20 nm intervals and were of 12 nm diameter.

For a = 3.5 nm (albumin), if r_f = 0.6 nm and δ= 8 nm, values typical of extended glycosaminoglycan side chains along a core protein monomer, Equation (5.4) predicts that σ_0 = 0.52. In contrast, if r_f = 6 nm and δ= 8 nm, Equation (5.27) predicts that σ_0 = 0.64, and σ_0 increases to 0.9 for δ= 6.5 nm.

Figure 5.7 compares the predictions for σ_0 as a function of the partition coefficient, ϕ_f, between pore theory (long dashed curves) and Equation (5.29) when α is prescribed (solid curves) and when β is prescribed (short dashed curves). Squire et al. (2001) estimate that the scattering centers along the core proteins were spaced at 20 nm intervals and were of 10-12 nm diameter. Equation (5.5) predicts that ϕ_f falls in the range 0.182-0.345 for r_f=5 to 6 nm. This range of ϕ_f is shown by the vertical-short-dashed lines in Figure 5.7. For the same structural model where r_f=6 nm and R_{eff}=10.5 nm, and a=3.5 nm, $\alpha \cong 0.6$, and β=0.33. One observes that in the range of interest for ϕ_f and α or β, the predictions for the pore theory are close to those for Equation (5.29). For other values of α or β the discrepancy is much larger.

5.5 DISCUSSION

Heretofore, the molecular sieving structure of the EGL had been widely assumed to be associated with extended GAG side chains periodically arranged along the core proteins of proteoglycans (Curry and Michel, 1980; Fu et al., 1994; Hu and Weinbaum, 1999). These extended fibers were thought to be sialic acid side chains with typically 0.6 nm radius. Since the structure of the proteoglycans was largely deduced from their two-dimensional appearance when splayed out on carbon filters (Buckwalter and Rosenberg, 1982), it was never clear how the fibers formed a 3-D lattice. It was assumed that in their extended state the protein monomers had a bottle brush appearance. The quasi-periodic structural model proposed in Squire et al. (2001) and Weinbaum et al. (2003) is a much denser and stiffer structure. The structural model depicted in Figure 5.1 taken from Weinbaum et al. (2003) is an appealing alternative in that it provides a reasonable 3-D organization of the matrix that is consistent with the latest ultrastructural studies (Squire et al., 2001). For a = 3.5 nm (albumin), if r_f = 0.6 nm and δ = 8 nm, values typical of extended glycosaminoglycan side chains, Equation (5.4) predicts that σ_0 = 0.52. In contrast, if r_f = 6 nm and δ = 8 nm, Equation (5.27) predicts that σ_0 = 0.64. The measured value of σ_0 is typically > 0.9 (Michel and Curry, 1999), which can be achieved simply by decreasing δ to 6.5 nm while keeping r_f = 6 nm. Therefore, the structural model proposed in Squire et al. (2001) and Weinbaum et al. (2003) provides more realistic predictions for σ_0 than a model based on extended GAG side chains.

The basic principle behind the oncotic flow in a fiber matrix is that impermeable fiber surfaces within the fiber matrix create radial gradients in solution properties normal to these surfaces which are necessary to maintain thermodynamic equilibrium. A solute

potential energy is generated because the impermeable fiber surfaces interact differently with the solute than with the solvent. The Gibbs-Duhem equation can thus be applied to relate the hydrostatic pressure and the solute concentration in the vicinity of the fiber surface as proposed by Anderson and Malone (1974) for the walls of a cylindrical pore. However, as in the cylindrical pore model in Anderson and Malone (1974), factors other than steric exclusion enter into the evaluation of Equation (5.23) for σ_0. These include solute shape, electrical charge, core protein cross links and other fiber geometries.

When the hydrostatic pressures at both sides are the same but the oncotic pressures are not, the velocity in the excluded zone, $U_e(r,z)$, is a function of r, see Equation (5.33) and Figure 5.3B. There are two components to the velocity in the excluded zone. One is due to the hydrostatic pressure gradient, which is very small in this case, and the other, $U_{e,oncotic}(r,z)$, is due to the oncotic pressure or the concentration gradient. The dependence of $U_e(r,z)$ on r results mostly from $\frac{\partial \pi_{ann}}{\partial z} \neq 0$. In the fluid annulus region ($r_f + a < r \leq R_{eff}$), the velocity, $U_{ann}(r,z)$, is relatively flat and given by Equation (5.32B). One notices in Equation (5.12) that the pressure, $P(r,z)$, in the fluid annulus region is equal to the hydrostatic pressure $P_{ann}(z)$, and $\frac{\partial P_{ann}}{\partial z}$ is close but not equal to zero when $P_{ann}(0) = P_{ann}(L_F)$. However, there are also two components in $U_{ann}(r,z)$. $U_{ann,oncotic}(z)$ describes the continuity in velocity at the interface where $r = r_f + a$. Therefore, the velocity profiles in an oncotic flow differ from those in a pressure driven flow. This raises a basic question: if one applies an oncotic pressure difference across a fiber matrix layer which is equal and opposite to the hydrostatic pressure difference, will

there be no flow? If the fiber matrix is impermeable to the solute the answer is yes. The oncotic pressures on both sides of the matrix layer are exposed to the same net pressure, $P_\infty(z)-\pi_\infty(z)$. The difference in the oncotic pressures, which is the driving force for the oncotic flow, is balanced by the hydrostatic pressure difference. There is no netflow in the fiber matrix. In contrast, if the fiber matrix is leaky to the solute, the flow across the fiber matrix layer is due to the difference in the velocity profiles driven by the hydrostatic pressure gradient and the oncotic pressure gradient. The reflection coefficient actually describes this difference, see Equation (5.19) or Equation (5.27). In Equation (5.19) the numerator is proportional to the average velocity for the oncotic flow and the denominator is proportional to that for pressure driven flow when the pressure gradient is the same as the oncotic pressure gradient. Another paradoxical observation is that if one applies equal hydrostatic pressures but unequal concentration or oncotic pressures at both sides of a leaky fiber matrix layer, the velocity in the fluid annulus, $U_{ann}(r,z)$, is not zero due to the oncotic pressure difference, and there must be convective flux for the solute, which leads to a non-uniform concentration or oncotic pressure gradient, $\frac{\partial \pi_{ann}}{\partial z}$, along the z direction; on the other hand, the average velocity, $\bar{U}$, defined in Equation (5.34) is constant due to the continuity in fluid flux. One concludes that the deviation of the $\frac{\partial \pi_{ann}}{\partial z}$ from a constant gradient must be compensated for by a non-uniform gradient for $\frac{\partial P_{ann}}{\partial z}$. Therefore, $\frac{\partial P_{ann}}{\partial z}$ is close, but not equal to zero.

Equation (5.4) has in the past been used as an approximate expression for the

reflection coefficient for a fiber matrix based on the assumption that there was a Poiseuillean like flow between the fibers. When r_f =6 nm (Squire et al., 2001; Weinbaum et al., 2003), the predicted reflection coefficient as a function of δ for large molecules (a =3.5 nm) agrees well with the predictions of our model. One the other hand, the discrepancy between the predictions of pore theory and the present model for small (a =0.45 nm) and medium (a =2.0 nm) solutes when r_f =6 nm are significant, as well as for r_f =2 nm for large solutes a =3.5 nm, as shown in Figure 5.4, 5.5, and 5.6.

The large differences in the expression for σ_0 between the results for a circular pore and for a periodic fiber array arise from two sources. One is that the velocity profiles generated by the oncotic gradient, second term in Equation (5.33A), are in fact not Poisseuillean and do not have a parabolic profile. The other is that the confining boundary geometries differ greatly , one representing flow interior to a circular cylinder and the other exterior to the cylinder surface.

The curves in Figure 5.7 for Equation (5.29) are truncated at values of ϕ_f <1. ϕ_f =1 requires that all the area within each periodic unit in the fiber matrix be available to solute, i.e., the solid fraction for the fiber matrix is zero. For each value of α or β there is a maximum value of ϕ_f that satisfies the constraint $\phi_f = 1-(\alpha+\beta)^2$. In the limit $\alpha \to 0$ the fiber radius becomes vanishingly small and the minimum value of σ_0 is determined by the exclusion volume of the solute surrounding the fiber axis and is given by $\sigma_0 = \beta^2$, whereas in the limit $\beta \to 0$, σ_0 =0 since the solute radius vanishes and no oncotic force can be generated.

The dimensionless parametric curves in Figure 5.7 are convenient for quickly

estimating σ_0 for a given periodic fiber array in which either α or β are specified. For a given α, the fiber radius and fiber matrix periodicity are specified and one varies β or solute radius. For a given β, the solute radius and fiber matrix periodicity are specified, and one varies α or fiber radius.

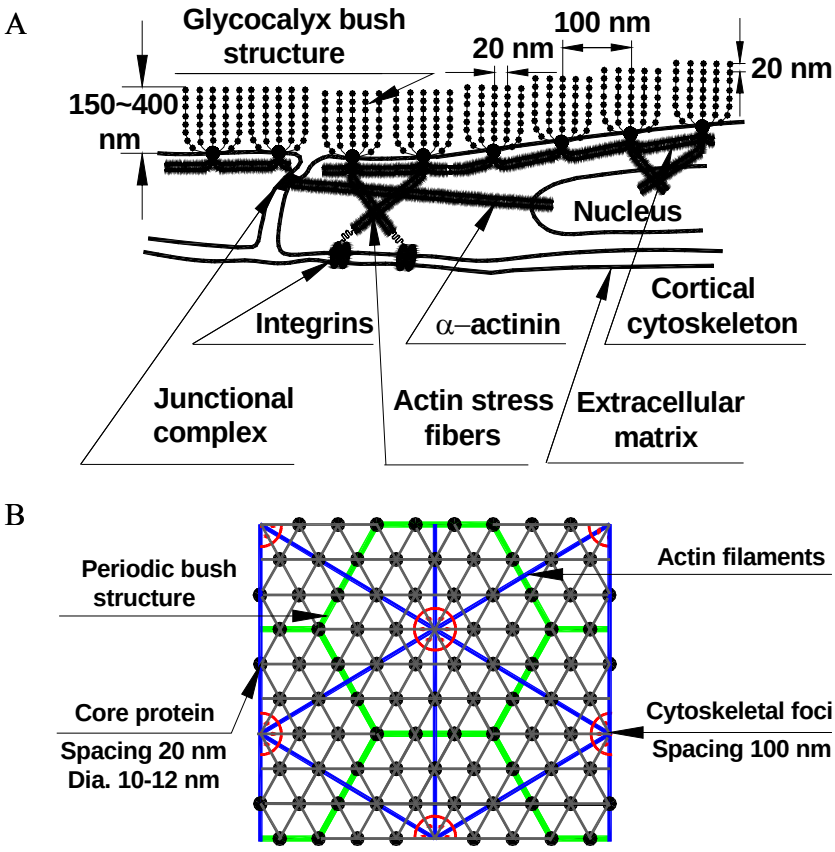

Figure 5.1 A. Sketch of endothelial layer from Weinbaum et al. (2003) with permission. B. En face view of the EGL with the underlying actin cortical web.

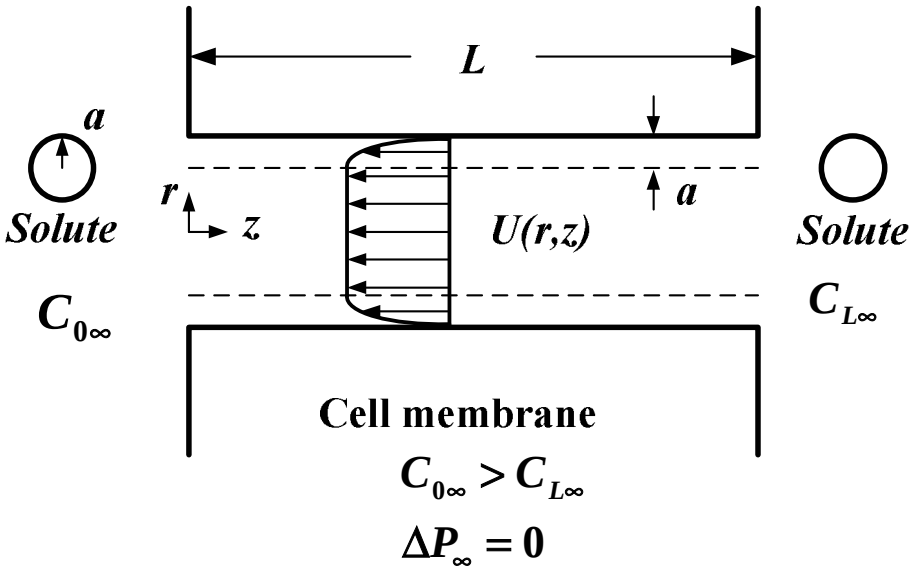

Figure 5.2 Sketch for the pore theory taken from Anderson and Malone (1974). The velocity in the excluded zone is a function of r, while the velocity in the core region is relatively flat when the hydrostatic pressures at both ends are the same.

Figure 5.3 A. The dashed lines ab, cb, and db are lines of flow symmetry along which $\frac{\partial u}{\partial n} = 0$, where *n* is normal to ab, cb, and db. The lines abc, abd, and cbd can be replaced by circular arcs with an effective radius R_{eff}. R_{eff} is chosen such that one half of the resulting fluid annulus has the same area as the open flow cross-section. B. Fluid annulus with radius R_{eff} surrounding the fiber of radius r_f. The sketch for the velocity profile shows that the velocity in the excluded zone is a function of r, while the velocity in the fluid annulus is relatively flat when the hydrostatic pressures at both sides of the fiber matrix layer are the same.

A

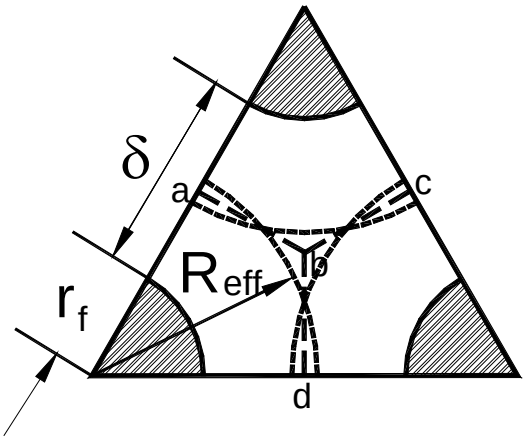

B

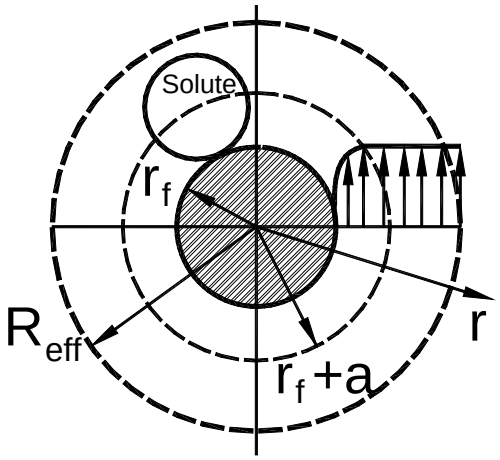

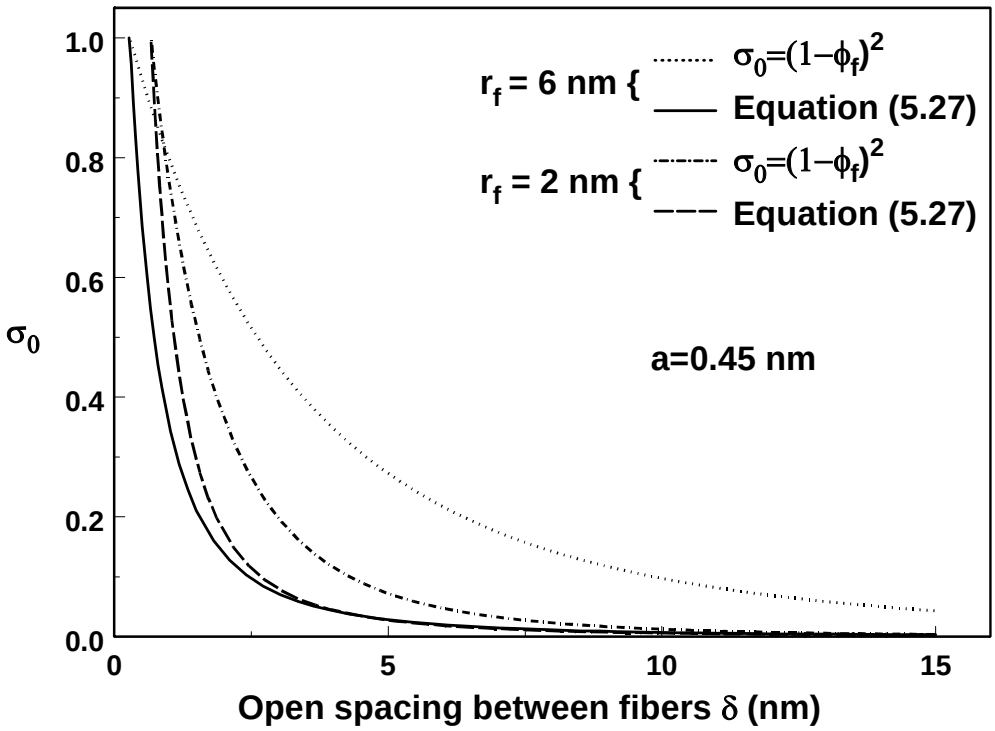

Figure 5.4 Comparison of the predictions of Equations (5.4) and (5.27) for σ_0 as a function of δ for two values of r_f for small size solutes a=0.45 nm.

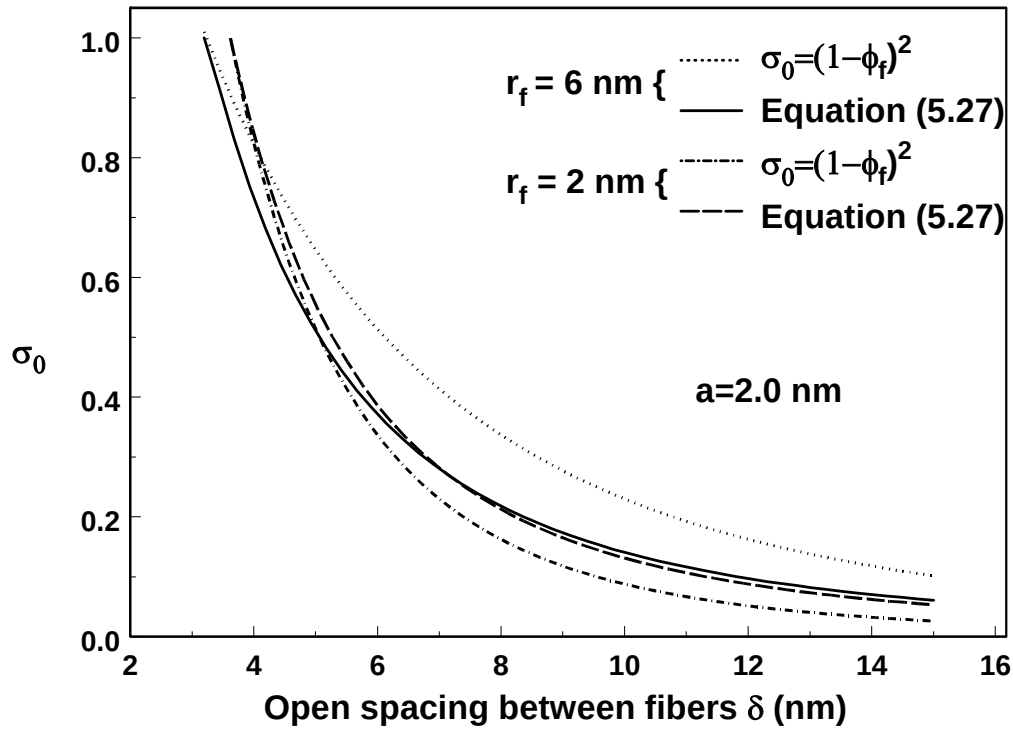

Figure 5.5 Comparison of the predictions of Equations (5.4) and (5.27) for σ_0 as a function of δ. for two values of r_f for small size solutes a=2.0 nm.

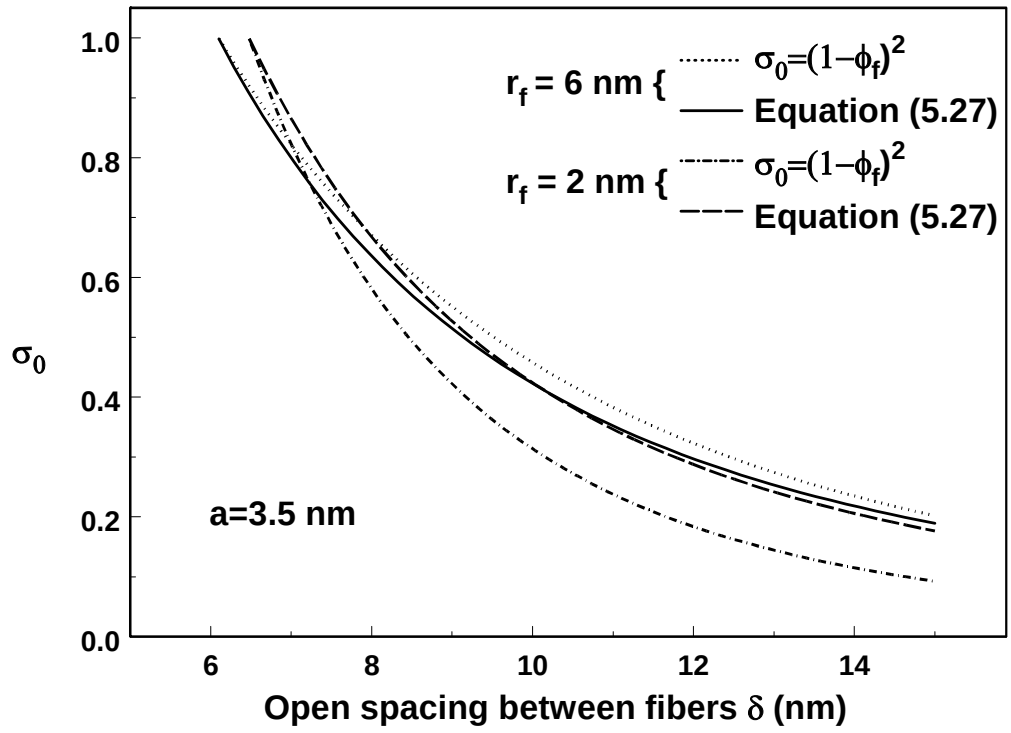

Figure 5.6 Comparison of the predictions of Equations (5.4) and (5.27) for σ_0 as a function of δ. for two values of r_f for small size solutes a=3.5 nm.

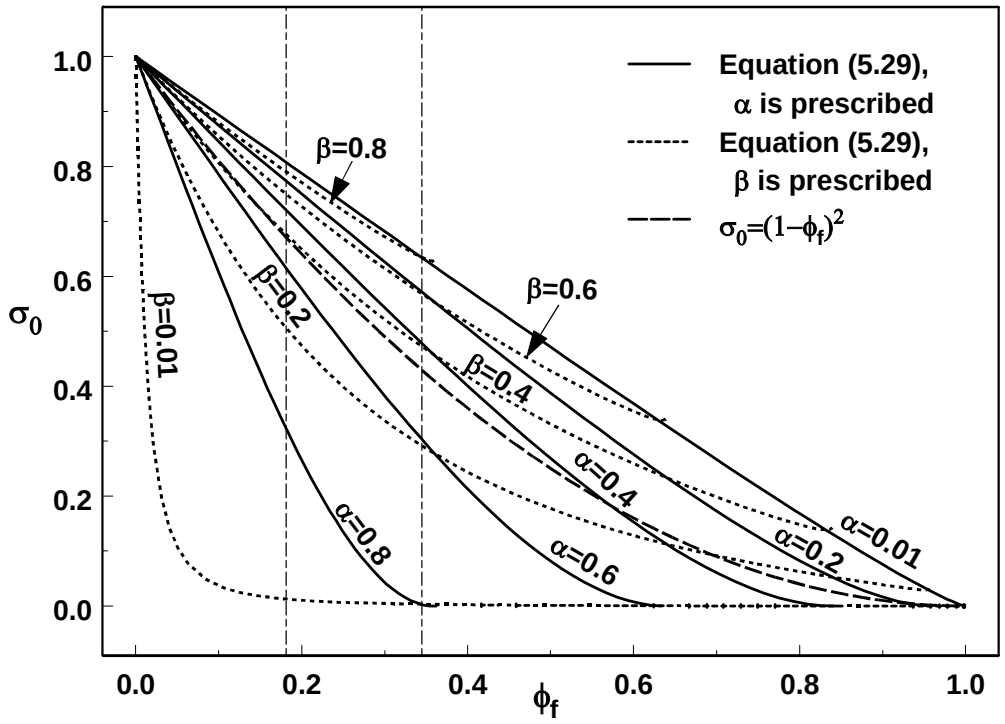

Figure 5.7 Comparison of the predictions of Equations (5.4) and (5.29) for σ_0 as a function of ϕ_f for representative values of α and β.

Chapter 6 Concluding Remarks

6.1 Conclusions

In this dissertation we have quantitatively investigated the multifaceted physiological functions of the EGL as a mechanotransducer of fluid shearing stress, and as a transport barrier, using models for the quasi-periodic structure of the EGL proposed in Squire et al. (2001) and Weinbaum et al. (2003). We also develop a simplified 1-D model to describe the revised Starling principle using the structural parameters for the interendothelial cleft measured in rat mesenteric capillaries (Adamson et al., 2004).

In Chapter 2, we develop a mathematical model for estimating the mechanical properties of the endothelial glycocalyx fibers based on existing experimental data (Vink and Duling, 1999). An important prediction of this study is the bending stiffness of the core proteins in the bush-like clusters that decorate the endothelial surface. The value of *EI*, 700 pN·nm^2, predicted by our model for the restoration of the glycocalyx layer after the passage of a white blood cell is at least 20 times less than the measured *EI*, 15×10^3 (Dupuis *et al*., 1997) ~73×10^3 (Gittes *et al*., 1993), for actin filaments, but sufficiently stiff to resist large deformations of the glycocalyx due to both fluid shear stresses in the physiological range and shear stresses due to the passage of red blood cells. The much larger value of *EI* for the actin filaments in the underlying cortical cytoskeleton indicates that it provides a firm support for the short linker molecules that attach the transmembrane proteins at the base of each bush-like cluster to the submembrane scaffold. We propose that it is these root-like connections which firmly anchor the fiber clusters. Our model predicts that, collectively, but not individually, the core proteins in the bush-

like structures in Figure 2.1A are ideally suited to act as mechanotranducers that convert fluid shearing stresses at the edge of the EGL to deformations of the cortical cytoskeleton. We suggest that this is the initial activating step in intracellular signaling.

In Chapter 3, we use the detailed morphological data for rat mesenteric capillaries obtained by our collaborator at UC Davis, Dr. R. H. Adamson, to construct a 3-D model for the water and solute flux across mammalian capillaries. To our knowledge, it is the first time that such detailed ultrastructural information is available for mammalian capillaries. Based on these structural data, we modify the 3-D model in Hu and Weinbaum (1999) and Hu et al. (2000) which was applied to frog mesenteric capillaries. Our experimental and theoretical results confirm and extend, for rat mesenteric microvessels, the observations described previously for frog mesenteric microvessels, that large protein osmotic pressures are developed across the microvessel wall even when albumin concentrations in the lumen and the tissue are equal (Hu et al., 2000). The measurements of the albumin concentration on both sides of the microvessel wall during high and low filtration states demonstrate that the local albumin concentration behind the glycocalyx must differ greatly from that in the tissue. The effective oncotic pressure difference is close to 70% of luminal oncotic pressure in rat mesenteric capillaries, although the concentration of albumin in the tissue within a few μm of the wall is 80-90% of the lumen value under conditions of both high and low filtration rates.

In Chapter 4, we first investigate the non-linear hydraulic resistance of the cleft when the EGL covers the entrance to the cleft using a detailed 3-D model. The model predicts that the presence of the TJ strand in close proximity to the EGL greatly changes the pressure entrance condition for the cleft and, thus, the fluid streamline pattern in the cleft.

Our 3-D model, as well as the models in Hu and Weinbaum (1999), Hu et al. (2000) and Adamson et al. (2004), also predict that the convective flow through the orifice-like breaks in the TJ strand could greatly reduce back diffusion from the tissue into the lumen side of the TJ strand with the result that the oncotic force behind the EGL could be much smaller than in the tissue at the cleft exit. Using these observations, we develop a much simpler, multilayer, one-dimensional theoretical model that can be solved analytically to provide most of the important results predicted by its much more complex numerical 3-D counterpart (Hu and Weinbaum, 1999; Hu et al., 2000; Adamson et al., 2004). The new model has the important advantage that it is much more accessible to experimentalists and can be readily applied to analyze cleft and junction structure and different tissue loading conditions. The 1-D model predicts that (1) when the entire water and solute fluxes pass through the paracellular pathway and the tissue concentration is equal to the ratio of the total solute to water flux, there is no steady state reabsorption even at very low lumen pressure, and the J_V/A curve bends sharply near $\sigma_f \pi_L$ (Michel and Phillips, 1987; Levick, 1991); (2) when there is a transcellular vesicular pathway in addition to the paracellular pathway, and the tissue concentration is equal to the ratio of the total solute to water flux, the J_V/A curve also bends , but less sharply than when there is only a paracellular pathway for water and albumin transport. If the newly defined vesicular transport coefficient K=5.057 nm/s, then one finds that C_T=0.4C_L at P_L= 25 cm H_2O, the average pressure in a capillary bed whose arterial pressure is about 35 cm H_2O and venous pressure about 15 cm H_2O; (3) when the tissue is backloaded isotonically as in Adamson et al. (2004), the J_V/A curve is in reasonable agreement with their measurements. However, when the tissue is backloaded at a concentration lower than that

in the lumen, there may be steady state reabsorption at low lumen pressure since the concentration behind the EGL cannot rise high enough to arrest the reabsorption. The tissue concentration at low lumen pressure is controlled by the superfusate concentration at the leakage site and does not rise as in the Michel and Phillips (1987) experiment.

In Chapter 5, we propose an approximate model to describe the mechanism of oncotic flow across the EGL based upon the fiber matrix structure proposed in Squire et al. (2001) and Weinbaum et al. (2003). We also derive an expression for the reflection coefficient for the EGL using an approach that parallels that introduced by Anderson and Malone (1974) for circular cylindrical pores, but where the boundaries now are the fibers of the matrix layer. The results show that for solutes of large size, such as albumin (3.5-nm radius), the simple expression proposed by Curry and Michel (1980), $\sigma_0 = (1-\phi_f)^2$, taken from circular pore theory, is surprisingly close to the predictions of the more rigorous model proposed herein. On the other hand, for small and medium sized solutes, the discrepancy between the results predicted by the two models is significant.

6.2 Questions that need to be addressed in the future

6.2.1 Tissue backloading model for the revised Starling principle

Michel and Phillips (1987)'s experiments on frog mesenteric capillaries showed that the transient water reabsorption at low capillary pressure will decay slowly to steady state filtration when the entire solute and water fluxes pass though the paracellular pathway and the concentration in the tissue is determined by the ratio of the total solute to water flux. Hu et al. (2000) and Adamson et al. (2004) observed the similar behaviors in frog and rat mesenteric capillaries, respectively, when they backloaded the tissue isotonically

with respect to the lumen. Pang and Tarbell (2003) also showed the transition from the short-term reabsorption to steady state filtration at low lumen pressure in their in vitro experiment where the concentration in the luminal reservoir is the same as (1 % BSA, equivalent to ~ 10 mg/ml), or higher than (5.5 % BSA, equivalent to ~ 55 mg/ml) the concentration in the abluminal reservoir (1 % BSA). Our model predicts that at low lumen pressure the transient water reabsorption will be arrested and the steady state filtration will be established with or without a transcellular vesicle flux (Michel and Phillips, 1987; Renkin, 1992; Michel, 1997), provided the tissue is not backloaded. The same behavior is observed when the tissue is isotonically backloaded both *in vivo* and *in vitro* (Pang and Tarbell, 2003; Adamson et al., 2004). However, our 1-D model predicts that the reabsorption will not be arrested when the tissue is backloaded at a lower concentration (20 mg/ml) than in the lumen. In this case our model predicts that the tissue concentration at low lumen pressure is controlled by the superfusate concentration at the leakage site and, thus, does not rise sufficiently to arrest the reabsorption as in the Michel and Phillips experiment. This discrepancy between our 1-D model prediction and the *in vitro* experimental observation in Pang and Tarbell (2003) suggests that additional *in vivo* and *in vitro* experiments need to be performed where the tissue is backloaded at lower concentrations to see whether or not the reabsorption can be arrested or not. The critical condition appears to be whether the tissue concentration at the leakage site can be maintained at the same concentration as the superfusate and a backward diffusive gradient established in the tissue. In contrast, backward diffusive gradients are not present in the Pang and Tarbell's *in vitro* experiment.

6.2.2 Transition from transient to steady state in the revised Starling principle

As mentioned above, both Hu et al. (2000) and Adamson et al. (2004) observed the transition from a transient behavior in which the vessel is temporarily reabsorbing to a new steady state in which there is a small positive filtration when the capillary pressure is quickly dropped to a low value from a high filtration state. One would anticipate that the characteristic time for concentration equilibration in the cleft to be of order L^2/D_C where L is the cleft depth and D_C is the diffusion coefficient in the cleft. For $L \cong 400$ nm and $D_C = 2 \times 10^{-7}$ cm^2/s, this time is 0.08s and thus << than 1 sec. If the time to establish a new equilibrium concentration behind the glycocalyx is so short, it is difficult to explain the paradoxical observation that several minutes elapse before a new steady state is achieved. A similar behavior is observed in Michel and Phillips (1987) where there is no back loading of the tissue. We propose that the new equilibrium is associated with the establishment of weak reverse standing concentration gradients in the tissue. Therefore, the characteristic time to achieve steady state is not associated with the equilibration in the cleft but the creation of the far field gradients even though these gradients are very small and the tissue concentration almost but not quite uniform. This paradoxical situation arises because the transport area in the tissue is typically 500 times greater than in the cleft, and the small gradient flux in the tissue can result in a large solute flux into the cleft. Since our numerical relaxation scheme in the 3-D model converges slowly when there are small tissue gradients, it is not easy to modify it to describe the transient process. However, our simple 1-D model provides a more feasible model to investigate the time course of this transition. Since the characteristic time for concentration equilibrium in the cleft is << than in the tissue, one can assume that the instantaneous concentration in the cleft is in a quasi-steady state and the concentration in the tissue varies slowly with time.

Bibliography

1. Adamson, R. H. (1990) Permeability of frog mesenteric capillaries after partial pronase digestion of the endothelial glycocalyx. *J. Physiol.* **428**, 1-13.

2. Adamson, R. H. and Michel, C. C. (1993) Pathways through the intercellular clefts of frog mesenteric capillaries. *J. Physiol.* **466**, 303-327.

3. Anderson, J. L. and Malone, D. M. (1974) Mechanism of osmotic flow in porous membranes. *Biophys J* **14**(12), 957-82.

4. Adamson, R. H., Lenz, J. F., Zhang, X., Adamson, G. N., Weinbaum, S. and Curry, F. E. (2004) Oncotic pressures opposing filtration across non-fenestrated rat microvessels. *J Physiol* **557**: 889-907.

5. Bird, R. B. (2001). Transport phenomena. New York, Wiley.

6. Boggon, T. J., Murray, J., Chappuis-Flament, S., Wong, E., Gumbiner, B. M. and Shapiro, L. (2002) C-cadherin ectodomain structure and implications for cell adhesion mechanisms. *Science* **296**, 1308-1313.

7. Buckwalter, J. A. and Rosenberg, L. C. (1982) Electron microscopic studies of cartilage proteoglycans. Direct evidence for the variable length of the chondroitin sulfate-rich region of proteoglycan subunit core protein. *J. Biol. Chem.* **257**(16), 9830-9839.

8. Clough, G., Michel, C. C. and Phillips, M. E. (1988) Inflammatory changes in permeability and ultrastructure of single vessels in the frog mesenteric microcirculation. *J. Physiol.* **395**, 99-114.

9. Curry, F. E. (1984). Mechanics and thermodynamics of transcapillary enchange. Handbook of physiology. Bethesda, American Physiological Society. **IV:** 309-374.

10. Curry, F. E. and Michel, C. C. (1980) A fiber matrix model of capillary permeability. *Microvasc. Res.* **20**(1), 96-99.

11. Damiano, E. R. (1998) The effect of the endothelial-cell glycocalyx on the motion of red blood cells through capillaries. *Microvasc. Res.* **55**(1), 77-91.

12. Davies, P. F. (1995) Flow-mediated endothelial mechanotransduction. *Physiol. Rev.* **75**(3), 519-560.

13. Dupuis, D. E., Guilford, W. H., Wu, J. and Warshaw, D. M. (1997) Actin filament mechanics in the laser trap. *J. Muscle Res. Cell Motil.* **18**(1), 17-30.

14. Florian, J. A., Kosky, J. R., Ainslie, K., Pang, Z., Dull, R. O. and Tarbell, J. M. (2003) Heparan sulfate proteoglycan is a mechanosensor on endothelial cells. *Circ Res.* **93**(10):e136-42.

15. Feng, J. and Weinbaum, S. (2000) Lubrication theory in highly compressible porous media: the mechanics of skiing, from red cells to humans. *J. Fluid Mechanics* **422**(1), 281-317.

16. Fu, B. M., Weinbaum, S., Tsay, R. Y. and Curry, F. E. (1994) A junction-orifice-fiber entrance layer model for capillary permeability: application to frog mesenteric capillaries. *J. Biomech. Eng.* **116**(4), 502-513.

17. Guo, P., Weinstein, A. M. and Weinbaum, S. (2000) A hydrodynamic mechanosensory hypothesis for brush border microvilli. *Am. J. Physiol. Renal. Physiol.* **279**(4), F698-F712.

18. Henry, C. B. and Duling, B. R. (1999) Permeation of the luminal capillary glycocalyx is determined by hyaluronan. *Am. J. Physiol.* **277**(2 Pt 2), H508-H514.

19. Henry, C. B. and Duling, B. R. (2000) TNF-alpha increases entry of macromolecules into luminal endothelial cell glycocalyx. *Am. J. Physiol. Heart. Circ. Physiol.* **279**(6), H2815-H2823.

20. Hu, X., Adamson, R. H., Liu, B., Curry, F. E. and Weinbaum, S. (2000) Starling forces that oppose filtration after tissue oncotic pressure is increased. *Am. J. Physiol. Heart Circ. Physiol.* **279**(4), H1724-H1736.

21. Hu, X. and Weinbaum, S. (1999) A new view of Starling's hypothesis at the microstructural level. *Microvasc. Res.* **58**(3), 281-304.

22. Levick, J. R. (1991) Capillary filtration-absorption balance reconsidered in light of dynamic extravascular factors. *Exp Physiol.* **76**(6), 825-857.

23. Luft, J. H. (1966) Fine structures of capillary and endocapillary layer as revealed by ruthenium red. *Fed. Proc.* **25**(6), 1773-1783.

24. Pang Z. and Tarbell J. M. (2003) In vitro study of Starling's hypothesis in a cultured monolayer of bovine aortic endothelial cells. *J Vasc Res.* **40**(4):351-358.

25. McDonald J. N. and Levick J. R. (1993) Effect of extravascular plasma protein on pressure-flow relations across synovium in anaesthetized rabbits. *J Physiol* **465**: 539-559.

26. Michel, C. C. (1983). The effects of certain proteins on capillary permeability to fluid and macromolecules. Pathogenicity of Cationic Proteins. P. P. Lambert, Bergmann, P., & Beauwens, R. New York, Raven Press**:** 125–140.

27. Michel, C. C. (1997) Starling: the formulation of his hypothesis of microvascular fluid exchange and its significance after 100 years. *Exp. Physiol.* **82**(1), 1-30.

28. Michel, C. C. and Phillips, M. E. (1987) Steady-state fluid filtration at different capillary pressures in perfused frog mesenteric capillaries. *J Physiol* **388**, 421-435.

29. Pries, A. R., Secomb, T. W. and Gaehtgens, P. (2000) The endothelial surface layer. *Pflugers. Arch.* **440**(5), 653-666.

30. Renkin E. M. (1977) Multiple pathways of capillary permeability. *Circ Res* **41**, 735-743.

31. Renkin E. M. (1992) Cellular and intercellular transport pathways in exchange vessels. *Am. Rev. Respir. Dis.* **146**, S28-31.

32. Rostgaard, J. and Qvortrup, K. (1997) Electron microscopic demonstrations of filamentous molecular sieve plugs in capillary fenestrae. *Microvasc. Res.* **53**(1), 1-13.

33. Sako, Y. and Kusumi, A. (1995) Barriers for lateral diffusion of transferrin receptor in the plasma membrane as characterized by receptor dragging by laser tweezers: fence versus tether. *J. Cell Biol.* **129**(6), 1559-74.

34. Sangani, A. S. and Acrivos, A. (1982) Slow flow past periodic arrays of cylinders with application to heat transfer. *International Journal of Multiphase Flow* **8**(3), 193-206.

35. Schulze, C. and Firth, J. A. (1992) Interendothelial junctions during blood-brain barrier development in the rat: morphological changes at the level of individual tight junctional contacts. *Brain Res Dev Brain Res* **69**: 85-95.

36. Secomb, T. W., Hsu, R. and Pries, A. R. (1998) A model for red blood cell motion in glycocalyx-lined capillaries. *Am. J. Physiol.* **274**(3 Pt 2), H1016-H1022.

37. Secomb, T. W., Hsu, R. and Pries, A.R. (2001) Effect of the endothelial surface layer on transmission of fluid shear stress to endothelial cells. *Biorheology* **38**(2-3), 143-150.

38. Shapiro, L., Fannon, A. M., Kwong, P. D., Thompson, A., Lehmann, M. S., Grubel, G., Legrand, J. F., Als-Nielsen, J., Colman, D. R. and Hendrickson, W. A. (1995) Structural basis of cell-cell adhesion by cadherins. *Nature* **374**, 327-337.

39. Squire, J. M., Chew, M., Nneji, G., Neal, C., Barry, J. and Michel, C. C. (2001) Quasi-periodic substructure in the microvessel endothelial glycocalyx: a possible explanation for molecular filtering? *J. Struct. Biol.* **136**(3), 239-255.

40. Timoshenko, S. P. and Gere, J. M. (1988). Theory of elastic stability. Large deflections of buckled bars(the elastica). New York, McGraw Hill**:** 76-82.

41. Tsay, R., Weinbaum, S. and Pfeffer, R. (1989) A new model for capillary filtration based on recent electron microscopic studies of endothelial junctions. *Chem. Eng. Commun* **82**, 67-102.

42. Vink, H. and Duling, B. R. (1996) Identification of distinct luminal domains for macromolecules, erythrocytes, and leukocytes within mammalian capillaries. *Circ. Res.* **79**(3), 581-589.

43. Vink, H., Duling, B. R. and Spaan, J. A. E. (1999) Mechanical properties of the endothelial surface layer (Abstract). *FASEB J.* **13**, A11.

44. Weinbaum, S. (1998) 1997 Whitaker Distinguished Lecture: Models to solve mysteries in biomechanics at the cellular level; a new view of fiber matrix layers. *Ann. Biomed. Eng.* **26**(4), 627-643.

45. Weinbaum, S., Zhang, X., Han, Y., Vink, H. and Cowin, S. C. (2003) Mechanotransduction and flow across the endothelial glycocalyx. *PNAS* **100**(13), 7988-7995.

46. Yan Z. Y., Weinbaum S. and Preffer, R. (1986) On the fine structure of osmosis including three-dimensional pore entrance and exit behaviour. *J. Fluid Mech.* **162**: 415-438.

47. Zhao, Y., Chien, S. and Weinbaum, S. (2001) Dynamic contact forces on leukocyte microvilli and their penetration of the endothelial glycocalyx. *Biophys. J.* **80**(3), 1124-1140.